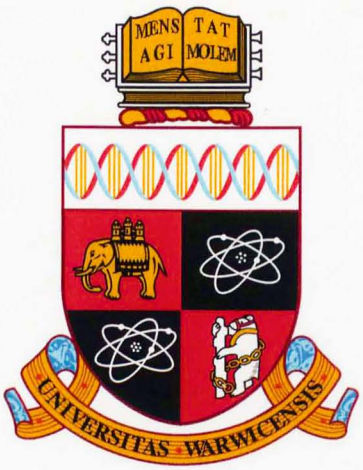

Studies of Unconventional Superconductors

by

Pabitra Kumar Biswas

Thesis

Submitted to the University of Warwick

for the degree of

Doctor of Philosophy

Department of Physics

June 2012

THE UNIVERSITY OF
WARWICK

Contents

List of Tables

List of Figures

Acknowledgments

First of all, I would like to acknowledge my supervisors Dr. Martin R. Lees and Prof. Don McK Paul for the advice and support I have received for the last three and a half years. It has been a real pleasure to work with them. I am extremely grateful to Dr. Adrian Hillier of ISIS Facility, RAL for his help with carrying out μSR measurements and understanding the results. It has been a privilege to work with a number of very talented international collaborators including Dr. Charles Dewhurst, Dr. Jorge Gavilano, Nikola Egetenmeyer, Dr. Ron Smith and Dr. William Marshall.

Thanks to Dr. Geetha Balakrishnan for supervising the crystal growths and Dr. Oleg Petrenko for his advice on Laue imaging system. A special thanks to Dr. Ravi Singh for lots of moral support. Many thanks to Tom Orton, for all the technical support. Thanks to the rest of the superconductivity and magnetism group: Andy Crichton, Dan O'Flynn, Tom Hayes, Catherine Fleck, Olga Young, Michael Smidman, Natalia Parzyk, and Robert Cook for their company over the last three and half years. Thanks to Dr. Da-qian Liao for growing the single crystal of CaAlSi, Dr. Dean Keeble for helping in single crystal X-ray diffraction of CaAlSi, and Steve York for the EDX measurements.

I would like to thank the Midlands Physics Alliance Graduate School for a studentship. The Quantum Design MPMS magnetometer and PPMS used in this work were obtained through the Science City Advanced Materials project: Creating and Characterizing Next Generation Advanced Materials project, with support from Advantage West Midlands (AWM) and part funded by the European Regional Development Fund (ERDF).

Finally, I would like to thank and dedicate this thesis to my parents for all their support and encouragement, my lovely wife Aparna for her support and patience and the rest of my family. Thanks to all of my friends for their love and support during my PhD at Warwick.

Declarations and Published Work

All the work presented in this thesis was carried out by me, except where explicitly stated. All of the experiments described in this thesis took place during the period of October 2008 to October 2011 and were carried out at the Department of Physics at the University of Warwick, the Institut Laue-Langevin, Paul Scherrer Institut or ISIS at the Rutherford Appleton Laboratory. For all of these experiments, I was either the sole experimentalist or a leading member of the experimental team. I have carried out all the experiments in the central facilities with the assistance of an instrument scientist. Analysis of the data from these experiments were conducted under the guidance of Dr. Martin Lees, Prof. Don McK Paul, Dr. Adrian Hillier, Dr. Charles Dewhurst, Dr. Ron Smith and Dr. William Marshall. The single crystal samples of ZrB_{12} were produced by myself, under the guidance of Dr. Geetha Balakrishnan. The single crystal samples of CaAlSi were made by Dr. D. Q. Liao. All the other samples were produced exclusively by myself. No part of this thesis has been submitted for examination at any other institute. Parts of the work described in this thesis have been published in the following articles:

1. P. K. Biswas, M. R. Lees, G. Balakrishnan, D. Q. Liao, J. L. Gavilano, N. Egetenmeyer, C. D. Dewhurst, and D. McK. Paul, *First-Order Reorientation of the Flux-Line Lattice in CaAlSi*, *Physical Review Letter* **108**, 077001 (2012).

2. P. K. Biswas, M. R. Lees, A. D. Hillier, and D. McK. Paul, *Comparative study of the centrosymmetric and non-centrosymmetric superconducting phases of*

Re3W using Muon-spin-spectroscopy and heat capacity measurements, *Physical Review B* **85**, 134505 (2012).

3. P. K. Biswas, M. R. Lees, A. D. Hillier, R. I. Smith, W. G. Marshall, and D. McK. Paul, *Structure and superconductivity of two different phases of* Re_3W, *Physical Review B* **84**, 184529 (2011).

4. P. K. Biswas, G. Balakrishnan, D. McK. Paul, M. R. Lees, A. D. Hillier, *Two-gap superconductivity in* $Lu_2Fe_3Si_5$, *Physical Review B* **83**, 054517 (2011).

5. P. K. Biswas, G. Balakrishnan, D. McK. Paul, C. V. Tomy, M. R. Lees, A. D. Hillier, *Muon-spin-spectroscopy study of the penetration depth of* $FeTe_{0.5}Se_{0.5}$, *Physical Review B* **81**, 092510 (2010).

6. P. K. Biswas, M. R. Lees, A. D. Hillier, and D. McK. Paul, *Coexistence of type-I and type-II superconductivity in the single crystal of* ZrB_{12}, (manuscript under preparation).

7. P. K. Biswas, A. D. Hillier, D. M. Paul, and M.R. Lees, *Structural, magnetic and transport properties of* $FeTe_{1-x}S_x$ *(*$0.1 \leq x \leq 0.5$*)*, (manuscript under preparation).

Abstract

In this thesis, the superconducting properties of some unconventional superconductors have been investigated using low temperature magnetic, thermal and transport measurements, small angle neutron scattering, and muon spin rotation/relaxation techniques. The aim was to correlate the symmetry and structure of the superconducting gap with the unusual properties in these superconductors.

These studies have required the preparation of high quality samples using different growth techniques. Good quality polycrystalline and single crystal samples of $FeSe_{1-x}Te_x$ and $FeTe_{1-x}S_x$ were grown using a self-flux method. Polycrystalline samples of $Lu_2Fe_3Si_5$ and Re_3W were made using the arc furnace. We have also grown single crystals of ZrB_{12} using the optical floating zone method in a 4 mirror image furnace, and CaAlSi crystal using the Bridgman method. All the compounds have been characterized with a combination of X-ray, neutron diffraction, EDX, magnetization, resistivity or specific heat measurements.

In order to investigate the pairing symmetry of the iron chalcogenide superconductors, low temperature muon spin rotation/relaxation (μSR) measurements have been performed on $FeTe_{0.5}Se_{0.5}$. The temperature dependence of the in-plane magnetic penetration depth is found to be compatible with either a two gap $s+s$-wave or an anisotropic s-wave model. This result is consistent with our heat capacity data collected on the same sample. μSR results of $FeTe_{1-x}S_x$ show an antiferromagnetic transition at low temperature and also suggest the presence of excess S in the samples. A similar magnetic transition has also been observed in the magnetization measurements.

The symmetry of the superconducting gap of $Lu_2Fe_3Si_5$ with $T_c = 6.1$ K has been investigated using low-temperature transverse-field μSR and specific heat measurements. The temperature dependence of the magnetic penetration depth, $\lambda(T)$ is consistent with a two gap $s+s$-wave model. Low-temperature specific heat measurements on the same sample also show evidence of two distinct superconducting gaps and hence support the muon results.

To resolve whether CaAlSi is a single band or multiband superconductor, we have studied the flux line lattice in CaAlSi using small angle neutron scattering. A well defined hexagonal flux line lattice is seen just above H_{c1} in an applied field of only 54 Oe. A 30° reorientation of this vortex lattice has been observed in a very low field of 200 Oe. This reorientation transition appears to be of first-order and

could be explained by non-local effects. The magnetic field dependence of the form factor is well described by a single penetration depth and a single coherence length. The penetration depth anisotropy has also been estimated with the field applied at different angles to the c-axis.

The B-T phase diagram of superconducting ZrB_{12} has been investigated by means of μSR spectroscopy using a mosaic of single crystal. The local field distribution for different applied fields and temperatures shows evidence of the Meissner, mixed, and intermediate states in ZrB_{12}. The intermediate state indicates that this material has some of the characteristics of a type-I superconductor, while the mixed state is typical of a type-II superconductor. Regions of coexistence have also been observed between the different states. We have not observed any distinct features of two-band or two-gap superconductivity in this material.

Two different superconducting phases of Re_3W have been found with different physical properties. One phase crystallizes in a non-centrosymmetric cubic (α-Mn) structure and has a superconducting transition temperature, T_c, of 7.8 K. The other phase has a hexagonal centrosymmetric structure and is superconducting with a T_c of 9.4 K. Switching between the two phases is possible by annealing the sample or remelting it. The zero-field μSR results indicate that time reversal symmetry is preserved for both structures of Re_3W. For both phases of Re_3W, the temperature dependence of the penetration depth can be explained using a single-gap s-wave BCS model. Low temperature specific heat data also provide evidence for an s-wave gap-symmetry for the two phases of Re_3W. Both the μSR and heat capacity data show that the CS material has a higher T_c and a larger superconducting gap $\Delta(0)$ at 0 K than the NCS compound.

The experimental work detailed in this thesis provides new information on the superconducting properties of $FeSe_{0.5}Te_{0.5}$, $FeTe_{1-x}S_x$, $Lu_2Fe_3Si_5$, CaAlSi, ZrB_{12}, and two different superconducting phases of Re_3W and contributes to our overall understanding of the physics of the different exotic superconducting features in these systems.

Chapter 1

Introduction

1.1 Introduction to Superconductivity

1.1.1 On a Historical Note

Superconductivity is among the most fascinating properties that a material can show. A superconducting material exhibits zero electrical resistance and the expulsion of magnetic fields below a certain temperature, called the superconducting transition temperature, T_c. Superconductivity was first discovered in April of 1911 by the Dutch physicist Heike Kamerlingh Onnes of Leiden University. He and his co-workers cooled mercury to the boiling temperature of liquid helium (4.2 K) and observed the abrupt vanishing of its electrical resistance [1]. He was awarded the Nobel Prize in Physics for low-temperature investigations in 1913. Since then, it has been a key interest to understand the mechanism behind superconductivity and find superconducting materials with higher T_c values. In the following 100 years, many superconductors were discovered [see Fig. 1.1].

The next great discovery in understanding superconductivity occurred when the expulsion of magnetic field was discovered by Meissner and Ochsenfeld in 1933 [2]. This phenomenon of superconductivity is now known as the Meissner effect. Over the next few decades, theorists struggled to find a microscopic theory for superconductivity. Major advances were made toward such a theory for superconductivity with the development of the London theory [3] in 1935 and the Ginzberg-Landau theory [4] in 1950. The complete microscopic theory of superconductivity was finally proposed in 1957 by Bardeen, Cooper, and Schrieffer [5] and is called the *BCS* theory. The authors were awarded the Nobel Prize in Physics in 1972. In general, the *BCS* theory limits superconducting transition temperatures to below 30 K. The limiting value of T_c was calculated as a function of the electron-phonon and

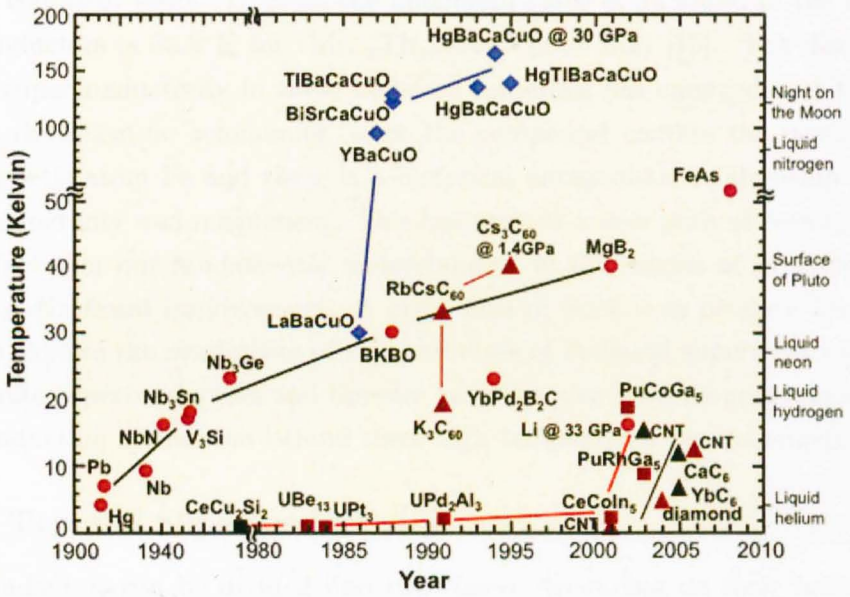

Figure 1.1: The chronology of the discoveries of superconductors with higher critical temperatures. The figure was taken from the website of the Coalition for the Commercial Application of Superconductors (CCAS).

electron-electron coupling constants within the framework of the strong-coupling theory [6]. Indeed, no superconducting compounds with T_c values higher than 30 K were known for a long time. In this context, the most important low-temperature superconductors are the metallic A15 compounds (Nb_3Ge, $T_c = 23$ K) [7] and the Chevrel phases ($PbMo_6Se_8$, $T_c = 18$ K) [8].

A genuine breakthrough was achieved in superconductivity research when high-temperature superconductivity was discovered in the cuprates in 1986 [9]. These ceramic superconductors show T_c higher than 77 K (the boiling point of liquid nitrogen), with 93 K in $YBa_2Cu_3O_7$ [10]. The highest confirmed value of T_c at ambient pressure so far is 133 K observed in $HgBa_2CaCu_2O_{6+x}$ [11]. In 1994, another class of superconductor, rare-earth borocarbides were discovered with a highest T_c of 23 K for YPd_2B_2C [12]. There was another surprise in the superconductor world when a metallic superconductivity with a T_c value of 39 K was found in a simple binary compound MgB_2 in 2001 [13].

In March 2008, a new era in superconductivity research began with the discovery of high-T_c superconductivity in an iron based compound with a T_c of 26 K [14]. Many families of Fe-based superconductors have been discovered within

the last couple of years. To date, the maximum value of T_c found in the Fe-based superconductors is 56.3 K for $Gd_{1-x}Th_xFeAsO$ ($x = 0.2$) [15]. The discovery of high-T_c superconductivity in these Fe-based materials has emerged as a huge surprise to the scientific community, since the compound contain the most familiar ferromagnetic atom Fe and there is a historical antagonistic relationship between superconductivity and magnetism. This has opened a new path of research driven by the fact that our fundamental understanding of the origins of superconductivity needs significant improvement. A great deal of work is in progress around the world to explore the similarities of this new class of Fe-based superconductors with the cuprate superconductors and thereby pave the way towards understanding the superconducting mechanism behind these high temperature superconductors.

1.1.2 Types of Superconductivity

Superconductors can be divided into two classes depending on their behaviour in an applied magnetic field. These are: Type-I and Type-II superconductors. In Type-I superconductors, there is a complete expulsion of an internal magnetic field from the bulk of a superconductor below T_c and this state is called the Meissner state [see Fig. 1.2]. As a result of this field expulsion, the magnetization (M) of a superconductor and the field (H) applied on it must be equal but opposite in sign. This implies that Type-I superconductor exhibits perfect diamagnetism, i. e., $\chi = M/H = -1$ in cgs unit. Superconductivity can be destroyed by the application of a large enough field called the critical field (H_c). The value of H_c needed to drive a superconductor into the normal state is calculated as a function of temperature (T):

$$H_c(T) \approx H_c(0)\left[1 - \left(\frac{T}{T_c}\right)^2\right], \tag{1.1}$$

where $H_c(0)$ is the critical field at absolute zero. The effect of H_c depends on the shape of the sample. For a sample with zero demagnetizing factor (a long cylinder or thin sheet with the field applied parallel to its length), the value of H_c everywhere along the surface is equal to the applied field, H_a. For samples with other geometries, where the demagnetizing factor is not zero, the actual field over some parts of the sample will exceed H_a, causing some normal regions to appear while H_a is still less than H_c. In this stage, there is always a coexistence between the superconducting and normal regions. This state is called the intermediate state of a Type-I superconductor.

In Type-II superconductors, the complete expulsion of the magnetic field ex-

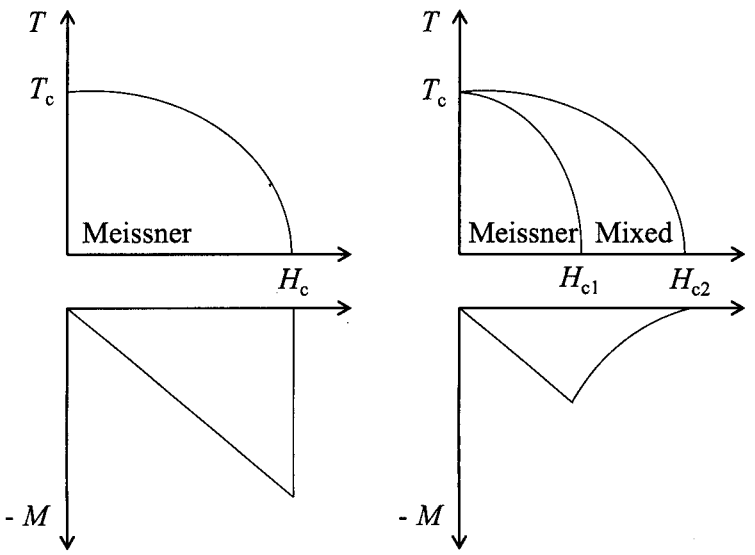

Figure 1.2: H-T and M-T phase diagrams for a Type-I (left) and Type-II (right) superconductor.

ists up to a certain critical field, called the lower critical field (H_{c1}). Above H_{c1}, the magnetic field enters into the bulk of a superconductor in the form of quantized flux lines (also called Abrikosov vortices after their discoverer [16]). The cores of these vortex are normal, surrounded by superconducting material. Each vortex carries a quantum of magnetic flux, $\phi_0 = h/2e$. These tiny vortices of magnetic flux repel each other and tend to arrange themselves in a periodic triangular flux line lattice (FLL) to lower their energy configuration. In general, we see a triangular/hexagonal FLL symmetry in the vortex state of a Type-II superconductor. However, since the energy difference between triangular and square FLL symmetries is only 2%, in some superconductors, the FLL also show cubic symmetry. For more details about the FLL, read the review article by E. H. Brandt [17]. As the field is increased further, more flux vortices enter the sample until a critical flux density is reached at another critical field. This second critical field is called the upper critical field (H_{c2}), above which the superconductor become a normal conductor. The behaviour of both types of superconductors under the application of field is shown schematically in Figure 1.2. For more details, see *Introduction to Superconductivity* by M. Tinkham [18].

The types of a superconductor can also be understood in terms of Ginzburg-Landau (GL) theory. A superconducting state has two characteristic lengthscales,

the penetration depth, λ, and the coherence length, ξ. The penetration depth is the distance over which an applied magnetic field will extend into the superconductor, and the coherence length is the minimum distance over which the density of superconducting carriers (electrons) can change. The ratio of these two lengthscales (λ/ξ) is called the GL parameter, κ. Although both λ and ξ depend strongly on temperature, κ is roughly temperature independent for most superconductors as the temperature effect cancel out in the ratio. κ is the key parameter in determining the nature of the behavior of a superconductor in a magnetic field. The limiting value of $\kappa = 1/\sqrt{2}$ separates Type-I and Type-II superconductors. In Type-I superconductors, κ is less than $1/\sqrt{2}$ and the surface energy associated with the boundary between superconducting and normal regions is positive. To maintain the lowest energy state, the surface energy i.e. the boundary area has to reduce as much as possible. Hence an external applied field is expelled from the bulk of a Type-I superconductor. However in Type-II superconductors, κ is greater than $1/\sqrt{2}$ and the surface energy is negative. To gain the lowest energy state, this will favour the field penetrating the superconductor in the form of quantized flux lines as discussed earlier to give a maximum possible boundary area.

In general, superconductors are classed as either Type-I or of Type-II. However, there are reports of low-κ Type-II superconductors like pure Nb, TaN (see Ref. [19]), where the authors describe the unusual behaviour in the vortex state due to an attractive interaction between flux lines. Recently a similar feature has possibly been observed in MgB_2, where a totally new state called "Type 1.5 superconductivity" is claimed by Moshchalkov *et al.* [20]. There is also the possibility of coexistence between Type-I and Type-II superconductivity which we have found with the low κ superconductor ZrB_{12}. For the results and discussion about the coexistence between Type-I and Type-II superconductivity in ZrB_{12}, see chapter 6.

1.2 Theory of Superconductivity

Developing the theory of superconductivity was one of the hardest problems in theoretical physics during the 20th century. Many great physicists have spent their time investigating the origin of superconductivity since its discovery in 1911. Those include the initial work by Cornelius Gorter and Hendrik Casimir in 1934 [21] followed by the outstanding phenomenological theories of Heinz and Fritz London in 1935 [3] and Vitaly Ginzburg and Lev Landau in 1950 [4]. All these efforts made significance advances in understanding how superconductivity works. Throughout these processes, several empirical relations had also been observed that hinted at

the importance of the crystal lattice to superconductivity. The T_c of a Type-I superconductor and its room temperature resistivity were found to be inversely related. Most interestingly, the best normal conductors such as Cu, Ag and Au did not even show a sign of a superconducting transition down to the lowest measurable temperature. It was also noticed that the T_c varied with the isotope. All this evidence indicated that there was a deep connection between the electron and the lattice vibration (phonon) of a material and this may be related to its superconductivity. This was finally revealed by Bardeen, Cooper and Schrieffer in a theory, called the *BCS* theory of superconductivity.

1.2.1 *BCS* Theory

The basic idea of the BSC theory is that electrons in a superconductor form a pair (known as a Cooper pair) via the electron-phonon interaction. In the simplest case, the electron-phonon interaction gives rise to a Cooper pair in the most symmetric form, i.e. vanishing relative orbital angular momentum and spin singlet configuration, called s-wave pairing symmetry. Electrons are fermions which means that no two electrons can be in the same quantum state. However, there is no such constraint for a Cooper pair. The Cooper pairs are more similar to bosons; they may condense into a quantum ground state and travel together collectively and coherently.

For a pair of electrons, the binding energy will be maximal if they have opposite momenta (k, -k), and the exchange correlation energy will be a minimum if they have opposite spins. Therefore, to minimize the ground state energy of a superconducting state, the Cooper pairs will have zero relative angular momentum and spin. This pairing state is called the singlet state with $k\uparrow$ and $k\downarrow$ electrons. *BCS* took the ground state wave function of a Cooper pair as

$$|\Psi_{BCS}\rangle = \prod_k (u_k^* + v_k^* c_{k\uparrow}^\dagger c_{-k\downarrow}^\dagger)\,|0\rangle\,, \tag{1.2}$$

where $c_{k\uparrow}^\dagger$, $c_{-k\downarrow}^\dagger$ are the electron creation operators that create a pair of electrons of zero relative momentum and opposite spin. $|0\rangle$ is the vacuum state. u_k^*, v_k^* are complex wavefunctions with $|u_k|^2 + |v_k|^2 = 1$. The probability of the pair ($k\uparrow$, $k\downarrow$) being occupied is $|v_k|^2$, and the probability that it is not occupied is $|u_k|^2 = 1 - |v_k|^2$.

In the language of second quantization, the reduced Hamiltonian of such a Cooper pair is

$$H = \sum_{k,\sigma=\uparrow,\downarrow} \left(\frac{\hbar^2 k}{2m} - \mu \right) c^\dagger_{k\sigma} c^\dagger_{-k\sigma} + \frac{1}{2} \sum_{k,k'} c^\dagger_{k\uparrow} c^\dagger_{-k\downarrow} V_{k,k'} c^\dagger_{k'\uparrow} c^\dagger_{-k'\downarrow}, \tag{1.3}$$

The first term describes the Bloch electrons, $\left(\frac{\hbar^2 k}{2m} - \mu \right)$ is the band energy dispersion with the chemical potential μ, and $V_{k,k'}$ is an attractive interaction. The attractive interaction between the electrons is necessary for creating the Cooper pairs and hence superconductivity. Electrons normally repel each other due to the electrostatic Coulomb force. However, it is possible for the motion of ions to screen the Coulomb repulsion between the electrons and produce a net attractive interaction. The details of how this may happen is described by Tinkham [22].

The ground state of the system can be obtained by minimizing the expectation value of the sum by setting

$$\langle \Psi_{BCS} | \sum_{k,\sigma=\uparrow,\downarrow} \left(\frac{\hbar^2 k}{2m} - \mu \right) c^\dagger_{k\sigma} c^\dagger_{-k\sigma} + \frac{1}{2} \sum_{k,k'} c^\dagger_{k\uparrow} c^\dagger_{-k\downarrow} V_{k,k'} c^\dagger_{k'\uparrow} c^\dagger_{-k'\downarrow} | \Psi_{BCS} \rangle = 0, \tag{1.4}$$

Minimization yields the expression for an excitation of wave vector k in a superconductor with energy

$$E_k = \sqrt{\left(\frac{\hbar^2 k}{2m} - \mu \right)^2 + \Delta^2}, \tag{1.5}$$

where Δ is the energy gap in the excitation spectrum and represent the expectation value of of the second term of Eq. 1.4.

1.2.2 Energy Gap

According to the *BCS* theory, the energy gap depends on the temperature and can be calculated by solving the self-consistent *BCS* equation [23]

$$\int_0^\infty dE \left[\frac{\tanh\left(\frac{1}{2T} \sqrt{E^2 + \Delta^2} \right)}{\sqrt{E^2 + \Delta^2}} - \frac{1}{E} \tanh\left(\frac{E}{2T_c} \right) \right] = 0, \tag{1.6}$$

An approximation to Eq. 1.6 can be written as

$$\Delta(T) = 1.76 \tanh\left\{ 1.82 \left[1.018 \left(\frac{T_c}{T} - 1 \right) \right]^{0.51} \right\}, \tag{1.7}$$

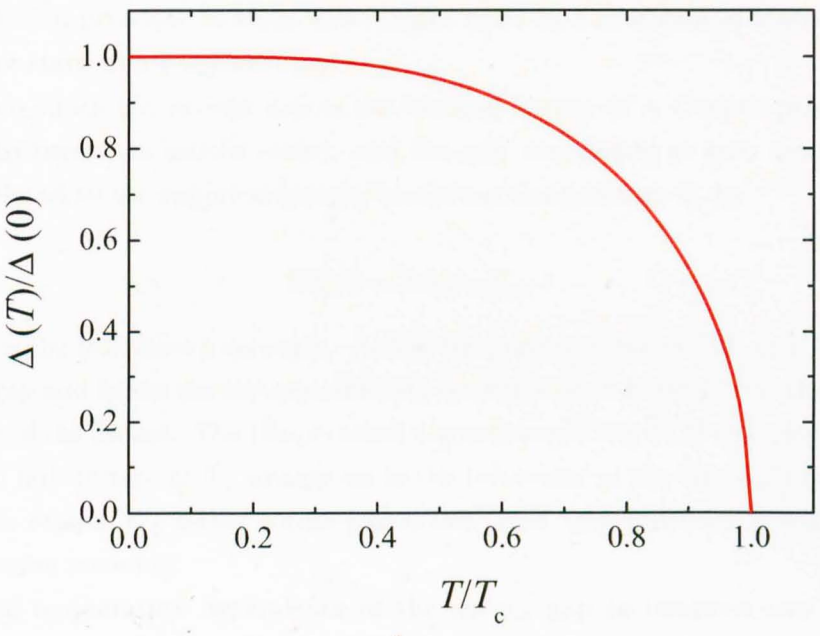

Figure 1.3: Temperature dependence of the normalised *BCS* gap function, $\Delta(T)/\Delta(0)$.

The temperature dependence of the *BCS* gap function, $\Delta(T)$ of Eq. 1.7 is shown in Figure 1.3.

A superconductor with *BCS* gap symmetry is known to have *s*-wave pairing symmetry. All the superconductors with *s*-wave pairing symmetry are generally called conventional *BCS* superconductors. In this pairing symmetry, electrons with opposite spin (singlet) form the cooper pairs. This is manifested as a finite-sized energy gap called superconducting gap in single particle excitations throughout the entire Fermi surface. Here, the orbital state of the Cooper pair can be a spherically symmetric analogous to an atomic *s* orbital. A deviation from this symmetry is considered as unconventional. For many unconventional superconductors, since Coulomb repulsive interaction between electrons is often rather strong, Cooper pairs favour a non-zero angular momentum to minimize the total energy. For example, Cooper pairs with relative orbital angular momentum $L = 1$ form the *p*-wave pairing symmetry (triplet), as we have seen for Sr_2RuO_4 [24]. The cuprate high temperature superconductors take the *d*-wave pairing symmetry (singlet) with relative orbital angular momentum $L = 2$ [25]. These cause superconducting gap diminishes at certain locations called nodes on the Fermi surface. The orbital state of the Cooper pairs with *p* and *d*-waves are analogous to atomic *p* and *d* orbitals, respectively. The

Pauli exclusion principle restricts spin-singlet pairs to s or d orbital states and the spin-triplet state to a p orbital state.

Two times the energy gap is the binding energy of a Cooper pair (energy required to break the paired state), and the gap magnitude at zero temperature, $\Delta(0)$ is related to the superconducting transition temperature T_c by

$$2\Delta(0) = 3.52 k_B T_c, \tag{1.8}$$

where k_B is the Boltzmann constant. At low temperature (below T_c), $k_B T$ is smaller than the gap and hence the superconducting electrons are not excited by the thermal vibrations of the lattice. The temperature dependence of the *BCS* energy gap shows that $\Delta(T)$ falls to zero at T_c, analogous to the behaviour of the GL order parameter ψ. For this reason, the terms "order-parameter" and "gap function" are often used with the same meaning.

The temperature dependence of the energy gap at temperatures near the critical temperature is described by the formula [26]

$$\frac{\Delta(T)}{\Delta(0)} \approx 1.74\sqrt{1 - T/T_c}, \tag{1.9}$$

1.2.3 Clean and Dirty *BCS* Model

The *BCS* model can be applied both on clean and dirty limits depending on the purity of the superconducting materials. The terms clean and dirty originate from the comparison of the isotropic *BCS* energy gap 2Δ with the normal-state scattering rate $1/\tau$, where τ is the mean free time between ionic collisions. For $1/\tau \ll 2\Delta$, the superconducting system is considered in the clean limit, while for the dirty limit, $1/\tau \geq 2\Delta$. The scattering rate increases as the system becomes more and more disordered. This disorderness may come from the presence of any impurity or inhomogeneity in the system. The clean and dirty limits may also be expressed as $l \gg \xi$ and $l \leq \xi$, respectively, where l is the quasiparticle mean-free path and ξ is the *BCS* coherence length. So far, we have discussed the *BCS* gap function in the clean limit only [see section 1.2.1]. The details about the temperature dependence of the gap function in the dirty limit are described in section 7.8.

1.2.4 Multiband Superconductivity

According to the *BCS* theory of superconductivity, all the electrons on an isotropic Fermi surface (FS) contribute equally to the superconducting pairing, giving a constant superconducting gap Δ. However, different scenarios can arise when the FS

has multiple bands, i.e., different bands with more or less itinerant electrons overlapping on the FS. In this case, electrons from different bands of the FS contribute to the superconductivity of a material. The simplest form of multiband superconductivity arises when electrons on different FS have different electron-phonon coupling strengths leading to different superconducting energy gaps. The different values of Δ on different sheets of the FS was considered theoretically back in the late 1950s [27]. Recently, this has emerged as a possible explanation for the unusual physical properties observed in different unconventional superconductors, such as MgB_2 [28], YNi_2B_2C [29, 30], and $Lu_2Fe_3Si_5$ [31].

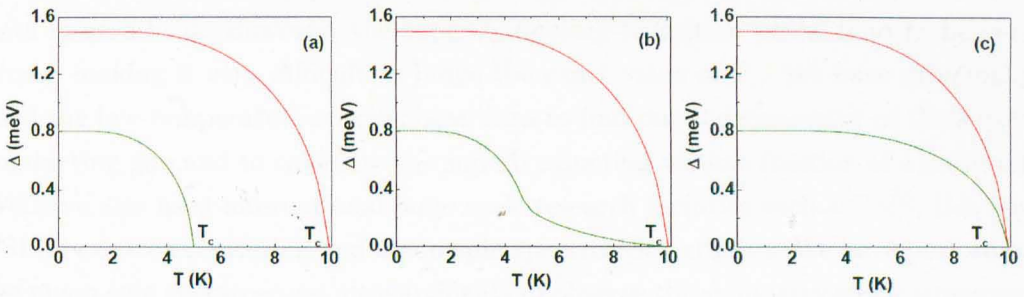

Figure 1.4: Superconducting gap parameters for (a) weak, (b) intermediate, (c) relatively strong coupling multi-band superconductor. The red and green lines represent the larger and the smaller bands, respectively.

According to the two-band model, the coupling strength between the bands depends on their relative compatibility for pair exchange. For weak inter-bands coupling, the superconducting bands will behave independently and have separate critical temperatures [see Fig. 1.4 (a)]. On the other hand, if the coupling strength is strong, the smaller band will prefer the T_c of the larger band. This behaviour is shown in Fig. 1.4 (c). An intermediate scenario can also be imagined and shown in Fig. 1.4 (b). We have investigated all these different multiband/multigap natures of the superconducting order parameters in different unconventional superconducting systems using low temperature specific heat and muon spin spectroscopy measurements.

In this thesis we have investigated the unusual properties of different superconducting systems. These are $FeTe_{0.5}Se_{0.5}$, $FeTe_{1-x}S_x$ ($0.10 \leq x \leq 0.50$), $Lu_2Fe_3Si_5$, CaAlSi, ZrB_{12} and two different superconducting phases of Re_3W. All these superconductors are unconventional in nature as they show different exotic properties which cannot be explained by a simple BCS model. Each of these materials has been briefly introduced in the starting of the corresponding chapters. We

have prepared single crystal or polycrystalline samples of all these material and performed in house measurements to study magnetic, thermodynamic and transport properties. Using magnetization, resistivity and specific heat, we can detect the superconducting transition temperature, T_c. However, finding out the exact T_c of a superconductor is more difficult from magnetization and specific heat compared to the resistivity measurement. For example, in magnetization measurements, we always need to apply some small field, hence we do not get the exact T_c which is defined as the ordering temperature in zero field. We have primarily used the magnetization data to calculate the lower and upper critical fields and also to check the amount of magnetic impurities. For specific heat meausrements, we can take the data in zero field. However, the superconducting transition peaks tend to be very broad, making it very difficult to judge the exact value of T_c. We have principally used the low-temperature specific heat data to find out the symmetry of the superconducting gap and to calculate the superconducting volume fraction of a material. We have also used international large scale research facilities such as ISIS, ILL and PSI for neutron scattering and muon spin spectroscopy studies. We have performed the muon spin spectroscopy measurements to observe the symmetry of the superconducting gap and compare it with the specific heat results. This technique can also be used to calculate the London magnetic penetration depth at absolute zero. Small angle neutron scattering measurements have been done to observe directly the FLL and to investigate its symmetry in the mixed state of a Type-II superconductor.

1.3 Thesis Overview

Chapter 2 introduces all the experimental techniques we have used through out this thesis. In chapter 3, we show the superconducting properties of the iron chalcogenide superconductors. Good quality polycrystalline and single crystal samples of $FeSe_{1-x}Te_x$ ($0 \leq x \leq 0.75$) and $FeTe_{1-x}S_x$ ($0.10 \leq x \leq 0.50$) have been grown successfully using the self-flux method. These compounds have been characterized through X-ray diffraction, EDX, transport, magnetization and specific heat measurements. We have successfully performed a transverse-field muon spin rotation (TF-μSR) study on a polycrystalline sample of superconducting $FeTe_{0.5}Se_{0.5}$ using MuSR at ISIS. The temperature dependence of the magnetic penetration depth, $\lambda(T)$, of $FeTe_{0.5}Se_{0.5}$ is compatible with a two gap $s + s$-wave or an anisotropic s-wave model. We have also performed μSR studies on polycrystalline samples of $FeTe_{1-x}S_x$ ($0.10 \leq x \leq 0.50$) and found the coexistence between superconductivity and antiferromagnetism in this system.

In Chapter 4, superconducting properties of $Lu_2Fe_3Si_5$ have been investigated using low-temperature TF-μSR and specific heat measurements. The magnetic penetration depth at zero temperature, $\lambda(0)$, is estimated to be 353(1) nm. $\lambda(T)$ of $Lu_2Fe_3Si_5$ is consistent with a two gap s+s-wave model. Low-temperature specific heat measurements on the same sample also show evidence of two distinct superconducting gaps.

In chapter 5, the flux line lattice in CaAlSi has been studied by small angle neutron scattering. A 30^o lattice reorientation has been observed between fields of 97 and 294 Oe. This reorientation transition appears to be first-order in character and can be explained well by non-locality effects. The microscopic parameters such as λ and ξ of CaAlSi have been estimated by fitting the field dependence of the form factor data.

In chapter 6, the superconducting phase diagram of ZrB_{12} has been mapped out using μSR measurements. The local field distribution for different applied fields and temperatures shows evidence of the Meissner, mixed, and intermediate states in ZrB_{12}. The intermediate state indicates that the material has the characteristics of a Type-I superconductor, while the mixed state is typical of a Type-II superconductor. Regions of coexistence have also been observed between the different states.

Chapter 7 presents the superconducting properties of the two superconducting phases of Re_3W by powder neutron diffraction, magnetization, resistivity, specific heat and μSR measurements. One phase crystallizes in a non-centrosymmetric α-Mn structure and has a superconducting transition temperature, T_c, of 7.80 ± 0.05 K. The other phase has a hexagonal centrosymmetric structure and is superconducting with a T_c of 9.40 ± 0.05 K. Switching between the two phases is possible by annealing the sample or remelting it. All these properties make Re_3W a very useful system in which to explore any differences in the superconducting states generated by the different crystallographic structures.

Chapter 2

Experimental Techniques

2.1 Sample Growth Techniques

2.1.1 Polycrystalline Sample Growth

All the samples were grown using the in-house facilities available at Warwick. To grow a new material, people generally start with growing a polycrystalline sample. It is also possible to perform lot of bulk measurements using polycrystalline samples. To grow a single crystal, it is essential to grow good quality polycrystalline samples for the starting material. We have used two different techniques to grow polycrystalline samples:

Solid State Reaction Method

In the solid state reaction method, the sample growth is carried out by mixing and grinding together all the required elemental powder materials in stoichiometric ratios, followed by making a pellet and then furnace heating at a controlled temperature. Sometimes, the pellet was sealed in a quartz tube under high vacuum to reduce any reaction with air, especially oxygen. Typically, the process of grinding and heating is repeated several times to make sure that the sample is homogeneous.

Arc Melting Method

Polycrystalline samples were also made using a tri-arc furnace. In this method, all the elemental materials are placed on a water cooled copper hearth. An arc is created by applying a very high DC current to the electrode of the furnace. The melting process is carried out under an Ar atmosphere. The ambient inert-gas atmosphere is Ti-gettered before melting the sample to absorb any remaining

oxygen. The samples are flipped and remelted several times in order to improve the uniformity. Sometimes, individual materials (of low vapour pressure) are melted separately before melting together to check if there is any weight loss during the melting process. We have successfully grown polycrystalline samples of $Lu_2Fe_3Si_5$ and Re_3W using this method.

2.1.2 Single Crystal Growth

In polycrystalline materials, the properties of the grain boundaries often manifest themselves more strongly than the properties of the material itself. Hence, it is sometimes crucial to obtain a good quality single crystal to study the properties of a material more precisely. It is also very useful to study any anisotropic behaviour of a material and this can only be performed in single crystals. Additionally, for neutron scattering studies, large single crystals are necessary. We have used three different methods to grow single crystals:

Flux Growth Method

The flux growth method is in principle very simple. The material in a polycrystalline form is mixed with a suitable solvent and melted. Then the solution is slowly cooled and the material crystallizes with spontaneous nucleation without any preferential nucleation sites. However, there are a few drawbacks in growing a crystal using this method. The crystals which are obtained by this method are commonly very small and very often it is difficult to separate the crystals from the solvent. It is also very important to avoid contamination from the crucible material and the solvent.

Crystals can be grown even without any external flux, where part of the materials work as a self-flux. This method is called the self-flux growth method. Single crystals of $FeTe_{0.5}Se_{0.5}$ and $FeTe_{1-x}S_x$ were grown using this method. Here, FeSe and FeS are used as a self-flux in the growth process of $FeTe_{0.5}Se_{0.5}$ and $FeTe_{1-x}S_x$, respectively.

Bridgman Method

The Bridgman method is a technique for growing a single crystal from a molten solid. The method involves heating a polycrystalline material above its melting point and slowly cooling it from the lower end of its container to start nucleation. Figure 2.1 shows a schematic of a Bridgman furnace. It works with three temperature zones. The temperature in the upper zone is the highest. The polycrystalline samples are melted in this zone. The temperature in the lower zone is kept below the melting

point of the materials. An adiabatic zone is established in the middle to stabilize the melt.

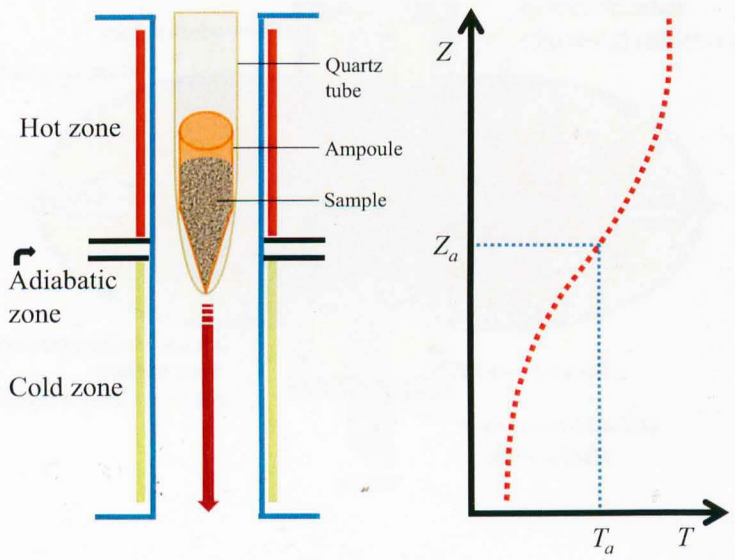

Figure 2.1: Schematic of a vertical Bridgman furnace. The graph in the left is the temperature profile of the Bridgman furnace along the vertical axis.

An ampoule with a conical shape bottom containing the polycrystalline materials is raised into the upper zone. The conical shape of the bottom is to help nucleation during crystal growth. The sample is melted in the upper zone with high enough temperature and then allowed to stabilize for about 24 h. The ampoule is slowly lowered into the cold zone with lowering speeds of the order of 1 to 10 mm/h. The crystal starts growing from the bottom of the ampoule. Single crystals of CaAlSi were grown by Dr. Da-Qian Liao using this method.

Optical Floating Zone Method

The optical floating zone technique is based on the zone melting principle. This method is the cleanest for growing single crystals as it does not use a crucible and hence reduces possible contamination. Figure 2.2 shows a schematic of a 2 mirror image furnace used in an optical floating zone method. We have also used a 4 mirror image furnace.

The heat supplied to the molten zone is provided by two/four halogen lamps. Light from these lamps are focused by the semi-ellipsoidal mirrors onto a central zone

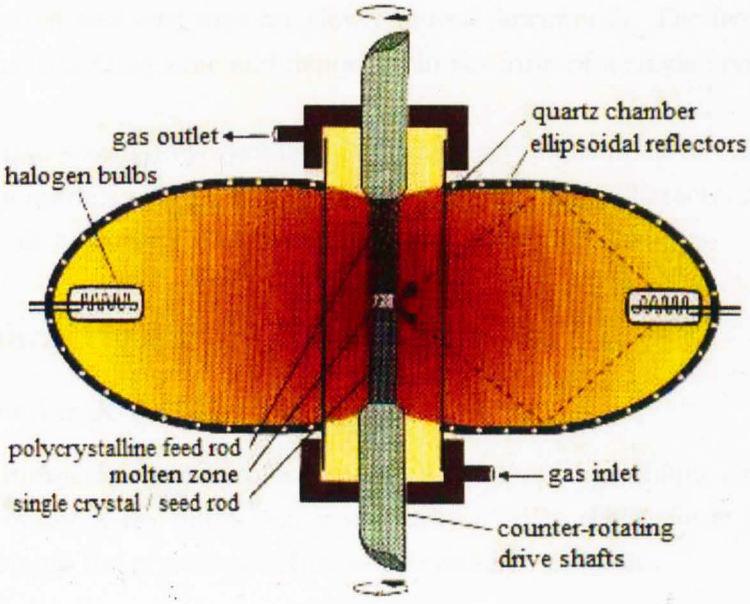

Figure 2.2: Schematic of an optical floating zone furnace. The light is focused by the semi-ellipsoidal mirrors onto a central zone where the seed and feed rods are brought into contact. Rotations of the two rods are performed to obtain a more homogeneous melt.

between two solid rods (called the seed and the feed rods) to make a molten zone which is held in place by its own surface tension. Normally, both the seed and the feed rods are made of polycrystalline materials. However, sometimes, a small part of a single crystal (if available) is used as the seed rod for better crystal quality. The growth process takes place inside a quartz tube, which allows for the use of different inert, oxidizing or reducing atmospheres. Movements of the mirrors, seed rod, feed rod and rotation of both seed and feed rods can be controlled independently. The melt temperature during growth can be precisely controlled by the applied lamp power but can not be measured directly. The stability of the molten zone is usually controlled by visual observation and manual adjustments of the lamp power. We have used this method to grow the single crystal of ZrB_{12}. An image of the single crystal of ZrB_{12} is shown in section 6.2.

This method also enables the growth of materials which do not melt congruently. In order to grow such materials, a solution (flux) with low melting point is used between the feed material and the seed rods. Thus, the processing temperature

can be kept well below the decomposition point of the material grown. During the process, the feed and seed rods are slowly moved downwards. The feed material is dissolved in the melting zone and deposited in the form of a single crystal onto the seed rod.

We have grown polycrystalline and single crystal samples of different superconducting materials using the above mentioned methods. Characterizations of all these materials have been performed using the following techniques.

2.2 Characterization Techniques

2.2.1 Powder X-ray Diffraction

The X-Ray diffraction pattern of a crystalline substance is a unique signature for a material. Powder X-ray diffraction is primarily used to check phase identification and to determine the crystal structure of a crystalline material.

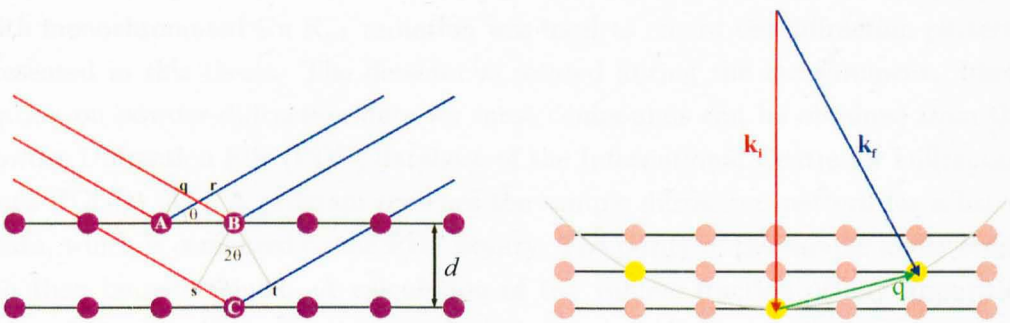

Figure 2.3: The diffraction process in real (left) and reciprocal (right) space. Parallel monochromatic x-rays (red) are incident on planes of atoms (purple spheres). The in-phase scattered rays are shown in blue. In reciprocal lattice space, a plane of atoms are denoted by a single point (pink sphere). Only those reciprocal lattice points that are intersected by the Ewald sphere (yellow spheres) satisfy the Bragg condition.

Incident X-rays are scattered by a sample [see Fig. 2.3] according to Bragg's law

$$n\lambda = 2d\sin\theta, \tag{2.1}$$

where n is an integer, λ is the wavelength of the X-ray beam, θ is the acute angle between the incident ray and the scattering planes, and d is the distance between

the crystal planes. A diffraction pattern is obtained by measuring the intensity of scattered waves as a function of scattering angle (2θ). For more details, see Ref. [32].

The diffraction process can also be described in terms of a reciprocal space lattice which is simply the Fourier transform of the real space lattice. Planes of atoms (with inter planar distance d) in real space are described by points in reciprocal space at a distance of $2\pi/d$ from the origin in a direction perpendicular to the original reflecting planes. If the incident beam is plotted in a direction parallel to its real space equivalent, with a length of $k = 2\pi/\lambda$ Å^{-1}, terminating at the origin of the reciprocal crystal lattice, the three dimensional locus of the wave vectors with the same length and origin as $\mathbf{k}_i$ will indicate $\mathbf{k}_f$ as the outgoing wave vector. The scattering vector is then $\mathbf{q} = \mathbf{k}_f$ - $\mathbf{k}_i$. For elastic scattering, the magnitudes of $\mathbf{k}_i$ and $\mathbf{k}_f$ are equal and all possible configurations of $\mathbf{k}_f$ will construct a sphere, called the Ewald sphere. A two dimensional image of an Ewald sphere is shown on the right hand side of Figure 2.3. Only the reciprocal lattice points that intersect with the Ewald sphere will satisfy the Bragg condition and contribute to the scattering.

A *Panalytical X'Pert Pro multipurpose* X-ray diffraction system (MPD) [33], with monochromated Cu $K_{\alpha 1}$ radiation was used to record the diffraction patterns presented in this thesis. The detector is rotated during the measurement. Information on powder diffraction data for most compounds can be obtained from the Powder Diffraction File (PDF) database of the International Centre for Diffraction Data (ICDD) [34]. A program searches the sample diffraction pattern for a list of peaks, which is compared to the PDF library. The purity of the sample under study can then be ascertained. A calculation of the volume fraction of any impurities is made possible by comparing the intensity ratios of the strongest peaks in the diffraction patterns.

2.2.2 Laue Diffraction

The Laue method is mainly used to determine the orientation of a single crystal. The Laue diffraction pattern can be obtained by two different methods, back-reflection and transmission Laue method. We have used the back-reflection Laue method. Here, a polychromatic source with a range of wavelengths is used to probe the whole plane of reciprocal space in a single measurement. An incident X-ray is fired onto the single crystal through the centre of a scintillator screen. The crystal then backscatters the X-ray towards the screen. Images on the screen are recorded using a *Photonic-Science* charge-coupled device (CCD) connected to a computer. Samples are mounted on a triple-axis goniometer which allow rotation and translation in each axis/direction to be remotely controlled from a computer. The exposure times and

number of images recorded can also be manipulated from the computer using the Image-Pro Express software. For more details about this technique, see Ref. [35].

2.2.3 Single Crystal X-ray Diffraction

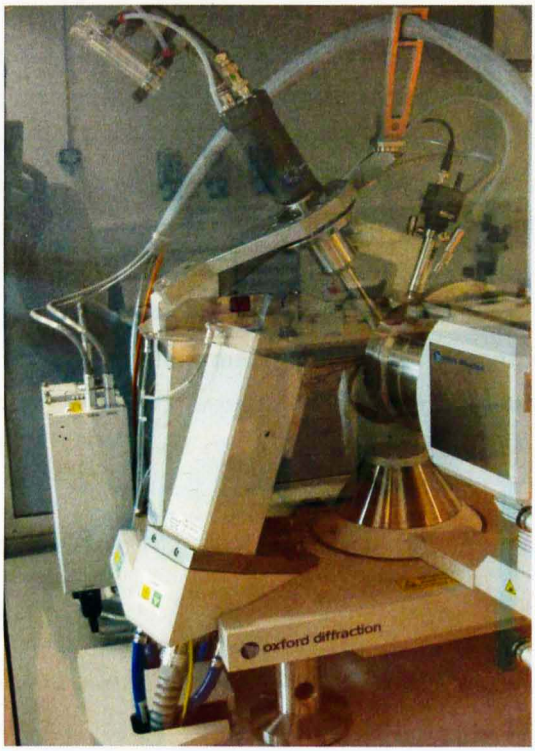

Figure 2.4: An Oxford Diffraction CCD single crystal diffractometer. The figure shows the sample on a four-circle goniometer, the cryo-jet, X-ray source, CCD and beam stop.

Single-crystal X-ray Diffraction is a non-destructive analytical technique which provides detailed information about the internal lattice of crystalline substances, including unit cell dimensions, bond-lengths, bond-angles, and details of site-ordering. At Warwick, we have used a Gemini R diffractometer [see Fig. 2.4] [36] with Mo Kα radiation to study the superstructure of the single crystal of CaAlSi [results are discussed in section 5.3]. The detector is a 135 mm diameter Ruby CCD area detector, which allows for extremely fast data collection of the entire Ewald sphere. A kappa-geometry goniometer moves the sample so that the majority of reciprocal space can be accessed. The parameters for a run, including the step size and X-ray voltage are optimized for a particular sample by performing a pre-experiment. Measurements at temperatures from 80 to 400 K are possible through use of a cryo-jet.

Data reduction and cell refinement were carried out using *CrysAlisPro* [37].

2.2.4 Energy Dispersive Analysis using X-rays

Energy Dispersive X-Ray spectroscopy (EDX), also referred to as EDS or EDAX, is an x-ray technique used in conjunction with scanning electron microscopy (SEM) to identify the elemental composition of a materials. A beam of electrons interacts with the sample and an electron from an inner atomic shell may be excited to an outer shell while creating an electron hole where the electron was. A higher energy electron then fills the hole and energy is given off in the form of an X-ray. The energy of that X-ray will be characteristic of the energy difference between the two energy levels, and so characteristic of the electronic structure of the element involved. The data generated by EDX analysis consist of energy spectra showing peaks corresponding to the elements making up the true composition of the sample being analyzed. For more details, see Ref. [38]. We have used this technique to analyze the composition of different constituents in the $FeTe_{1-x}S_x$ system.

2.3 Magnetic and Physical Properties Measurements

2.3.1 Magnetization

The bulk magnetization measurements presented in this work were performed using a SQUID (Superconducting Quantum Interference Device) magnetometer, part of *Quantum Design*s Magnetic Property Measurement System (MPMS) [39], shown schematically in Figure 2.5. This instrument is very sensitive to a tiny magnetic signal, making it ideal for measuring subtle changes in the magnetic behaviour of a sample when it is subjected to different temperatures, magnetic fields or pressures.

The temperature dependence of the magnetization can be measured in two different applied field situations. These are called zero-field cooled (ZFC) and field cooled (FC) modes. A ZFC measurement involves the sample being cooled from the high temperature paramagnetic state to base temperature before a magnetic field is applied to the sample. In a FC measurement, the field is applied beforehand. There can be a significant difference between the ZFC and FC data depending on the nature of the magnetic order present in a material.

The SQUID Magnetometer

The SQUID magnetometer comprises of a second-order gradiometer (counter-wound pick-up coils) connected to two parallel Josephson junctions in a superconducting

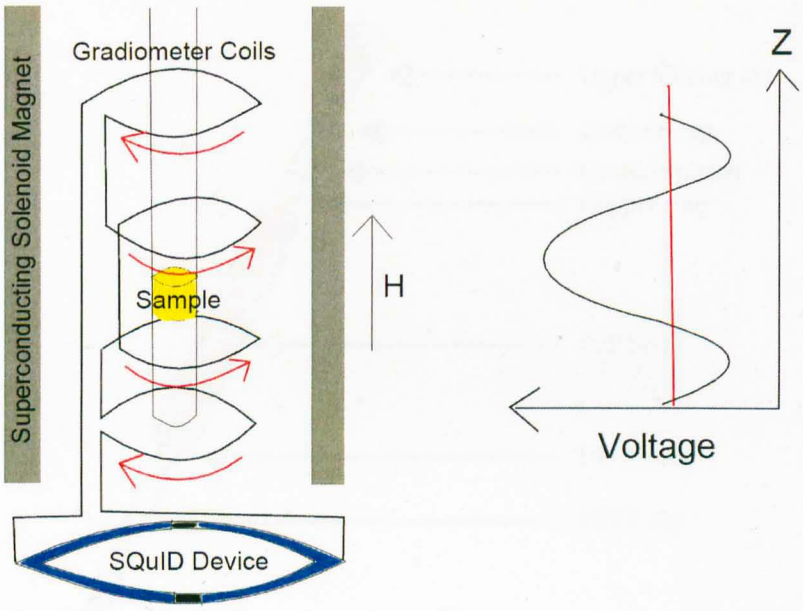

Figure 2.5: A schematic diagram of a *Quantum Designs* SQUID magnetometer. The sample is scanned along the z direction through the pick-up coils. The change in current is detected by the SQUID sensor, based on superconducting loops containing Josephson junctions and yield a voltage response. The measured voltage response curve is fitted and a value of the magnetization computed from the fitting.

ring. The sample is mounted in a non-magnetic sample holder and then placed on the end of a non-magnetic sample rod between the pick up coils. The movement of the sample through the gradiometer induces a current in the coils due to Faraday's law of electromagnetic induction. The SQUID then functions as an extremely sensitive current to voltage converter, outputting the change in magnetic flux measured by the pick-up coils as a dipole voltage response. The SQUID voltage is then measured at a number of sample positions along the scan length. This SQUID response is fitted to the theoretical signal from a point-source magnetic dipole using either iterative or linear regression algorithms, and the moment of the sample is then extracted. SQUID magnetometers are capable of measuring very small magnetic moments. The instrument used in this work has a resolution of 5×10^{-8} emu. Magnetization measurements can be performed with an external magnetic field up to 70 kOe (using a superconducting magnet) and a temperature range between 1.9 to 400 K.

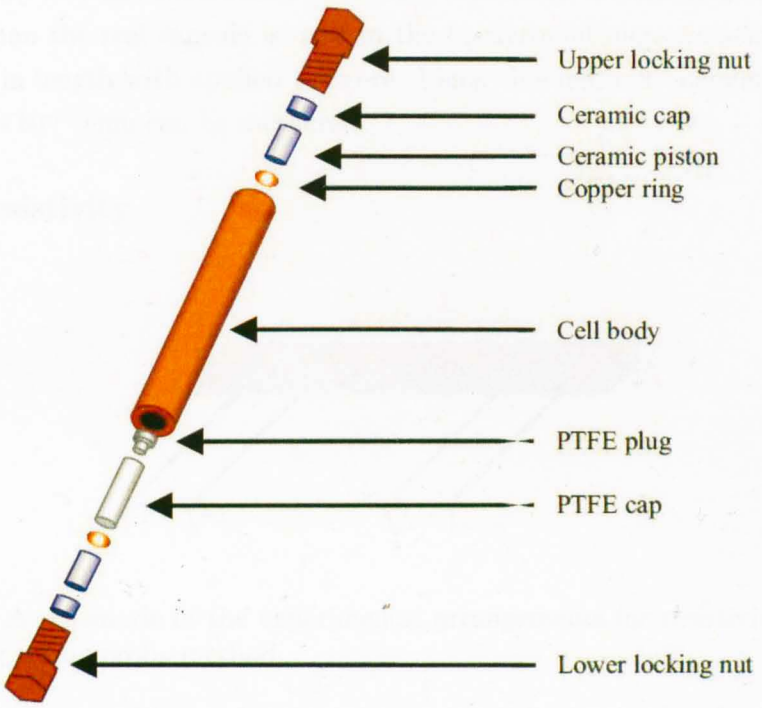

Figure 2.6: A schematic of the Mcell10 hydrostatic pressure cell.

Magnetization Under Pressure

Magnetization measurements under external pressures of up to 10 kbar were made using the easyLab Mcell 10 hydrostatic pressure cell. The cell is designed specially for use with the *Quantum Design* MPMS SQUID magnetometer. A schematic diagram of the pressure cell is shown in Figure 2.6. The sample is loaded in a PTFE capsule filled with Daphne oil (the pressure transmitting medium). The hydrostatic pressure is generated inside the capsule via two ceramic pistons using a hydraulic press, and maintained by tightening the end locking nuts. The sample space is approximately 1.9 mm in diameter and 10 mm long. A small piece of Sn is also placed in the capsule. The superconducting T_c of Sn is well known as a function of pressure, and therefore the *in-situ* pressure can be measured using the Sn manometer. Background signals are subtracted simultaneously using the automatic background subtraction feature of the MPMS magnetometer, in which the voltage response curves for the empty cell recorded at the relevant temperatures and fields are subtracted from the total voltage response from the cell plus the sample. The fit of the difference curve therefore gives the value of the moment of the sample. In

order to carry out this subtraction procedure effectively, a dummy capsule shorter in length than the real capsule is used in the background measurements to mimic the change in length with applied pressure. Using this method, magnetic moments as low as 1×10^{-5} emu can be measured.

2.3.2 Resistivity

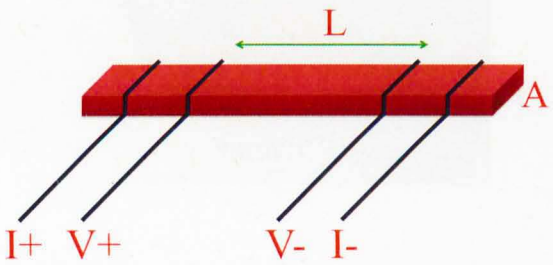

Figure 2.7: A schematic of the experimental arrangements for resistivity measurements using a four probe method.

Resistivity measurements were performed in a *Quantum Design* Physical Properties Measurement System (PPMS) under applied fields of up to 90 kOe and a temperature range of 1.8 - 400 K, using a standard four-probe method. Four electrical contacts on the sample were made with fine silver wires fixed to the surface of the sample by silver epoxy. A schematic of a four probe technique is shown in Fig. 2.7. Here, L and A are the seperation length between the two inner probes and cross section area, respectively. The resistivity ρ, of a long parallelopiped can be defined as

$$\rho = \frac{RA}{L}, \tag{2.2}$$

where, $R = V/I$, V is the voltage and I is current measured through the sample.

2.3.3 Heat Capacity

Specific heat measurements were performed using a two-tau relaxation method in a *Quantum Design* PPMS. An image of the sample holder (puck) is shown in Fig. 2.8. The sample is attached to the stage by standard cryogenic grease such as Apiezon N or H Grease to ensure good thermal contact. The sample platform (stage) is suspended in the centre of the puck by eight thin wires that serve as the electrical

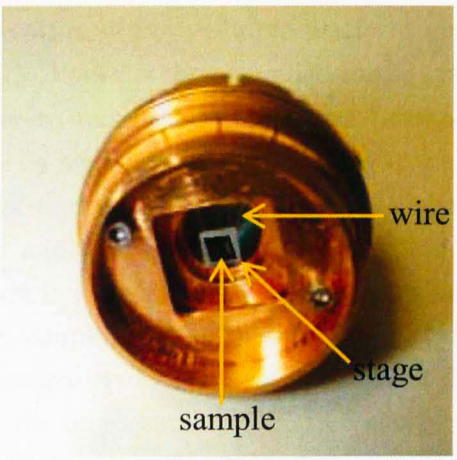

Figure 2.8: An image of the experimental arrangements of the sample puck for heat capacity measurements using relaxation method.

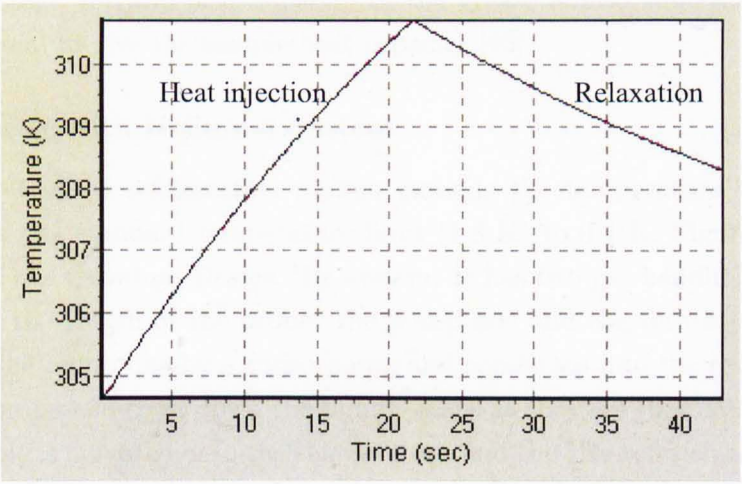

Figure 2.9: The black line is the plot of the heat injection to the sample and the relaxation over time. The red dotted line is the two-tau model fit to temperature relaxation curve.

leads for an embedded heater and thermometer. The wires also provide a well-defined thermal connection between the sample platform and the puck. The puck is then inserted into the PPMS, which is equipped with a 90 kOe magnet and capable of a temperature range of 1.8 to 400 K. To minimize the heat lost via

exchange gas, the sample chamber is maintained at a very low pressure ($\approx$ 0.01 μbar). First, the temperature of both sample platform and puck are stabilized at an initial temperature, T_0. Power is then supplied to the platform heater for a given amount of time in order to raise the temperature (around 1 %) of the platform to T_1. Once the heater is switched off, the temperature of the sample platform relaxes back to the puck temperature, T_0. Figure 2.9 shows the plot of the heat injection to the sample and the relaxation as a function of time. The decay of the platform temperature is exponential, with a time constant that depends upon the heat capacity of the sample and the thermal conductance of the wires through which the heat flow is transmitted. The heat capacity at a particular temperature is determined by fitting the temperature relaxation curve.

The two-tau model for measuring heat capacity assumes the sample may not be in good thermal contact with its surroundings [40]. Two time constants are taken from the relaxation times between the sample and sample stage and the sample stage and puck. This is then compared to a relaxation model involving perfect thermal contact between the sample and stage. An addenda heat capacity measurement of the sample stage and the heat capacity of the grease is also subtracted from the measured signal to give the sample heat capacity [40].

Heat Capacity with Helium-3 System

The Helium-3 (^{3}He) refrigeration system extends the temperature range of the PPMS below the standard temperature limit (1.8 K) to 0.4 K. Figure 2.10 shows the image of the *Quantum Design* ^{3}He system. It has two gas-handling lines which run through the length of the probe: the pump line and the return line. ^{3}He gas flows down the pump line by a turbo pump and condenses into the reservoir in the base of the probe and cools down the sample stage as they are thermally connected. After a sample is mounted onto the sample stage and the ^{3}He-refrigerator is inserted into the sample chamber, the PPMS cools the sample chamber to 1.8 K. Once the sample chamber is cold, the ^{3}He-refrigerator is automatically activated and begins to condense ^{3}He. It is a continuously circulating system as it implements a return line that allows ^{3}He to continuously flow back into the reservoir. Hence, there is no limitation on how long the refrigerator will stay cold.

The experimental techniques we have discussed so far are mainly used to study the bulk properties of a material in a macroscopic level. However, to observe the magnetic field distribution inside a material in a microscopic level, we have used μSR technique.

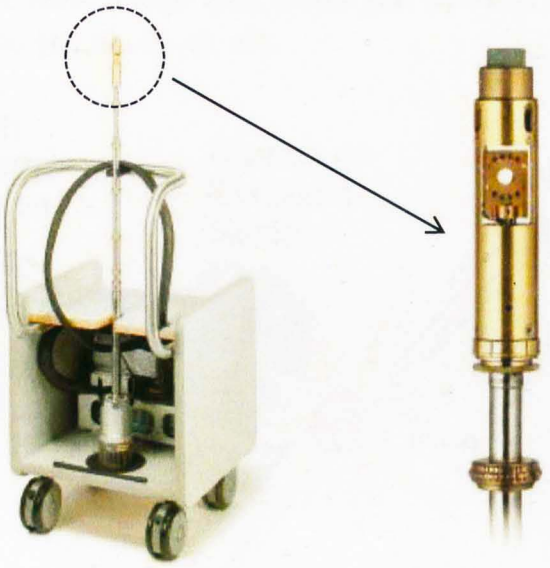

Helium-3 System with probe, diaphragm pump, and cart

Helium-3 probe

Figure 2.10: An image of the *Quantum Design* Helium-3 system. This option is compatible with the Heat Capacity, Resistivity, and AC Transport measurement capabilities.

2.4 Muon Spin Rotation/Relaxation

μSR stands for Muon Spin Rotation/Relaxation/Resonance, where the R is determined by the nature of application of the muon. A muon is a charged spin-1/2 particle with a mass about 200 times that of an electron (or 9 times less than that of a proton). A muon can be considered as a heavier version of the electron. Due to the large magnetic moment (3.18 times bigger than a proton), when a muon is implanted into matter it becomes an extremely sensitive microscopic probe of magnetism. Positive muons (μ^+) are mainly used in condensed matter physics experiments (magnetism, superconductivity, etc). μ^+ avoid the positively charged nuclei in the host material, whereas negative muons (μ^-) implant close to atomic nuclei. Hence μ^- is generally much less sensitive to the phenomena of condensed matter physics, which are essentially the physics of electrons, rather than nuclei. Here, we will only talk about μ^+ as we are only interested in investigating the electronic behaviour of a material. To learn more about μSR and its applications, read the books by Schenck 1985, Schenck and Gygax 1995 [41, 42] and review articles by

Dalmas and Yaouanc 1997, Amato 1997, Hillier and Cywinski 1997, Blundell 1999 and Sonier *et al.* 2000 [43, 44, 45, 46, 47].

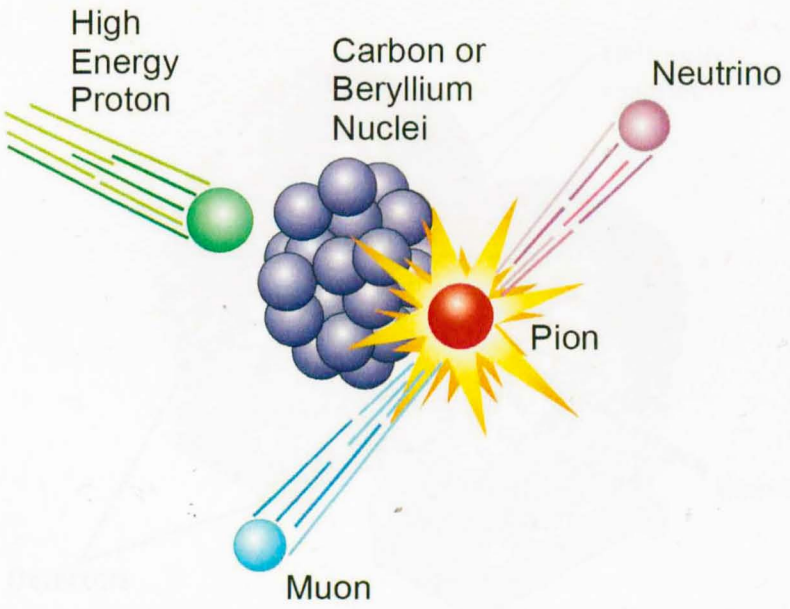

Figure 2.11: Production of muons by firing high-energy protons into a light target (usually graphite).

Low energy muons are produced from ordinary pion decay. High energy protons p (produced using a synchrotron) are fired into a light target (usually graphite or beryllium) to make pions (π^+) [shown in Fig. 2.11] via

$$p + p \rightarrow \pi^+ + p + n, \tag{2.3}$$

and the π^+ decay into μ^+ via

$$\pi^+ \rightarrow \mu^+ + \nu_\mu, \tag{2.4}$$

where ν_μ is a muon-neutrino. In the rest frame of the π^+, the μ^+ and the ν_μ must have equal and opposite momentum to fulfill the momentum conservation law. The π^+ has zero spin and ν_μ has spin 1/2 which is aligned antiparallel with its momentum due to negative helicity. This implies that the μ^+ spin must be opposite to the neutrino spin and hence similarly aligned. Thus by selecting pions which stop in the target, one must produce 100% spin-polarized muons. The muons are stopped in the bulk of a sample and decay after a time t with probability proportional to

$\exp(t/\tau_\mu)$, where $\tau_\mu = 2.2$ μs is the lifetime of the muon. The muon decays into three particles as

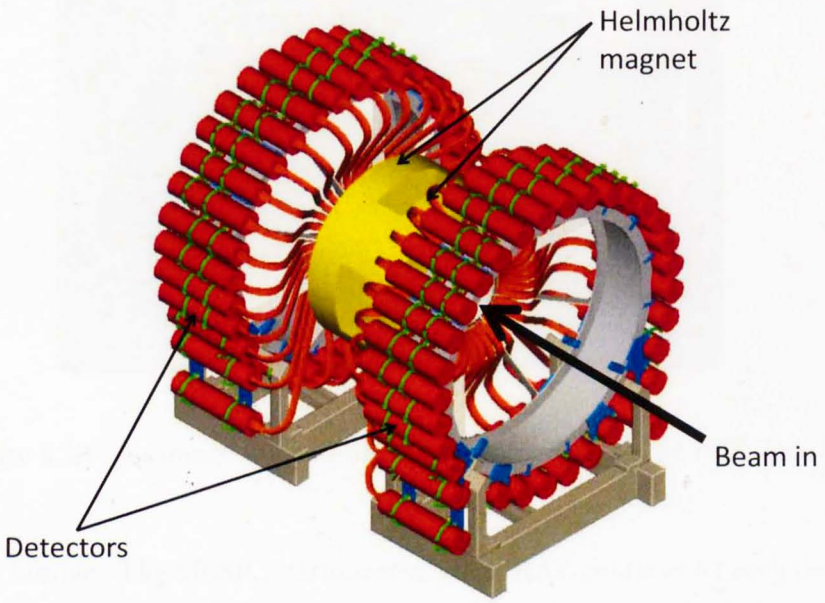

Figure 2.12: One of the suite of μSR spectrometers based at ISIS, RAL. The red cylinders are the detectors and the yellow part is the magnet made of Helmholtz coils. The sample is placed inside the two Helmholtz coils. Beam enter the sample along the axis (of the coils and cylindrically arranged detectors) for the longitudinal field and perpendicular to the axis for the transverse field measurements.

$$\mu^+ \rightarrow e^+ + \nu_e + \bar{\nu_\mu}, \tag{2.5}$$

where e^+ is a positron. The decay involves the weak interaction and thus conserves parity [48]. This phenomenon leads the emitted positron to emerge predominantly along the direction of the muon spin when it decayed. In an experiment, one detects this decay product (basically e^+) and the orientation of the e^+ spin tells one essentially which way each muon-spin was pointing as it decayed. We cannot be certain from a single positron decay along which direction the muon spin was pointing in the sample. However, by measuring the anisotropic distribution of the decay positrons from a collection of muons deposited under the same conditions, one can determine the statistical average direction of the spin polarization of the muon ensemble. Experimentally, this can be detected using scintillation detectors placed

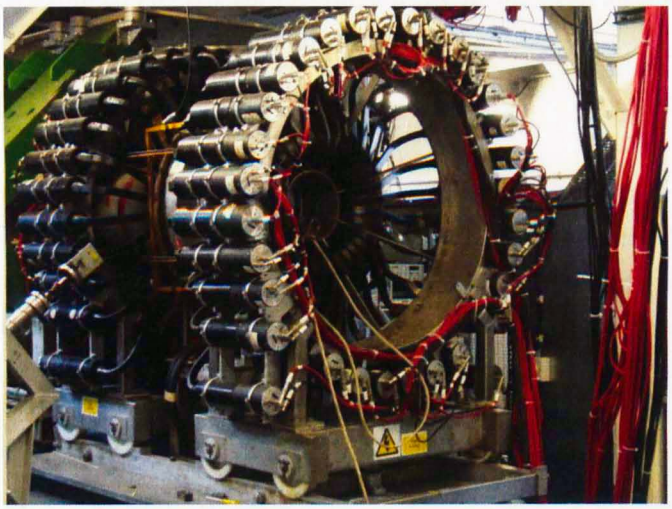

Figure 2.13: An image of the μSR spectrometers based at ISIS, RAL.

around the sample. The MuSR instrument at ISIS, RAL contains 64 such detectors, each consisting of a piece of plastic scintillator joined by an acrylic light-guide to a photomultiplier tube. The detectors are arranged in two arrays around the sample position on a cylinder concentric with the Helmholtz coils of a magnet. A pulse of positive muons is produced every 20 ms with a FWHM of $\sim$ 70 ns. A schematic of the MuSR instrument at ISIS, RAL is shown in Fig. 2.12. A photograph of the spectrometer is shown in Fig. 2.13. When using μSR spectroscopy to study matter, depending on the direction of the applied magnetic field, one has the flexibility of choosing from a number of different experimental configurations. Here, we will only discuss transverse field Muon spin rotation (TF-μSR) and longitudinal field Muon spin relaxation (LF-μSR) as the others are not relevant to my work.

TF-μSR

In this configuration, an external magnetic field is applied perpendicular (transverse) to the initial direction of the muon spin polarization. A schematic of this configuration is shown in the left of Fig. 2.14. The muon spin precesses about the transverse field with a frequency proportional to the strength of the field at the muon site in the material. We have used this technique to measure the internal magnetic-field distribution in the vortex state of a type-II superconductor with a resolution of 0.1 mT. A pulse of positive muons is implanted into the bulk of the superconductor with their initial spin polarization perpendicular to the applied magnetic field. They stop

at interstitial sites due to electrostatic repulsion by atomic nuclei and precess about the local magnetic field $B(r)$ with a Larmor frequency

$$\omega_\mu = \gamma_\mu B(r), \tag{2.6}$$

where $\gamma_\mu/2\pi = 135.5342$ MHz/T is the muon gyromagnetic ratio. In the vortex state of a type-II superconductor, the muons implanted close to the vortex cores experience a larger magnetic field than those implanted between vortices. Due to this variation of magnetic field strength from site to site, different muons will precess at different frequencies and become progressively dephased so that oscillation signals will be damped. The larger the penetration depth, the smaller the magnetic field variation and the less pronounced the depolarization/relaxation rate. Thus the relaxation rate of the precession signal can be used to obtain directly the magnetic penetration depth of a superconductor.

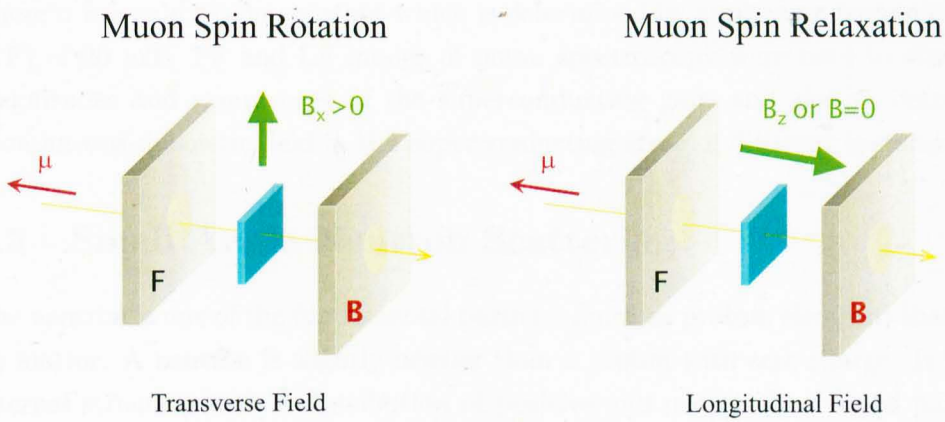

Figure 2.14: Field arrangement in the two MuSR geometries. F and B are the detectors positioned before and after the sample.

LF-μSR

Here, the direction of the external magnetic field is parallel or antiparallel to the initial direction of the muon spin polarization. A schematic of this configuration is shown in the right hand panel of Fig. 2.14. Using this configuration, one can measure the time evolution of the muon polarization along its original direction. Measurements can also be performed in the absence of an external field, called zero field muon spin relaxation (ZF-μSR). ZF-μSR is a very sensitive method of detecting weak internal magnetism, that arises due to ordered magnetic moments, or random

fields that are static or fluctuating with time. The capability of studying materials in zero external field is a tremendous advantage over other magnetic resonance techniques such as nuclear magnetic resonance (NMR) and electron paramagnetic resonance (EPR).

In LF-μSR experiments, positrons are detected and time stamped in the detectors which are positioned before (F) and after (B) the sample. The positron counts $N_{F,B}(t)$ have the functional form

$$N_{F,B}(t) = N_{F,B}(0) \exp\left(\frac{-t}{\tau_\mu}\right)[1 \pm G_Z(t)], \tag{2.7}$$

where $G_Z(t)$ is the longitudinal relaxation function. $G_Z(t)$ is determined using

$$\frac{N_F(t) - \alpha N_B(t)}{N_F(t) + \alpha N_B(t)}, \tag{2.8}$$

where α is a calibration constant which is determined by applying a transverse-field (TF) of 20 mT. TF and LF modes of muon spectroscopy were used to study the magnitudes and symmetries of the superconducting gaps and also to detect any spontaneous magnetic field in the superconducting state of different systems.

2.5 Small Angle Neutron Scattering

The neutron is one of the fundamental particles (such as proton, electron) that make up matter. A neutron is slightly heavier than a proton with zero charge. It has an internal structure with a distribution of positive and negatively charged particles. The neutron is highly penetrating and has a magnetic dipole moment and spin. These properties make the neutron a very useful tool in solid state physics research. Small angle neutron scattering (SANS) is an elastic neutron scattering technique that measures the deviation to small angles (fractions of a degree) of a neutron beam due to the structure of various substances on a mesoscopic scale of about 10 - 1000 nm. The Abrikosov vortex lattice, also called the flux line lattice (FLL), is one of the example systems that fits within this length scale. Due to flux quantization, one unit cell must contain one flux quantum. For a hexagonal FLL, this gives:

$$d = \sqrt{\frac{2\phi_0}{\sqrt{3}B}}, \tag{2.9}$$

where B and d are the internal induction field per unit area and flux line lattice constant, respectively.

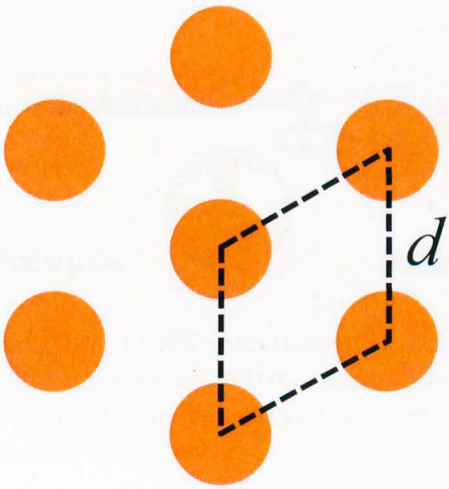

Figure 2.15: Hexagonal FLL symmetry with the unit cell and flux line spacing.

Figure 2.15 shows the hexagonal symmetry of the FLL, including unit cell and flux line spacings. For a relatively high induction, *e.g.* 1 T, the d-spacing is $\approx$ 40 nm. This is at least two orders of magnitude larger than that of the atomic lattice spacings of the host crystal, and indicates that cold neutrons are required to probe this periodicity. To cope with the extremely small momentum transfers (due to the large d-spacing) involved in this type of scattering, SANS instruments utilize long-wavelength ($\lambda_n = 1$ nm) neutrons. Even after using long-wavelength neutrons, the angle of scatter, 2θ, which is given by Bragg law [see Eq. 2.1] is still only of the order of a degree. Hence SANS instruments are also characterised by their large sample-detector distances to separate out diffracted neutrons from the undiffracted main beam.

SANS measurements were performed using the D22 instrument at the Institut Laue-Langevin (ILL), Grenoble, France and the SANS I instrument at the Paul Scherrer Institut, Villigen, Switzerland. Fig. 2.16 shows a schematic diagram of the instrument. Neutrons with a range of wavelengths lying between 3 and 40 Å are used in these experiments. Thus the examination of materials is possible on length scales which are inaccessible with the methods of light scattering. In principle the setup of a small angle experiment is the same as for light scattering. The distance between source and detector, the height of the scattered beam and the resulting

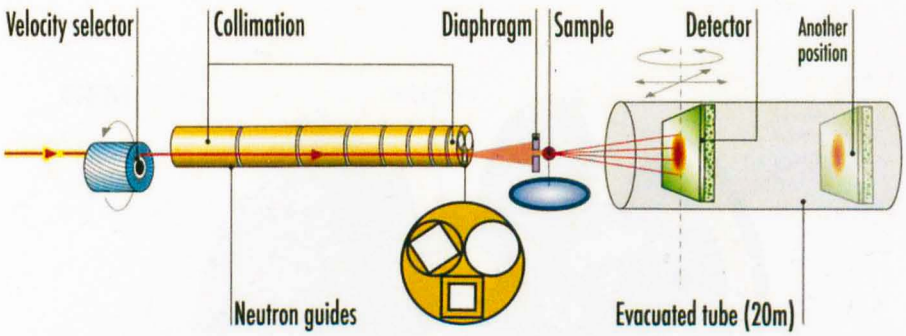

Figure 2.16: A schematic of D22, a SANS instrument at ILL, France. The neutrons are extracted from the cold source by a neutron guide and a wavelength is selected by a mechanical velocity selector. The two other important instrument parameters are the collimation length and the detector distance.

scattering angle characterise the scattering geometry. To monochromate the neutron beam a mechanical velocity selector is used. It consists of a rotating cylinder with helical gaps. Because of the constant velocity of rotation, only neutrons with a specific wavelength are able to pass the cylinder. A collimation section is used to reduce the beam divergence, and is comprised of two pinholes of varying size and separation. The diameter is typically of 16 or 25 mm. At PSI, the collimation length can be varied from 1 to 18 m in one meter increments. For D22, this can be done in steps with size of 17.6, 14.4, 11.2, 8.0, 5.6, 4.0, 2.8, 2.0, and 1.4 m. Two-dimensional ^{3}He-detectors are used to detect the diffracted neutrons which can be positioned at any distance between 1.4 and 20 m from the sample. Both the collimation section and the detector are kept in vacuum to reduce air scattering and beam attenuation. All passages between vacuum and atmosphere were through single crystal sapphire windows to reduce the small angle background signal as much as possible. We have used this technique to observe the vortex state of superconducting CaAlSi.

2.5.1 Powder Neutron Diffraction

The General Materials (GEM) diffractometer [49] at the pulsed neutron source ISIS, RAL is a powder neutron diffractometer. The layout of the GEM diffractometer is shown in Fig. 2.17. GEM can be used to perform high intensity, high resolution experiments to study the crystal structure and magnetic structure of materials, as well as performing structural studies on disordered materials such as glasses and amorphous metals [50]. It has eight detector banks which cover the scattering angle range from 1.1° to 169.3°. The banks contain ZnS/^{6}Li scintillator detectors

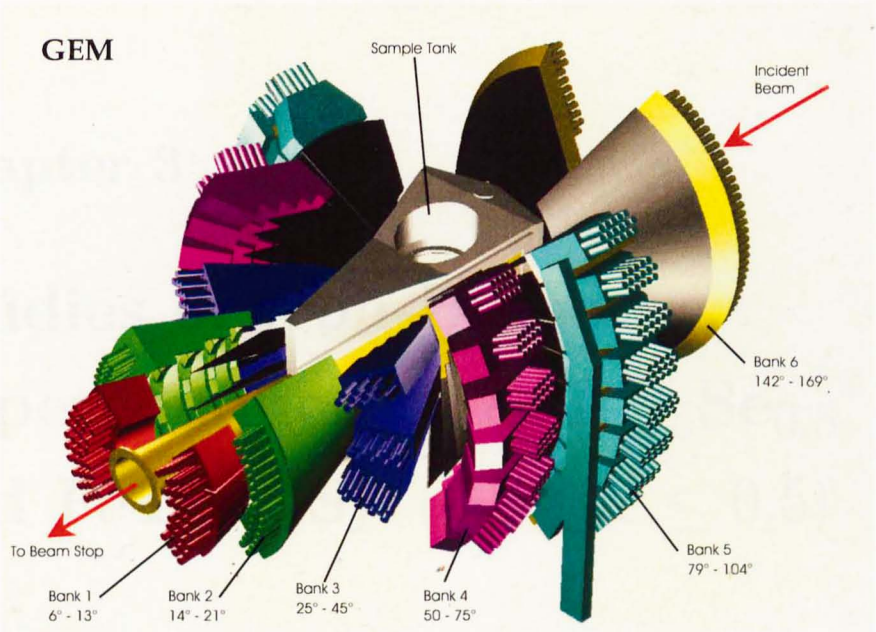

Figure 2.17: Layout of the powder neutron diffractometer GEM at ISIS, RAL.

which are narrow in width (5 mm), giving a high Q resolution. The large number of detectors inside the evacuated sample tank around the sample are engineered in such a way so as to give the highest possible count rate. The neutron flight path and sample tank are evacuated to prevent air scattering. There is a long incident path of 17 m, allowing the flight path and time-of-flight to be well defined. Before reaching the sample, the beam is collimated and a series of choppers define an incident wavelength range (typically 0.05 to 3.40 Å). Neutron powder diffraction experiments were performed to study the crystal structure of the two different superconducting phases of Re_3W. The results were shown in section 7.4.

Chapter 3

Studies of Iron-Based Superconductors $FeTe_{0.5}Se_{0.5}$ and $FeTe_{1-x}S_x$ $(0.1 \leq x \leq 0.5)$

3.1 Iron-Based Superconductors

In 2008, research on high-T_c superconductivity turned in a new direction with the discovery of superconductivity in the iron-based superconductors, $LaFeAsO_{1-x}F_x$ (labelled *1111*, based on the elemental ratios in the chemical formula of the parent compound LaFeAsO), with a T_c of 26 K by Hosono's group [14]. This discovery was preceded by an earlier report of superconductivity at 4 K in LaFePO by the same group [51]. The T_c was soon raised to 43 K, either by replacing La with Sm ($SmFeAsO_{1-x}F_x$) [52], or by applying pressure [53]. Several other *1111* superconductors with $T_c \geq 50$ K have been reported [54], and the current record is 56 K in $Gd_{1-x}Th_xFeAsO$ [15]. Besides the *1111*-type system, four other families of iron-based superconductors have been found, denoted as the *122*-type BFe_2As_2(B=Ba, Sr, or Ca) [55], the *111*-type AFeAs(A = alkali metal) [56], the *11*-type α-FeSe(Te) [57], and the *21311*-type Sr_2PO_3FeAs [58].

The structures of all these families possess the same tetragonal symmetry at room temperature [see Fig. 3.1]. However, the *122* family has a space group *I4/mmm*, while for the rest, the space group is *P4/nmm*. The key ingredient of all these structures is the quasi-two-dimensional layer/slab consisting of a square lattice of iron atoms with tetrahedrally coordinated bonds to either phosphorus, arsenic, selenium or tellurium anions. These slabs are either simply stacked together, as in FeSe, or are separated by spacer layers using alkali (e.g. Li), alkaline

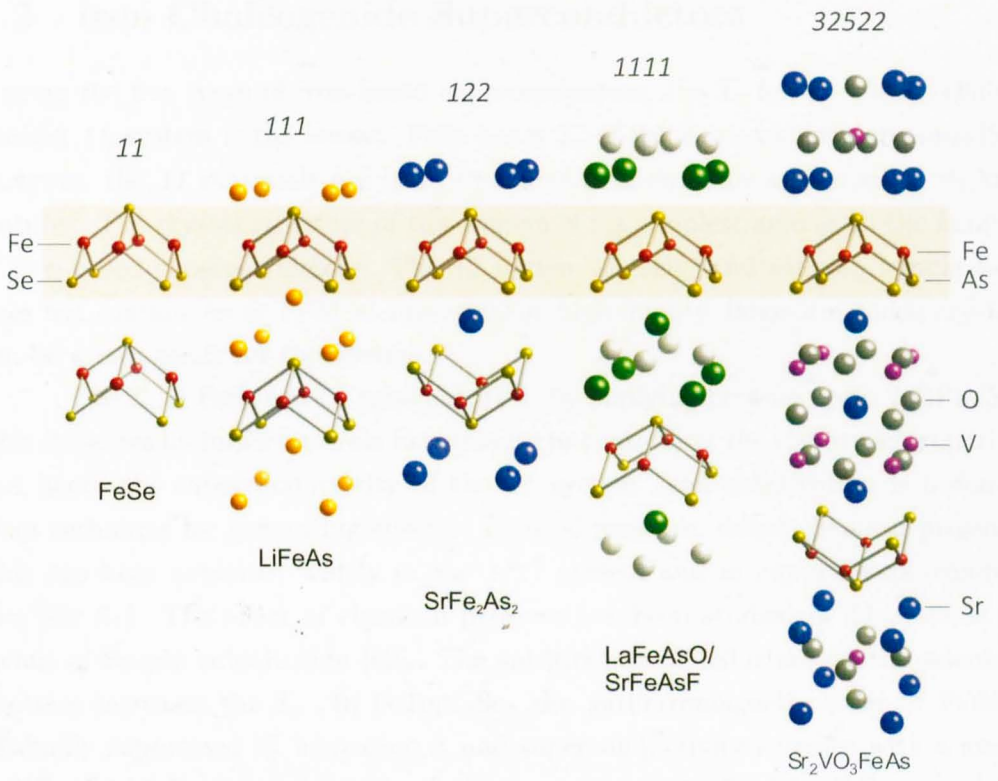

Figure 3.1: Crystallographic structures of the five different families of iron-based superconductors.

earth (e.g. Ba), rare earth oxide/fluoride (e.g. LaO or SrF) or more complicated perovskite-type combinations (e.g. Sr_2O_3). The common FeAs/FeSe building block is considered as a critical component in stabilizing the superconductivity in these iron-based superconductors. All the Fe-based superconductors discovered so far possess some common characteristics of electronic structure. The low-lying electronic excitations are mainly dominated by the five *3d* orbitals which give rise to a couple of hole-like bands near the zone center Γ and electron-like bands near the zone corner M. The qualitative agreement with experiment is also remarkably good. Several angle-resolved photoemission spectroscopy (ARPES) and quantum oscillations measurements confirmed that the predicted band structure composing of hole pockets at the zone center and electron pockets at the zone corners. However, fundamental research and potential applications of those FeAs-based materials may be limited by the presence of the poisonous element As. The discovery of superconductivity in the As-free Fe(Se, Te) compounds (the *11* system) hence constituted exciting progress.

3.2 Iron Chalcogenide Superconductors

Among the five types of iron-based superconductors, the T_c for the Fe-ch (chalcogenide) *11* system is the lowest. FeSe has a T_c of 8.0 K at ambient pressure [57]. However, the *11* materials are still of particular interest for a number of striking features. The crystal structure of this system is the simplest among all the families of iron-based superconductors. The *11* system is easier and safer to handle as it does not contain As or P. Most importantly, high-quality, large-size single crystals can be grown easily for this system.

The T_c of FeSe can be raised to 37 K by applying pressue up to 7 GPa [59]. This indicates an important role for pressure in controlling the electronic properties and hence the superconductivity of the *11* system. Ion substitution is a convenient technique for generating effective internal pressure, called chemical pressure. This has been exploited widely in the *1111* system and in cuprate superconductors [60, 61]. The effect of chemical pressure has been studied in *11* systems by means of Se-site substitution [62]. The substitution of tellurium on the selenium site also increases the T_c. In $FeTe_{1-x}Se_x$ the antiferromagnetic order of FeTe is gradually suppressed by increasing x, and superconductivity emerges with a maximal T_c of 14.5 K at $x = 0.5$ under ambient pressure [62, 63]. Like FeSe, a positive pressure effect was also observed in $FeTe_{1-x}Se_x$. The T_c of $Fe_{1+\delta}Te_{0.43}Se_{0.57}$ gradually increases with the applied pressure and attains a broad maximum of 23.3 K at 23 GPa. Further compression to 12 GPa leads to a metallic but nonsuperconducting ground state. High-resolution synchrotron X-ray diffraction shows that the superconducting phase is orthorhombic at ambient pressure but with a pressure between 2 to 3 GPa, the structure of $Fe_{1+\delta}Te_{0.43}Se_{0.57}$ transforms to a more distorted monoclinic symmetry [64]. This implies that there is a link between the crystallographic and electronic structures of the iron chalcogenide superconductors. Magnetization and resistivity measurements indicate a lower critical field at $T = 0$ K, $H_{c1}(0)$, of between 10 and 80 Oe and an upper critical field, $H_{c2}(0)$, of between 400 and 600 kOe for the $FeTe_{1-x}Se_x$ $(0.25 \leq x \leq 0.5)$ system [65, 66, 67]. Measurements on single crystals indicate that the superconducting properties of this material are anisotropic [66, 67]. All these properties along with the similarity of the Fermi surface to the FeAs based superconductors [68] make the *11* system an ideal candidate to study the structure, magnetism, resistivity, specific heat, symmetry of the order parameter and superconductivity in Fe-based superconductors.

$FeTe_{1-x}S_x$ is another member of the *11* family and is also superconducting with a T_c of 10 K at ambient pressure [69]. Interestingly, the parent compound,

FeTe, is not superconducting and shows antiferromagnetic order at around 70 K. Elemental substitution can sometimes suppress the antiferromagnetic order and induce superconductivity in Fe-based superconductors. For example, this is the case for the compounds of *122* family [55, 70]. A similar scenario has been observed for FeTe, where a small amount ($\leq$ 10%) of S doping on the Te site induces superconductivity [69]. Note, however, the as-grown samples were reported to be either poorly superconducting or non-superconducting. Bulk superconductivity could be induced by immersing the samples into water or alcohol for several days or by annealing in oxygen for 12 h [71, 72, 73]. The solubility limit of the sulfur on the Te site in $FeTe_{1-x}S_x$ is reported to be 12 % [74].

Studies of the iron chalcogenide superconductors provide an excellent opportunity to understand the unconventional superconductivity in these systems which might be helpful to reveal the key ingredient to increase the T_c to a higher value.

3.3 Studies of $FeTe_{0.5}Se_{0.5}$

Soon after the discovery of superconductivity in FeSe with a T_c of 8 K, it was natural to explore whether chemical substitution could increase T_c in this system. A quite immediate choice in this respect was the partial replacement of Se by Te. It was found that the T_c can be raised to a maximum of 14.5 K with a 50 % Te substitution to the Se site.

3.3.1 Sample Growth of $FeTe_{0.5}Se_{0.5}$

A sample of $FeTe_{0.5}Se_{0.5}$ was synthesized in a two-step self-flux method [for more details about the self-flux method, see section 2.1.2] from high purity iron granules (99.999%), selenium shot (99.997%) and tellurium powder (99.999%). First, the appropriate stoichiometric mixture of elements was sealed in an evacuated carbon coated quartz tube (10^{-6} mbar) and heated at a rate of 100 ^{o}C/h to 650 ^{o}C, held at this temperature for 48 h, and then cooled to room temperature at 50 ^{o}C/h. The sample was then heated at a rate of 180 ^{o}C/h to 970 ^{o}C for 24 h and cooled to room temperature at 3 ^{o}C/h. Since the quartz tube often cracked during this cooling, the tube was sealed into a second quartz tube under a high vacuum before the second heating process. Figure 3.2 shows a sample of $FeTe_{0.5}Se_{0.5}$, grown using the above mentioned method.

Figure 3.2: A sample of $FeTe_{0.5}Se_{0.5}$, made by the two-step self-flux method.

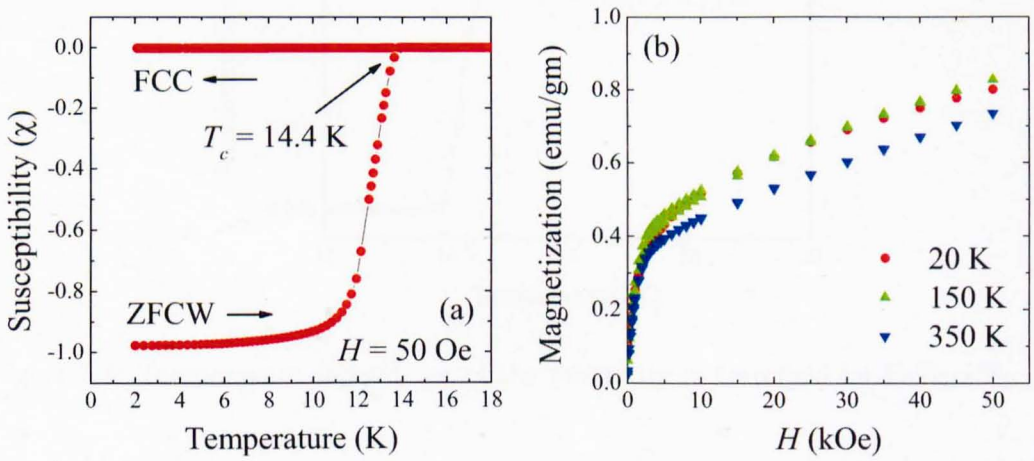

Figure 3.3: (a) Temperature dependence of the magnetic susceptibility of $FeTe_{0.5}Se_{0.5}$ measured using zero-field-cooled warming (ZFCW) and field-cooled cooling (FCC) protocols. The diamagnetic susceptibility corresponds to complete diamagnetic screening with a T_c onset of 14.4 K. (b) Magnetization versus applied field curves for $FeTe_{0.5}Se_{0.5}$ collected above T_c at 20 K, 150 K, and 350 K.

3.3.2 Magnetization Measurements of $FeTe_{0.5}Se_{0.5}$

Magnetization (M) versus temperature (T) measurements carried out in a *Quantum Design* MPMS magnetometer [see section 2.3.1] reveal the sample has a transition

temperature T_c of 14.4 K [see Fig. 3.3 (a)]. The zero-field (ZF)-cooled dc susceptibility approaches a value of -1 while the field cooled signal is 10^{-3} indicating strong pinning in the sample. Magnetization versus applied magnetic field loops collected in the normal state at 20, 150 and 350 K [see Fig. 3.3 (b)] show that the normal state signal is nearly temperature independent and has a response made up of contributions typical of a soft ferromagnet and a Pauli paramagnet. This is consistent with the presence of a small amount of Fe_3O_4 in the sample. Using the published value for the saturation magnetization of Fe_3O_4 [75] we estimate this fraction to be $\sim$ 0.5% of the sample by mass. The magnetization at 50 kOe and 20 K is $\sim$ 30 times smaller than that reported in the sample of $FeSe_{0.85}$ studied by Khasanov *et al.* [76]

3.3.3 Resistivity Measurements of $FeTe_{0.5}Se_{0.5}$

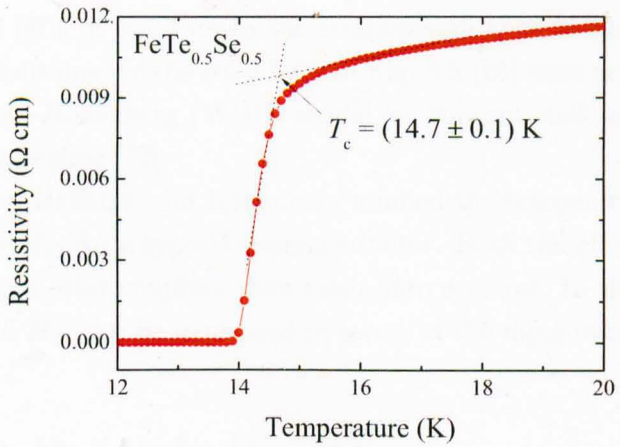

Figure 3.4: Temperature dependence of the resistivity in zero field for $FeTe_{0.5}Se_{0.5}$.

Resistivity measurements were performed using the standard four probe method, see section 2.3.2. Figure 3.4 shows the temperature dependence of the resistivity, ρ(T), of $FeTe_{0.5}Se_{0.5}$ near the superconducting transition. The transition is observed at (14.7 $\pm$ 0.1) K. Figure 3.5 (a) illustrates the effect on the resistive transition for a series of applied magnetic fields (0, 1, 2, 4, 5, 6, 8, 10, 20, 30, 40, 50, 60, 70, 80, and 90 kOe) on $FeTe_{0.5}Se_{0.5}$. The resistive transitions are shifted toward the lower temperatures as the the magnetic field increases. The temperature dependence of the upper critical field, H_{c2}(T), determined from the resistive transitions is shown in Fig. 3.5 (b). Here, ρ_n is the resistivity of $FeTe_{0.5}Se_{0.5}$ just above the T_c. H_{c2}(T) were calculated by collecting the temperatures as the resistivity falls

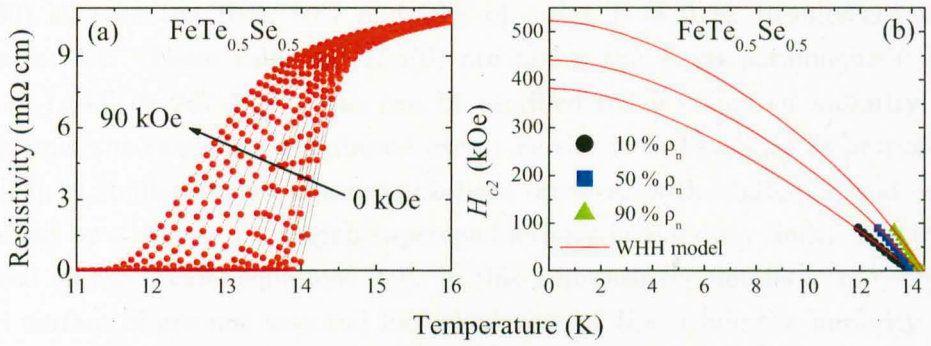

Figure 3.5: (a) Temperature variation of the resistivity in a set of magnetic fields (0, 1, 2, 4, 5, 6, 8, 10, 20, 30, 40, 50, 60, 70, 80, and 90 kOe) for $FeTe_{0.5}Se_{0.5}$. (b) Temperature dependence of the upper critical fields H_{c2} of $FeTe_{0.5}Se_{0.5}$. The solid line is a fit to the data using the WHH model.

to 10%, 50% and 90% of ρ_n. Fits to the temperature dependence of H_{c2} data for three different conditions[see the solid lines in Fig. 3.5 (b)] were achieved within the Werthamer-Helfand-Hohenberg (WHH) model for conventional superconductors in the weak-coupling regime [77].

Werthamer, Helfand, and Hohenberg studied the temperature and impurity dependence of the H_{c2} for a type-II superconductor. Both the effects of Pauli paramagnetism and spin-orbit coupling were taken into account. In the dirty limit, the upper critical field H_{c2} can be expressed in terms of the digamma function:

$$\ln\frac{1}{t} = \left(\frac{1}{2}+\frac{i\lambda_{so}}{4\gamma}\right)\Psi\left(\frac{1}{2}+\frac{\hbar+\frac{1}{2}\lambda_{so}+i\gamma}{2t}\right) + \left(\frac{1}{2}+\frac{i\lambda_{so}}{4\gamma}\right)\Psi\left(\frac{1}{2}-\frac{\hbar+\frac{1}{2}\lambda_{so}-i\gamma}{2t}\right) - \Psi\left(\frac{1}{2}\right), \quad (3.1)$$

where $t=\frac{T}{T_c}$, $\gamma=\left[(\alpha\hbar)^2-\left(\frac{1}{2}\lambda_{so}\right)^2\right]^{1/2}$ and the $\hbar$ is related to H_{c2} by the following function

$$\hbar = -\frac{4H_{c2}}{\pi^2\left(dH_{c2}/dt\right)|_{t=1}}, \quad (3.2)$$

Here, λ_{so} is the spin-orbit scattering strength and α is the Maki parameter. The temperature dependence of the H_{c2} can be fitted by adjusting λ_{so} and α. Using the WHH model, we estimate the values of $H_{c2}(0)$ are 380(20), 440(20), and

520(30) kOe for the 10%, 50% and 90% of ρ_n at $T = 0$ K. Results are shown in Table. 3.1. These values of $H_{c2}(0)$ are above the Pauli paramagnetic limit, $H_{ppl} = 1.84T_c \approx 267$ kOe. This can be ascribed to an enhanced impurity scattering from the randomly distributed excess Fe site in $FeTe_{0.5}Se_{0.5}$ as proposed in Ref. [78]. A similar phenomena has also been observed with MgB_2 [79] and can be explained by a theory of two-gap superconductivity in the dirty limit. The theory is based on the Usadel equations [80]. In this approach the details of the complex Fermi surface of are not essential for calculation of H_{c2}, while the impurity scattering is accounted for by both intraband and interband scattering by nonmagnetic impurities.

Table 3.1: Results for fits to the temperature dependence of the upper critical field of $FeTe_{0.5}Se_{0.5}$ using WHH model.

Model	$H_{c2}(10\%)$ (kOe)	$H_{c2}(50\%)$ (kOe)	$H_{c2}(90\%)$ (kOe)
WHH Model	$38(2) \times 10$	$44(2) \times 10$	$52(3) \times 10$

3.3.4 Heat Capacity Measurements of $FeTe_{0.5}Se_{0.5}$

The heat capacity C of a substance is the amount of heat required to change its temperature by one degree. The specific heat capacity, often simply called specific heat, is the heat capacity per unit mass of a material. In a superconductor, the specific-heat measurements provide a clear signature of the superconducting phase transition. One can estimate the symmetry of the superconducting order parameter from its electronic specific heat below T_c.

The heat capacity was measured using a two-tau relaxation method in a *Quantum Design* Physical Properties Measurement System at temperatures ranging from 1.9 K to 300 K. For details of this technique, see section 2.3.3.

The specific heat (C) of $FeTe_{0.5}Se_{0.5}$ is plotted in Fig. 3.6 in the form of C vs. T. No anomaly is observed from room temperature down to 0.4 K except at the superconducting transition around 14.5 K. In general, materials with more than one type of atom (either different masses of different bonding strengths) may exhibit two types of lattice vibrations (phonons). These may be described as acoustic and optical phonons. For a compound having N atoms per unit cell, one expects 3 acoustical and $3N - 3$ optical phonon modes. The acoustic modes are represented as the Debye oscillators, which contribute to the total specific heat as

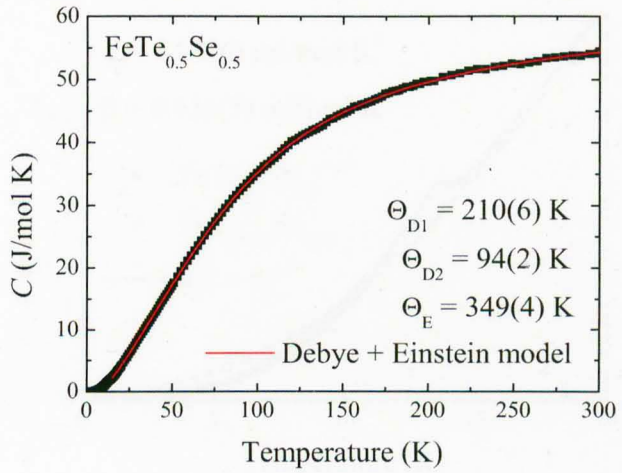

Figure 3.6: Temperature dependence of the specific heat, C of $FeTe_{0.5}Se_{0.5}$. Solid line is the two Debye and one Einstein model fit to the data using Eq. 3.3 and Eq. 3.4.

$$C_D(T,\Theta_D) = 9RN_D(T/\Theta_D)^3 \int_0^{\Theta_D/T} \frac{x^4 \exp(x)}{(\exp(x)-1)^2} dx, \tag{3.3}$$

while the optical modes are represented as

$$C_E(T,\Theta_E) = 3RN_E \left(\frac{\Theta_E}{T}\right)^2 \frac{\exp(\Theta_E/T)}{(\exp(\Theta_E/T)-1)^2}, \tag{3.4}$$

where R is the gas constant, Θ_D, Θ_E, N_D and N_D are the Debye temperature, the Einstein temperature, number of the Debye oscillators and number of the Einstein oscillators, respectively. For more details, see Ref. [81]. To get a satisfactory description of the phonon contribution, we model the temperature dependence of the specific heat data of $FeTe_{0.5}Se_{0.5}$ by two-Debye modes and one-Einstein mode, also called the Born-von Karman model

$$C(T) = \gamma_n T + 2C_D(T,\Theta_D) + C_E(T,\Theta_E), \tag{3.5}$$

where C_D and C_E denote the Debye and Einstein contributions to the specific heat and γ_n is the Sommerfeld coefficient. The fits yield $\Theta_{D1} = 210(6)$, $\Theta_{D2} = 94(2)$, $\Theta_E = 349(4)$ K for $FeTe_{0.5}Se_{0.5}$. These values are consistent with the other reported data for this system [82].

Figure 3.7 shows C vs. T of $FeTe_{0.5}Se_{0.5}$ and $FeTe_{0.75}Se_{0.25}$ at low temperature. Specific heat data of $FeTe_{0.5}Se_{0.5}$ exhibit a pronounced anomaly around 14 K.

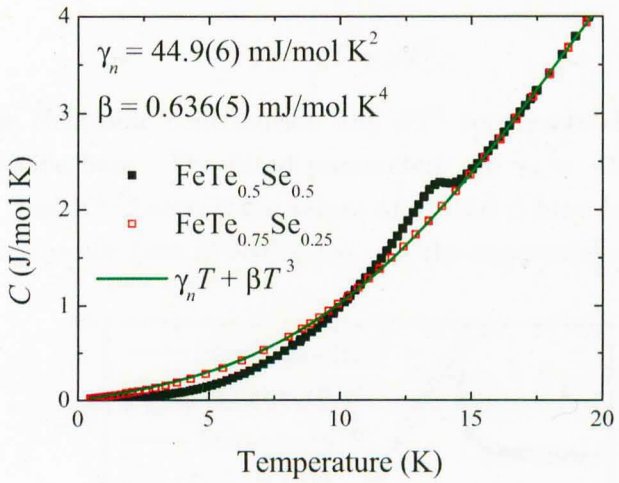

Figure 3.7: C vs T of $FeTe_{0.5}Se_{0.5}$ and $FeTe_{0.75}Se_{0.25}$ at low temperature. Solid lines are the fit to the specific data of $FeTe_{0.75}Se_{0.25}$ using Eq. 3.6.

When a material becomes superconducting, the lattice parameters (i.e. the crystal structure) will not change and so the specific heat of the lattice will not change either. The difference between the specific heat of the normal state and the superconducting state is thus due to the change in the electronic specific heat. When the lattice contribution to the specific heat is determined in the normal state (e.g. by applying a magnetic field) one can subtract this value from the total specific heat in order to find the contribution of the electronic specific heat in the superconducting state.

For $FeTe_{0.5}Se_{0.5}$, the upper critical field is too high to drive the superconductor into the normal state to estimate the phonon contribution. So as an alternative, we assume that the phonon part of the specific heat is almost independent of doping. We have therefore measured the specific heat of non-superconducting $FeTe_{0.75}Se_{0.25}$ to use as a reference for the phonon contribution to the specific heat for $FeTe_{0.5}Se_{0.5}$. The specific heat of $FeTe_{0.75}Se_{0.25}$ does not show any superconducting anomaly as expected. The temperature scale of the specific heat data of $FeTe_{0.75}Se_{0.25}$ has been corrected by a scaling factor (0.9) to match with the specific heat of $FeTe_{0.5}Se_{0.5}$ above T_c. The scaling factor was introduced as the phonon specific heats of both samples will not be strictly identical. These data further show that the substitution of Se by Te does increase the lattice contribution to the specific heat by a small amount as expected. The solid line in Fig. 3.7 shows the low temperature fit to the specific heat data of $FeTe_{0.75}Se_{0.25}$ using the equation

$$C(T) = \gamma_n T + \beta T^3, \tag{3.6}$$

where $\gamma_n T$ is the electronic contribution and βT^3 represents the phonon contribution to the specific heat. The fitted parameters are $\gamma_n = 44.9(6)$ mJ/mol K^2, $\beta = 0.636(5)$ mJ/mol K^4. Later, these values of γ_n and β have been used to calculate the electronic specific heat of $FeTe_{0.5}Se_{0.5}$ in the superconducting state.

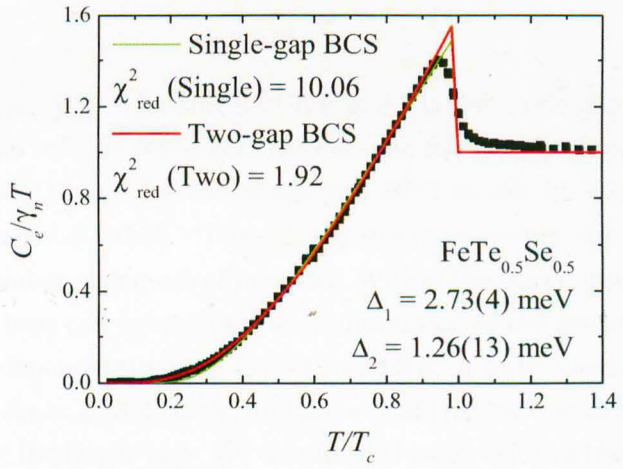

Figure 3.8: Electronic contribution to the specific heat of $FeTe_{0.5}Se_{0.5}$ as $C_e/\gamma_n T$ vs T/T_c. Solid lines are the fit to the data using a single-gap and two-gap BCS models.

We have investigated the symmetry of the superconducting gap of $FeTe_{0.5}Se_{0.5}$ by examining the temperature dependence of electronic specific heat. Figure 3.8 shows the non-lattice part of the specific heat of $FeTe_{0.5}Se_{0.5}$ obtained by subtracting the phonon contribution (βT^3) from the total specific heat data.

To perform a single-gap and two-gap BCS models fit to the $C_e/\gamma_n T$ data in the superconducting state, we use the BCS expressions for the normalized entropy, S, and the specific heat

$$\frac{S}{\gamma_n T_c} = -\frac{6}{\pi^2}\frac{\Delta_0}{k_B T_c}\int_0^\infty [f \ln f + (1-f)\ln(1-f)]dy, \tag{3.7}$$

$$\frac{C}{\gamma_n T_c} = t\frac{d(S/\gamma_n T_c)}{dt}, \tag{3.8}$$

where $t = T/T_c$, $f = [1 + \exp(E/k_B T)]^{-1}$ is the Fermi function, ϵ is the energy of the normal electrons relative to the Fermi energy, $E = [\epsilon^2 + \Delta^2(t)]^{1/2}$, and $y = \epsilon/\Delta$. The temperature dependence of the energy gap varies as $\Delta(t) = \Delta_0 \delta(t)$, where $\delta(t)$ is the

Table 3.2: Results for fits to the temperature dependence of the electronic contribution to the specific heat of $FeTe_{0.5}Se_{0.5}$ using different models for the symmetry of the superconducting gap function.

Model	Gap value (meV)	χ^2_{red}
s-wave	$\Delta(0) = 0.63(1)$	10.06
$s+s$-wave	Δ_1=2.73(4), Δ_2=1.26(13) and $\omega_1 = 0.87(5)$	1.92

normalized BCS gap [83]. The blue line in Fig. 3.8 is the single-gap BCS model fit to the data, while the red line represents the two-gap fit. We obtain a superconducting gap, $\Delta(0) = 0.63(1)$ meV for the single-gap BCS model fit with a reduced chi-squared (χ^2_{red}) value of 10.06. The χ^2_{red} statistic is simply the chi-squared (χ^2) divided by the number of degrees of freedom. Within the simple two-gap BCS model, the total specific heat can be assumed as a summation of the contribution from each gap calculated independently using Eqs. 3.7 and 3.8. A fit to the data using the two-gap model yields $\Delta_1 = 2.73(4)$ meV, and $\Delta_2 = 1.26(13)$ meV with a weighting factor (ω_1) of 0.87(5) for the larger gap. We obtain the lowest value of the χ^2_{red} (1.92) using this two-gap model. The magnitude of the superconducting gaps are $2\Delta_1/k_BT_c = 4.52(9)$ and $2\Delta_2/k_BT_c = 2.10(28)$. Table 3.2 shows the fitted parameters using different superconducting gap models. The second superconducting gap (smaller gap) is nearly half of the larger gap. These data suggest that the difference in the gap value of each band in this system is less substantial than the case of other multigap superconductors, like MgB_2 and $Lu_2Fe_3Si_5$ [28, 31] where the smaller gap is only one fourth of the larger gap.

3.3.5 μSR Measurements of $FeTe_{0.5}Se_{0.5}$

μSR measurements on $FeTe_{0.5}Se_{0.5}$ were performed using the MuSR spectrometer based at ISIS. For more details about the MuSR spectrometer, see section 2.4. Measurements were carried out in zero field and in both longitudinal-field (LF) and transverse-field (TF) modes in magnetic fields of up to 2500 and 600 Oe for the LF and TF modes, respectively. Each detector is normalized for the muon decay and rotated into two components at 90 degrees to one another.

A powder sample of $FeTe_{0.5}Se_{0.5}$ (with a size of 30 mm by 30 mm square and 1 mm thick) was mixed with GE varnish and mounted on a pure Ag plate. For measurements down to 1.2 K, the sample was placed in a conventional Oxford Instruments cryostat. Data were also collected between 0.3 and 1 K in an Oxford

Instruments He-3 cryostat. For the measurements in TF mode in the conventional cryostat, haematite slabs were positioned immediately behind the sample to reduce the background signal. Muons stopping in the hematite contribute a negligible amount to the asymmetry signal because they are rapidly depolarized. For measurements in the He-3 cryostat these haematite slabs were removed to ensure good thermal contact between the sample and the cold stage of the cryostat leading to an increased background in the collected data. For all the data collected in a magnetic field presented here, the sample was field-cooled to base temperature and the data collected while warming the sample in a field. A set of data collected at 1.2 K in an applied LF, $H = 400$ Oe after the sample was zero-field cooled produced no usable signal due to the very strong pinning present in the sample.

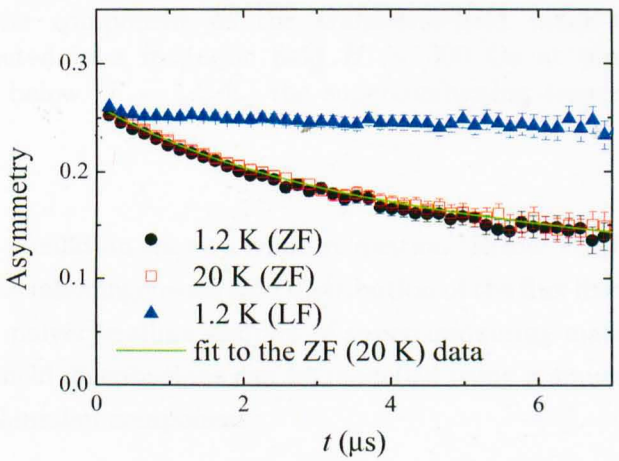

Figure 3.9: Zero-field (T=20 and 1.2 K) and longitudinal-field (T=20 K and $H = 300$ Oe) μSR time spectra for a sample of $FeTe_{0.5}Se_{0.5}$.

Zero-field (ZF) μSR data (see Fig. 3.9) can be fitted using

$$G_Z(t) = A_0 \exp(-\Lambda t), \tag{3.9}$$

where A_0 is the initial asymmetry, with a small nearly T independent relaxation rate, Λ, of $0.19\mu s^{-1}$ between 20 and 1.2 K. The application of a small longitudinal magnetic field is sufficient to decouple the muon spin from the internal magnetic field. In line with the observations of Khasanov *et al.* [76] this suggests that the depolarization is caused by weak, static magnetic fields, that are present in the sample both above and below T_c. The most likely source of these fields is dilute, randomly oriented magnetic moments associated with the Fe_3O_4 impurity phase.

Figure 3.10 shows the TF-μSR precession signals above and below T_c. In the

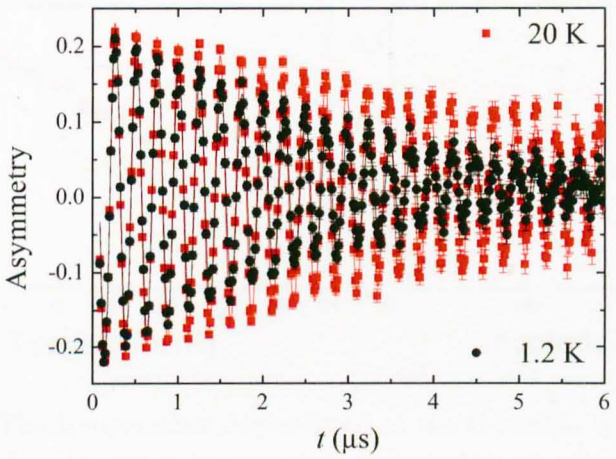

Figure 3.10: One component of the transverse-field muon-time spectra for $FeTe_{0.5}Se_{0.5}$ collected in a magnetic field $H = 300$ Oe at temperatures above ($T = 20$ K) and below ($T = 1.2$ K) the superconducting transition temperature $T_c = 14.4$ K.

normal state, the oscillation shows a small relaxation. Below T_c, the relaxation rate increases due to the inhomogeneous field distribution of the flux line lattice. Previous measurements on polycrystalline samples of superconducting materials have shown that the internal field distributions can be modelled using a sinusoidally oscillating function with a Gaussian component

$$G_X(t) = A_0 \exp(-\Lambda t) \exp\left(-\sigma^2 t^2\right) \cos(\omega t + \varphi), \tag{3.10}$$

where ω is the muon precession frequency and φ is the phase offset. σ is the Gaussian relaxation rate given by $\sigma = \left(\sigma_{sc}^2 + \sigma_{nm}^2\right)^{\frac{1}{2}}$. $\sigma_{sc}(T)$ is the contribution to the relaxation arising from the vortex lattice while σ_{nm}, the nuclear magnetic dipolar term, is assumed to be temperature independent over the temperature range of the measurements. The data were fitted in two steps. First the data in the two channels were fitted simultaneously at each temperature with A_0, Λ, and σ as common variables. The fits were checked over the entire temperature range to ensure that physical values were obtained for all the parameters at each temperature point. To ensure stability of the fits, Λ was then fixed to the value obtained just above T_c and the data were refitted at each temperature point. The temperature dependence of σ obtained is shown in Fig. 3.11 (a). The value of σ is also observed as a function of applied field and found to very little or no change over the entire field range [see Fig. 3.11 (b)].

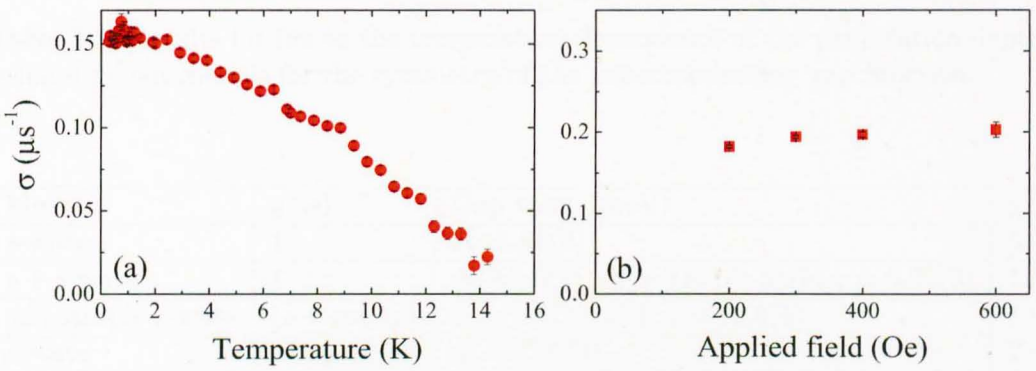

Figure 3.11: (a) The temperature dependence of the Gaussian depolarization rate σ extracted from the TF muon-time spectra collected in an applied magnetic field $H = 300$ Oe. (b) The magnetic field independence of the parameter σ.

In a superconductor with a large upper critical field and a hexagonal Abrikosov vortex lattice, the Gaussian muon-spin depolarization rate, $\sigma_{sc}(T)$, is related to the penetration depth λ by the expression

$$\frac{2\sigma_{sc}^2(T)}{\gamma_\mu^2} = 0.00371\frac{\Phi_0^2}{\lambda^4(T)}, \tag{3.11}$$

where $\gamma_\mu/2\pi = 135.5$ MHz/T is the muon gyromagnetic ratio and $\Phi_0 = 2.068 \times 10^{-15}$ Wb is the flux quantum [47, 84]. The temperature dependence of the penetration depth can then be fitted using either a single gap or a two gap model [23, 85]

$$\frac{\lambda^{-2}(T)}{\lambda^{-2}(0)} = \omega_1\frac{\lambda^{-2}(T,\Delta_{0,1})}{\lambda^{-2}(0,\Delta_{0,1})} + (1-\omega_1)\frac{\lambda^{-2}(T,\Delta_{0,2})}{\lambda^{-2}(0,\Delta_{0,2})}, \tag{3.12}$$

where $\lambda^{-2}(0)$ is the value of the penetration depth at $T = 0$ K, $\Delta_{0,i}$ is the value of the i-th ($i = 1$ or 2) superconducting gap at $T = 0$ K and ω_1 is the weighting factor.

Each term in equation 3.12 is evaluated using the standard expression within the local London approximation [22, 86]

$$\frac{\lambda^{-2}(T,\Delta_{0,i})}{\lambda^{-2}(0,\Delta_{0,i})} = 1 + \frac{1}{\pi}\int_0^{2\pi}\int_{\Delta_{(T,\varphi)}}^{\infty}\left(\frac{\partial f}{\partial E}\right)\frac{E\mathrm{d}E\mathrm{d}\varphi}{\sqrt{E^2-\Delta_i(T,\varphi)^2}}, \tag{3.13}$$

where f is the Fermi function, φ is the angle along the Fermi surface, and $\Delta_i(T,\varphi) = \Delta_{0,i}\delta(T/T_c)\,g(\varphi)$. The temperature dependence of the gap is approximated by the expression $\delta(T/T_c) = \tanh\left\{1.82\left[1.018\left(T_c/T-1\right)\right]^{0.51}\right\}$ [23] while

Table 3.3: Results for fits to the temperature dependence of the penetration depth using different models for the symmetry of the superconducting gap function.

Model	$g(\varphi)$	Gap value (meV)	χ^2_{red}
s-wave	1	Δ=1.86(2)	5.93
$s+s$-wave	1	Δ_1=2.6(1), Δ_2=0.87(6) and $\omega_1 = 0.70(3)$	1.55
anisotropic s-wave	$(s+\cos 4\varphi)$	$\Delta = 1.4(1)$ with $s = 1.56(5)$	1.62
d-wave	$\lvert\cos(2\varphi)\rvert$	$\Delta = 3.31(4)$	2.87

$g(\varphi)$ describes the angular dependence of the gap and is replaced by 1 for both an s-wave and an $s+s$-wave gap, $(s+\cos 4\varphi)$ for an anisotropic s-wave and $|\cos(2\varphi)|$ for a d-wave gap. [63]. The fits [see Table 3.3] appear to rule out both the d-wave and s-wave as possible models for this system. The values of χ^2 are lower for both $s+s$-wave and anisotropic s-wave models. Note, the normalized χ^2 values, resulting from our least squares fits to the temperature dependence of λ^{-2} using different models for the gap, are used as the criteria to determine which model best describes the data.

The anisotropic s-wave model gives a value for s, the parameter reflecting the isotropic s-wave component, that is larger than that obtained for $FeSe_{0.85}$ in Ref. [76]. Nevertheless, the variation in the gap with angle $\Delta_{max}/\Delta_{min} \approx 4.6$ is still larger than the published values for related single layer superconductor $NdFeAsO_{0.9}F_{0.1}$. [87]

A fit to the data using a two-gap $s+s$-wave model is shown in Fig. 3.12 and gives $\Delta_{0,1} = 2.6(1)$ meV and $\Delta_{0,2} = 0.87(6)$ meV with $\omega_1 = 0.70(3)$. This model gives the lowest χ^2. The gap parameters extracted from these μSR studies, are consistent with the parameters extracted from heat capacity measurements. ω_1 agrees with the value obtained by μSR for $FeSe_{0.85}$ where $\omega_1 = 0.658(3)$. [76] The size of the larger energy gap for $FeSe_{0.85}$ and $FeTe_{0.5}Se_{0.5}$ scale with T_c. We found the gap ratio, $\Delta_{0,1}/\Delta_{0,2} \sim 3$ for $FeTe_{0.5}Se_{0.5}$, which is 40% smaller than the corresponding value seen in $FeSe_{0.85}$ but is similar to the value for RFeAsO$_{0.9}$F$_{0.1}$ (R=La, Nd) determined by measuring the magnetic penetration depth using a tunnel-diode resonator [88].

For anisotropic polycrystalline samples, the magnetic penetration depth, λ, calculated from the μSR depolarization rate σ is related to λ_{ab}, the in-plane penetration depth by $\lambda = 3^{\frac{1}{4}}\lambda_{ab}$ [89]. Note, μSR cannot measure λ along a single crystallo-

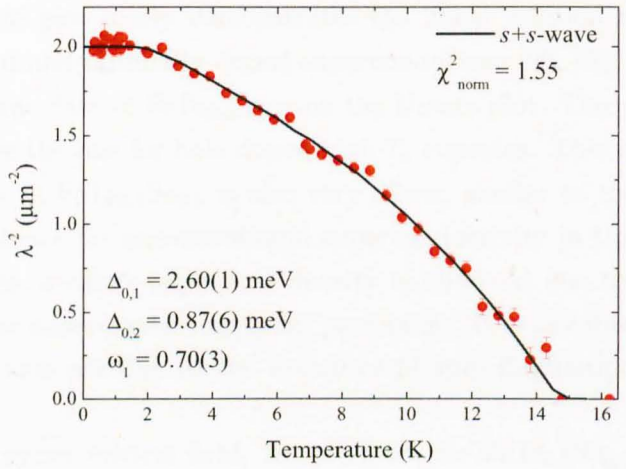

Figure 3.12: Temperature dependence of λ^{-2} for $FeTe_{0.5}Se_{0.5}$. The curve (black line) is a fit to the data using two s-wave components, each with an isotropic gap.

graphic direction. The measurements are limited to mixed quantities, which here is $\lambda_{ab} = (\lambda_a \lambda_b)^{1/2}$. At $T = 0$, the value for $\lambda\,(0) = 703(2)$ nm with $\lambda_{ab}\,(0) = 534(2)$ nm. The error in $\lambda(0)$ is the statistical error arising from the fit to the $\lambda^{-2}(T)$ data using the model described in the text. The error quoted does not take into account any systematic errors (e.g. vortex lattice disorder) that may be present in the data. These values are longer than those obtained by Khasanov *et al.* [76] for $FeSe_{0.85}$ in spite of the fact that the T_c of $FeTe_{0.5}Se_{0.5}$ is ~ 6 K higher.

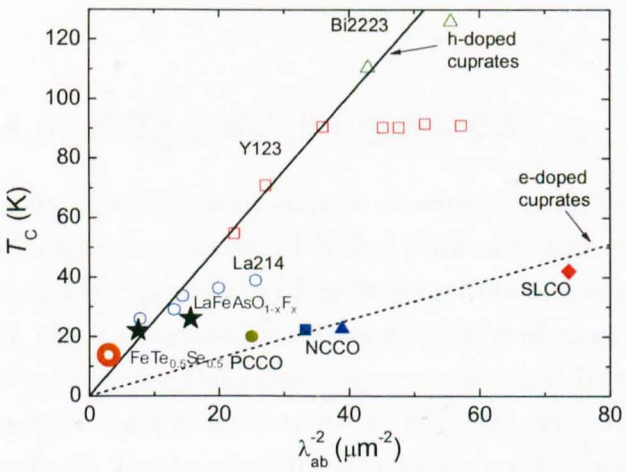

Figure 3.13: Uemura plot for hole and electron doped high T_c cuprates. The doughnut on the plot shows the data for $FeTe_{0.5}Se_{0.5}$.

An Uemura plot nicely demonstrates the linear relation between λ^{-2} and T_c for underdoped and optimally doped superconductors [90, 91]. In Fig. 3.13, the doughnut shows the data of $FeTe_{0.5}Se_{0.5}$ on the Umera plot. The value for λ places $FeTe_{0.5}Se_{0.5}$ above the line for hole doped high T_c cuprates. This indicates that the superfluid density of $FeTe_{0.5}Se_{0.5}$ is also very dilute, similar to the cuprate family, and provides evidence for unconventional superconductivity in this system. In underdoped cuprates, a dilute superfluid density is observed due to the fluctuations of the phase of the superconducting order parameter. It is assumed that the effects of phase fluctuations are due to the exchange of spin fluctuations in the pairing interaction [92].

Using an upper critical field, $B_{c2}(0) \parallel ab$, for $FeTe_{0.5}Se_{0.5}$ estimated from transport measurements of 520 kOe and $B_{c2} = \frac{\Phi_0}{2\pi\xi^2}$, we calculate a coherence length, ξ_{ab}, for $FeTe_{0.5}Se_{0.5}$ at 0 K of $\sim$ 2.6 nm. If this is combined with our measurement of λ and the standard expression $H_{c1} = \frac{\Phi_0}{4\pi\lambda^2}\left(\ln\frac{\lambda}{\xi} + 0.12\right)$ [22] we estimate $H_{c1}(0) \parallel ab$ = 32 Oe. This is in fair agreement with magnetization measurements where the first deviation from linear behaviour gives $H_{c1}//ab$ of between 10 and 80 Oe at 1.5 K. [66, 67]

By this point we know that $FeTe_{0.5}Se_{0.5}$ is superconducting with a T_c of 14.5 K. We have also seen that the T_c of $FeTe_{0.5}Se_{0.5}$ can be raised as high as 23.3 K with the application of external pressure. Inseatd of applying external pressure, we can substiture a atomic site of a material with a smaller size atom and increase the internal pressure (called chemical pressure). In the next section we have discussed about $FeTe_{1-x}S_x$, where we replaced Se with S to increase the T_c by growing chemical pressure.

3.4 Studies of $FeTe_{1-x}S_x$ $(0.1 \leq x \leq 0.5)$

FeTe has a tetragonal structure analogous to superconducting FeSe. It undergoes antiferromagnetic ordering at nearly 70 K and does not show superconductivity. The magnetic ordering is suppressed by S or Se substitution, and superconductivity appears [62, 63, 69, 74]. It is assumed that the substitution of smaller atoms at the Te site create a chemical pressure and induce superconductivity. However, hydrostatic pressure does not induce superconductivity in FeTe [93, 94]. In order to try to understand why only the Te-site substitution can induce superconductivity in FeTe, we have carried out an in depth study of S-substituted FeTe.

3.4.1 Sample Growth of $FeTe_{1-x}S_x$ $(0.1 \leq x \leq 0.5)$

As-grown samples of $FeTe_{1-x}S_x$ $(0.1 \leq x \leq 0.5)$ were made using the same technique as described in section 3.3.1. Finally, the samples were annealed in an oxygen flow at 200°C for 12 h.

3.4.2 Powder X-ray Diffraction Studies of $FeTe_{1-x}S_x$ $(0.1 \leq x \leq 0.5)$

Powder x-ray diffraction patterns were collected using a Panalytical X'Pert Pro X-Ray MPD Powder Diffractometer with Cu $K\alpha$ radiation. For more details of the experimental procedure, see section 2.2.1. The XRD patterns show that all the samples have a tetragonal structure with space group $P4/nmm$. The patterns indicate that all the samples contain small amounts of the impurities Fe_7S_8 and Fe_3O_4, consistent with previously reported XRD patterns.[71] By comparing the intensity of the impurity peaks with those from the sample, we estimate that the impurities constitute no more then 2% of the sample.

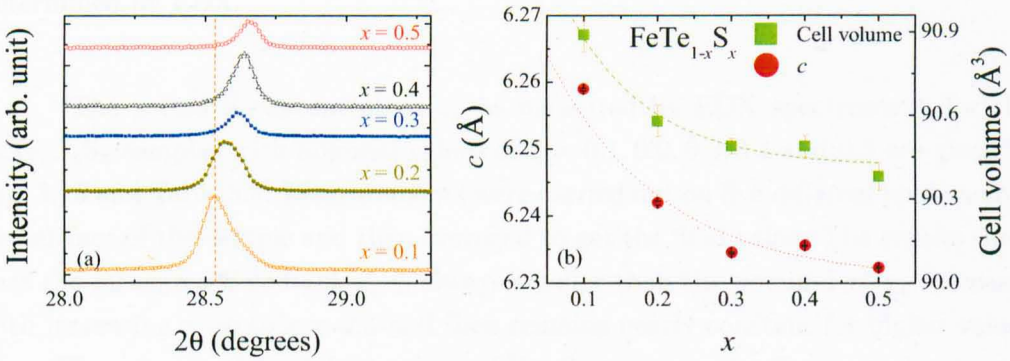

Figure 3.14: (a) Powder x-ray diffraction data collected around the (002) peak for samples of $FeTe_{1-x}S_x$ $0.1 \leq x \leq 0.5$ shows the clear shift in the position of this peak with increasing x. (b) The c-axis lattice parameter and the cell volume as a function of S doping, refined from the x-ray diffraction patterns.

Figure 3.14(a) clearly shows the shifting of the (002) peak toward higher 2θ angles with increasing S concentration. A broadening of the peaks for lower x (especially for $x = 0.1$ and $x = 0.2$) indicates the presence of some local structural inhomogeneity in these samples. Figure 3.14(b) shows that the lattice constant, c, and the cell volume initially decrease with increasing S concentration. These results are consistent with the fact that the ionic radius of S^{2-} (1.84 Å) is smaller than Te^{2-} (2.21 Å). [95] The changes in c and the cell volume reach saturation at $x = 0.3$,

implying that there is a limit to the amount of S that can be doped onto the Te site in $FeTe_{1-x}S_x$.

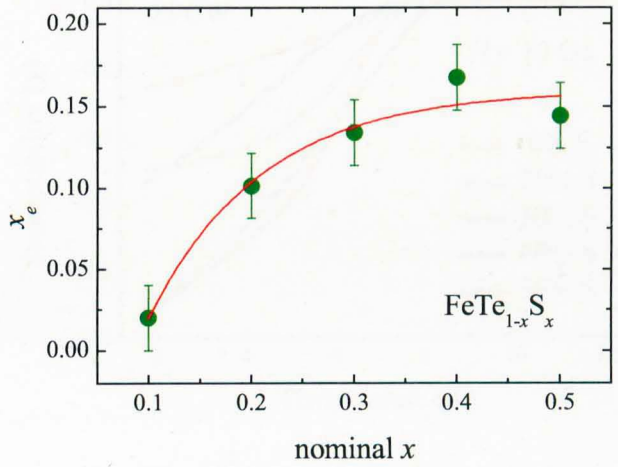

Figure 3.15: Actual S concentration, x_e, in $FeTe_{1-x}S_x$ as a function of nominal x determined by EDX.

The actual S concentration x_e as measured by EDX spectroscopy for the $FeTe_{1-x}S_x$ samples with nominal values of $x = 0.1, 0.2, 0.3, 0.4$ and 0.5 are given in Fig. 3.15 and Table 3.4. Measurements were carried out on five different spots across the surface of the sample and then averaged to get the final value. The results show that the measured S content x_e is always smaller than the nominal x. x_e increases with increasing x up to $x = 0.3$ and then remains nearly constant for higher values of x. We estimate the solubility limit of the S atoms on the Te site to be around 16%, which is slightly higher than 12%, suggested by Mizuguchi *et al.* [74]. However we could not detect any trace of free S in the XRD data.

Table 3.4: Results for S concentration(x_e), lattice parameters (a and c) and cell volume (v) of $FeTe_{1-x}S_x$ for nominal $x = 0.1, 0.2, 0.3, 0.4$ and 0.5.

x	x_e	a(Å)	c(Å)	v(Å^3)
0.1	0.02(1)	3.811(3)	6.2589(2)	90.89(6)
0.2	0.10(2)	3.810(1)	6.2419(3)	90.58(6)
0.3	0.13(5)	3.810(1)	6.2345(1)	90.49(3)
0.4	0.16(4)	3.810(2)	6.2356(1)	90.49(4)
0.5	0.14(5)	3.808(2)	6.2323(1)	90.38(5)

3.4.3 Magnetization Measurements of $FeTe_{1-x}S_x$ $(0.1 \leq x \leq 0.5)$

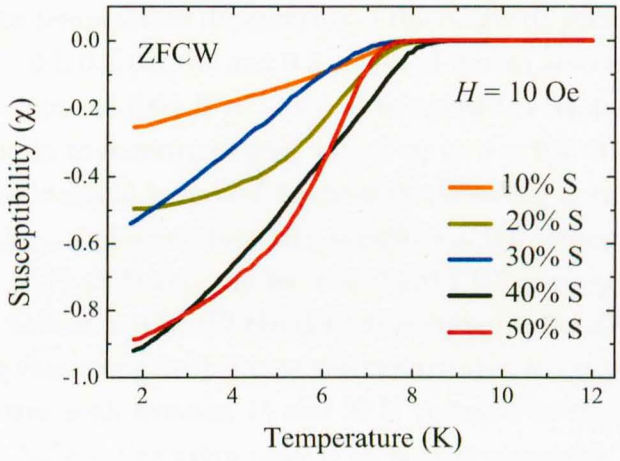

Figure 3.16: Temperature dependence of the magnetic susceptibility, $\chi(T)$, of $FeTe_{1-x}S_x$ for $x = 0.1, 0.2, 0.3, 0.4$ and 0.5, measured on zero-field-cooled warming (ZFCW).

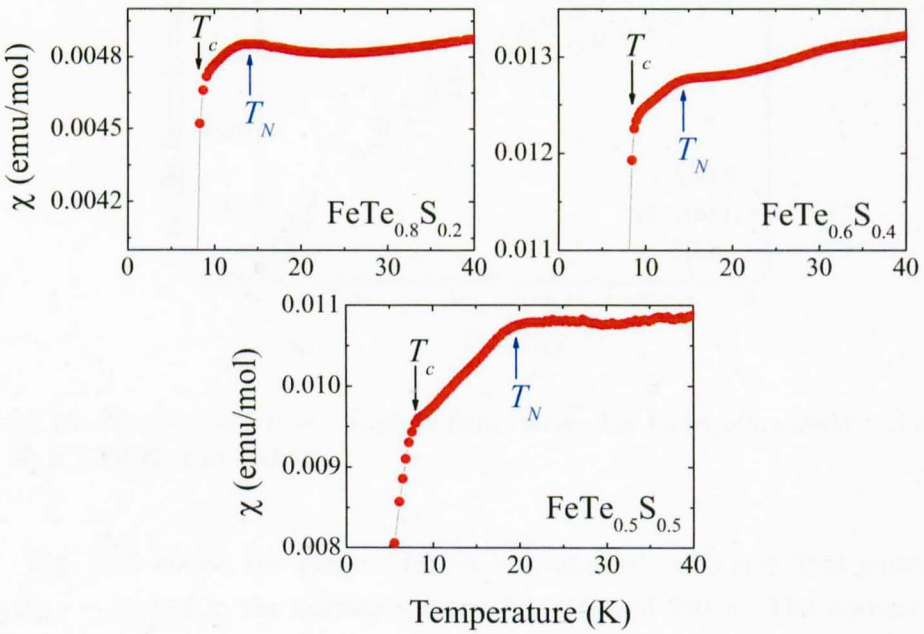

Figure 3.17: Temperature dependence of the magnetic susceptibility, $\chi(T)$, of $FeTe_{1-x}S_x$ for $x = 0.2, 0.4$ and 0.5, measured on zero-field-cooled warming (ZFCW) with an applied field of 1 kOe.

Magnetization measurements as a function of temperature T, applied field H and pressure P were performed in a MPMS magnetometer [see section 2.3.1]. Fig. 3.16 shows the temperature dependence of the magnetic susceptibility $\chi(T)$ of $FeTe_{1-x}S_x$ for $x = 0.1, 0.2, 0.3, 0.4$ and 0.5 collected during zero-field-cooled warming (ZFCW) in an applied field $H = 10$ Oe. The transition temperature T_c (onset) of $FeTe_{1-x}S_x$ appears to increase slightly with x up to $x = 0.4$. The data also show that the diamagnetic signal increases slowly with increasing x and reaches a maximum for $FeTe_{0.6}S_{0.4}$, indicating that this sample has the largest superconducting volume fraction. $\chi(T)$ of $FeTe_{1-x}S_x$ for $x = 0.2, 0.4, 0.5$ were also collected in an applied magnetic field of 1 kOe. All the data were taken in the ZFCW mode. Data in Fig. 3.17 show that along with the superconducting transition (marked as T_c), there is also an extra peak between 14 and 20 K (marked as T_N) for each of those compositions. We believe this extra peak is an antiferromagnetic transition due to the ordering of the iron spins. A similar antiferromagnetic transition has also been observed at 58 K in the parent compound FeTe [96].

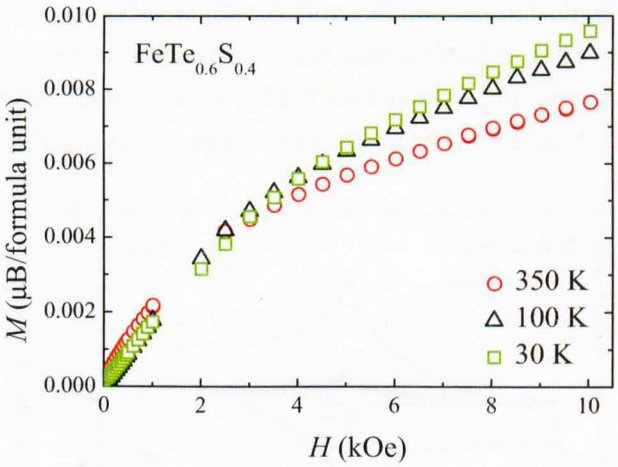

Figure 3.18: Magnetization vs. applied field curves for $FeTe_{0.6}S_{0.4}$ collected above T_c at 30 K, 100 K, and 350 K.

Fig. 3.18 shows the magnetization vs. applied magnetic field curves for $FeTe_{0.6}S_{0.4}$ collected in the normal state at 30, 100 and 350 K. The normal state signals are nearly temperature independent. This suggests that the normal state magnetization has a response made up of contributions typical of a soft ferromagnet and a Pauli paramagnet [67]. This is due to the presence of a small amount of Fe_7S_8 and Fe_3O_4 in the sample. Using the reported value for the saturation magnetization of Fe_7S_8 and Fe_3O_4 we estimate this fraction to be $\sim 1.0\%$ of the sample by mass,

is similar to our x-ray diffraction measurements [97, 75].

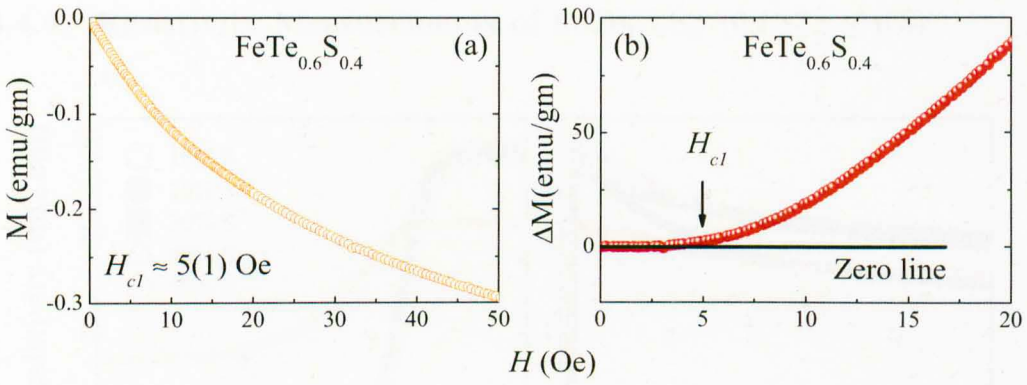

Figure 3.19: (a) Magnetization (M) as a function of applied magnetic field, H, collected at 1.8 K. (b) ΔM vs H, shows the deviation from the straight line magnetization.

Fig. 3.19 (a) shows the magnetization (M) as a function of applied magnetic field at 1.8 K. ΔM is the difference in the magnetization from a straight line behaviour where the first deviation of ΔM from the zero line gives an estimate of the lower critical field (H_{c1}). H_{c1} is approximately 5(1) Oe for $\Delta M \leq 10^{-5}$ emu/f.u.

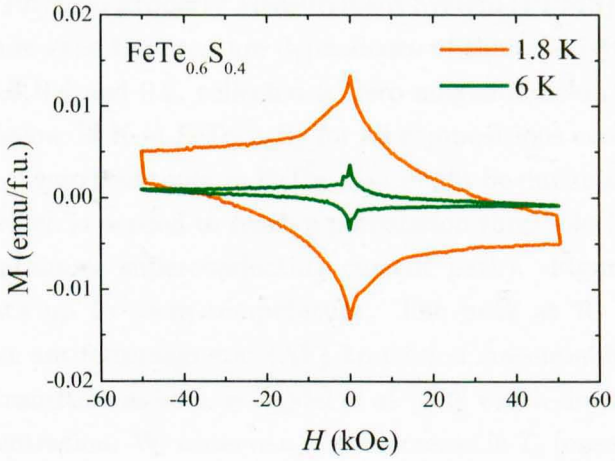

Figure 3.20: Magnetic hysteresis loops for $FeTe_{0.6}S_{0.4}$ collected at 1.8 K and 6 K.

Figure 3.20 presents the magnetic hysteresis loops for $FeTe_{0.6}S_{0.4}$, collected at 1.8 K and 6 K. The hysteresis loops have a large loop-width that mainly arises from bulk flux pinning rather than from the (Bean-Livingston) surface barrier [98]

as seen in many other Fe-based superconductors [99].

3.4.4 Resistivity Measurements of $FeTe_{1-x}S_x$ $(0.1 \leq x \leq 0.5)$

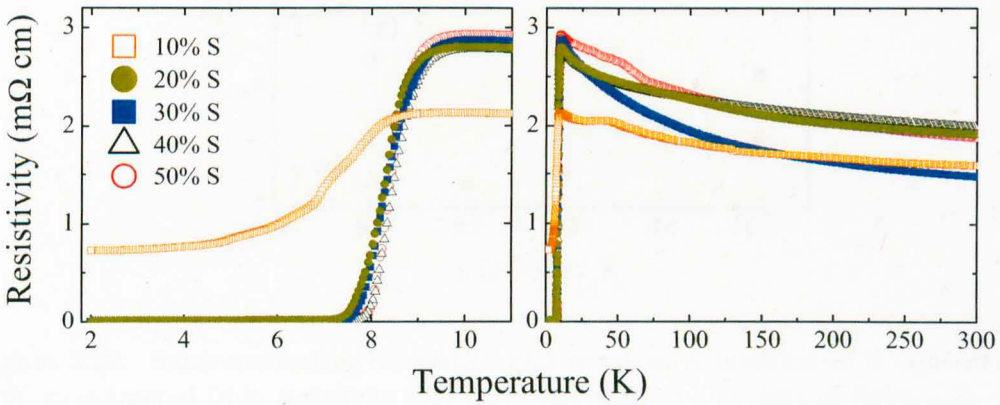

Figure 3.21: (a) Resistivity as a function of temperature of $FeTe_{1-x}S_x$ for $x = 0.1, 0.2, 0.3, 0.4$ and 0.5, measured in zero applied magnetic field. (b) Resistivity as a function of temperature, measured up to room temperature.

AC resistivity was measured by a standard four-probe configuration using a *Quantum Design* Physical Property Measurement System (PPMS), see section 2.3.2. Figure 3.21 (a) shows the temperature dependence of the resistivity ρ of $FeTe_{1-x}S_x$ for $x = 0.1, 0.2, 0.3, 0.4$ and 0.5, collected in zero magnetic field. Zero resistivity is clearly observed below 10 K in $FeTe_{1-x}S_x$ for all compositions except in the $x = 0.1$ sample. The lack of zero resistivity in $FeTe_{0.9}S_{0.1}$ might be due to the insufficiency of S concentration which is needed to reach a percolation threshold (i.e. the minimum fraction for a continuous superconducting current path). Figure 3.21 (b) shows the resistivity data up to room temperature. The peak at 70 K for $FeTe_{0.9}S_{0.1}$ corresponds to an antiferromagnetic (AF) transition presumably coupled with a structural phase transition as seen by Zajdel *et al.* [100] which slowly disappears with increasing S concentration. We observe a slight increase in T_c (onset) with increasing S concentration with a maximum T_c (onset) of (10.04 ± 0.01) K for $x = 0.4$.

The superconducting transition temperature of $FeTe_{1-x}S_x$ as a function of S doping is shown in Fig. 3.22. T_c^{onset} (R) and T_c^{zero} (R) have been taken from the resistivity data [see Fig. 3.21] while T_c^{onset} (χ) is taken from the $\chi(T)$ data [see Fig. 3.16]. In all three sets of data, T_c remains nearly constant for all sulfur compositions.

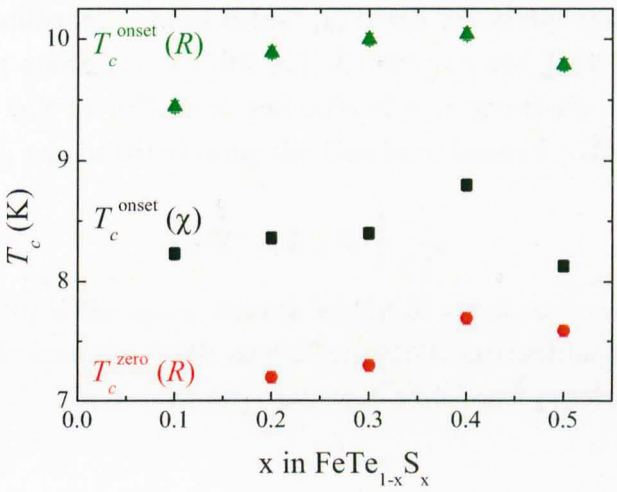

Figure 3.22: Superconducting T_c (onset and zero) as a function of S concentration, x, extracted from resistivity (R) and susceptibility (χ) data of $FeTe_{1-x}S_x$ for $x = 0.1, 0.2, 0.3, 0.4$ and 0.5.

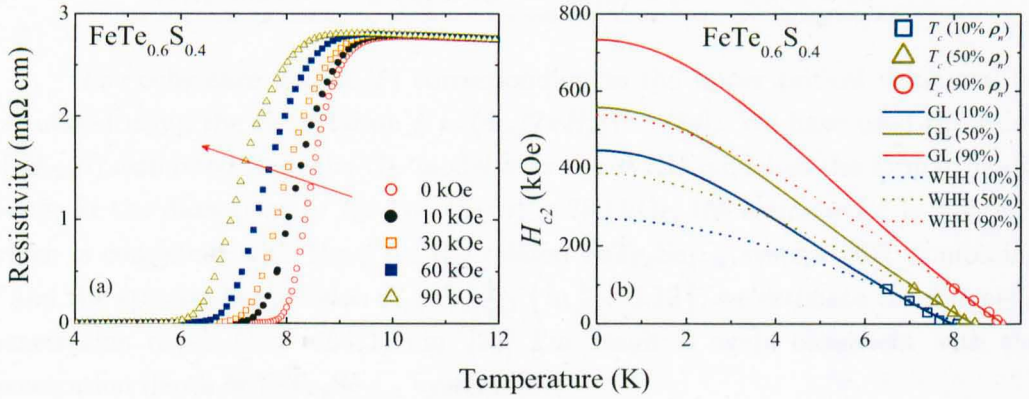

Figure 3.23: (a) Resistivity as a function of temperature of $FeTe_{0.6}S_{0.4}$, measured in different applied fields. (b) Temperature dependence of the upper critical field of $FeTe_{0.6}S_{0.4}$. The solid lines indicate the fits made using GL theory. The dashed lines indicate the fits from the WHH model.

Fig. 3.23 (a) shows the temperature dependence of resistivity of $FeTe_{0.6}S_{0.4}$ in different applied magnetic fields up to 90 kOe. This indicates that the superconducting transitions shift toward lower temperature and become broader with increasing applied magnetic fields. ΔT_c increases from 2.14 K at 0 Oe to 3.10 K at 90 kOe. Fig. 3.23 (b) shows the upper critical field (H_{c2}), determined from the T_c

of $FeTe_{0.6}S_{0.4}$ at different applied fields. ρ_n is the resistivity of $FeTe_{0.6}S_{0.4}$ in the normal state (just above T_c). $T_c(10\%\ \rho_n)$, $T_c(50\%\ \rho_n)$ and $T_c(90\%\ \rho_n)$ are defined as the resistivity falls to 10%, 50% and 90% of ρ_n respectively. The temperature dependence of H_{c2} can be fitted using the Ginzburg Landau (GL) theory:

$$H_{c2}(T) = H_{c2}(0)\frac{1-t^2}{1+t^2}, \tag{3.14}$$

where $H_{c2}(0)$ is the upper critical field at $T = 0$ K and $t = T/T_c$ [101]. The fits were also made from the WHH model [for details, see section 3.3.3]. Results are shown in Table. 3.5. The results are consistent with other reported values for this system. [69, 102]

Table 3.5: Results for fits to the temperature dependence of the upper critical field of $FeTe_{0.6}S_{0.4}$ using GL theory and WHH model.

Model	$H_{c2}(10\%)$ (kOe)	$H_{c2}(50\%)$ (kOe)	$H_{c2}(90\%)$ (kOe)
GL theory	$45(3) \times 10$	$56(3) \times 10$	$73(5) \times 10$
WHH Model	$27(4) \times 10$	$39(3) \times 10$	$54(4) \times 10$

The coherence length (ξ) corresponding to the upper critical value can be calculated using the GL relation $\xi = (\Phi_o/2\pi H_{c2})^{1/2}$ [84]. We have used the value of $H_{c2}(0)$ estimated from the GL model over the WHH model as the formar model better fit the data close to T_c. For $H_{c2}(0) = 780$ kOe, the estimated ξ is 2.05 nm, which is consistent with the ξ for the related $FeTe_xSe_{1-x}$ system. [67] Combining ξ and the standard expression $H_{c1} = \frac{\Phi_0}{4\pi\lambda^2}\left(\ln\frac{\lambda}{\xi} + 0.12\right)$, we estimate the magnetic penetration depth, $\lambda = 664(1)$ nm. [22] The result is again consistent with the penetration depth of $FeTe_xSe_{1-x}$ system. [67]

3.4.5 Magnetization Measurements of $FeTe_{0.5}S_{0.5}$ with Pressure

Magnetization versus temperature under pressure were carried out in a copper-beryllium clamp cell (easyLab Mcell 10). For details about the easyLab Mcell 10, see section 2.3.1. The samples were placed in a PTFE sample holder filled with a pressure transmitting medium (Daphne oil) and the pressure was applied at room temperature. The pressure at low temperature was determined by measuring the T_c of a piece of high purity (99.9999%) tin (used as a Manometer) placed alongside the sample.

Fig. 3.24 shows the pressure dependence of the T_c of $FeTe_{0.5}S_{0.5}$ obtained from magnetization measurements. Data collected for increasing or decreasing pres-

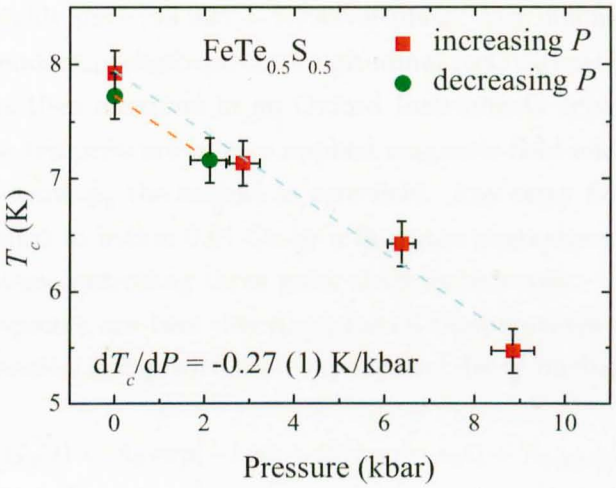

Figure 3.24: Pressure (P) dependence of the transition temperature T_c for $FeTe_{0.5}S_{0.5}$.

sure legs, T_c of $FeTe_{0.5}S_{0.5}$ decreases linearly with increasing pressure (P) with a gradient, $dT_c/dP = -0.27(1)$ K/kbar. This contrasts with the scenario it has been observed for FeSe and $FeTe_{1-x}Se_x$ system, where T_c initially increases with P and goes through a broad maximum and decreases thereafter [64]. This type of opposite pressure dependence can be understood from the low temperature crystal symmetry of $FeTe_{1-x}S_x$ system. A detail study by P. Zajdel *et al.* [100] on $FeTe_{1-x}S_x$ suggest that on sulfur inclusion, the monoclinic crystal structure of $Fe_{1+x}Te$ transforms through an orthorhombic phase to a superconducting tetragonal phase with a T_c of 10 K. This is a completely different scenario to that seen for other members of the iron chalcogenide system. For example, FeSe is orthorhombic rather than tetragonal at low temperature [103]. Hence, a possible link can be made between the structure and pressure dependence of T_c in the iron chalcogenide system.

So far we have investigated different superconducting properties of $FeTe_{1-x}S_x$. To observe the magnetic ordering and if there is any coexistence between the superconducting and magnetic phase in $FeTe_{1-x}S_x$, we have performed the μSR studies on the different compositions of $FeTe_{1-x}S_x$.

3.4.6 μSR Measurements of $FeTe_{1-x}S_x$ $(0.1 \leq x \leq 0.5)$

μSR experiments were carried out in longitudinal geometry using the MuSR spectrometer at the ISIS facility (see section 2.4 for more detail). The polycrystalline samples were formed into thin disks, 30 mm in diameter and 1 mm thick, and

mounted onto a highly pure (99.995 + %) silver plate. Any muons stopped in silver give a time-independent background for longitudinal (relaxation) experiments. The sample holder was then mounted in an Oxford Instruments cryostat. The sample was cooled to base temperature in zero applied magnetic field and the μSR spectra were collected on warming the sample in zero field. Any stray fields at the sample position are cancelled to within 0.01 Oe by a flux-gate magnetometer and an active compensation system controlling three pairs of correction coils.

The μSR spectra are best described for all temperatures and compositions by a double exponential decay with each exponential decay having equal weighting, as given by

$$G_z(t) = A_0 \exp(-\lambda_1 t) + A_0 \exp(-\lambda_2 t) + A_{bckgrd} \tag{3.15}$$

where A_0 is the initial asymmetry, $\lambda_{1,2}$ are the muon depolarization rates and A_{bckgrd} is the background coming from Ag exposed to the muon beam. A typical spectrum is shown in Fig. 3.25. The need for the two exponential decay times implies that there are two unique muon sites within the sample.

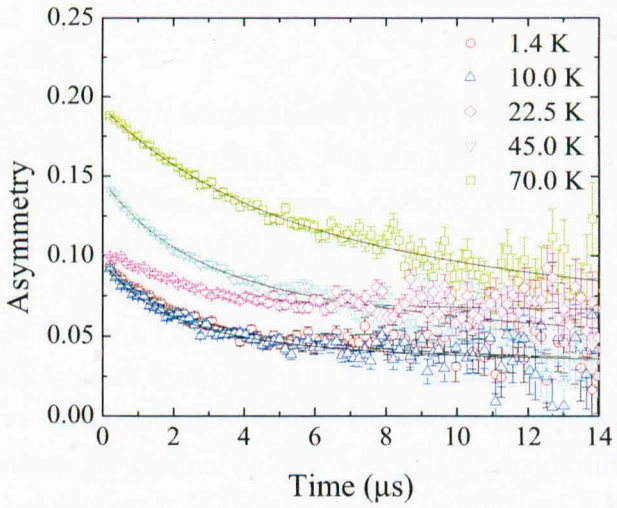

Figure 3.25: Typical μSR spectra for $FeTe_{0.9}S_{0.1}$ for a range of temperatures. The lines are least squares fits to the data as described in the text.

Figure 3.26 shows the initial asymmetry as the function of temperature. The drop in the initial asymmetry might be due to a magnetic transition which does not show any dependence on composition. Interestingly, the drop in initial asymmetry is quite broad which suggests regions of the sample are ordering, which may indicate inhomogeneity in the sample. Another interesting point to note is the

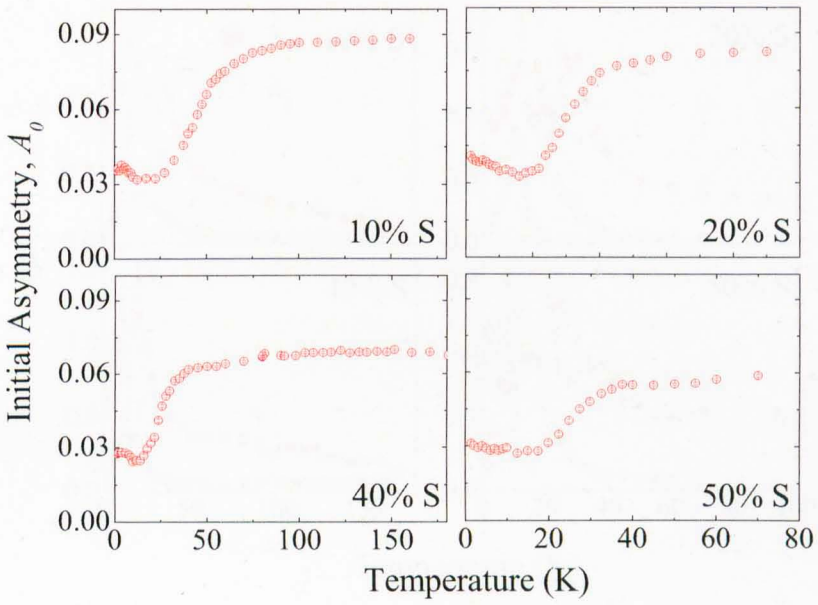

Figure 3.26: The temperature dependence of the initial asymmetry of the relaxing component A_0.

gradual reduction of A_0 at high temperatures with increasing S concentration, whilst A_{bckgrd} remains approximately constant. This could be caused by either magnetic impurities or muonium. In the latter case, a thermalized positive muon picks up an electron and form a neutral atomic state. Magnetization data from $FeTe_{1-x}S_x$ (see Fig. 3.18) show almost no evidence of magnetic impurities. However, EDAX measurements show that the solubility of S in FeTe reaches saturation at 16%. The behaviour of pure S is quite complex, but an interesting feature is that implanting muons into S gives 100% muonium, which causes a complete loss of asymmetry. Therefore, we attribute the gradual reduction of A_0 with composition to an excessed S, and the estimated amount is in broad agreement with the EDAX measurements.

Figure 3.27 shows the muon depolarization rate (λ) as a function of temperature. As expected the depolarization rate shows a peak at the superconducting transition. Interestingly, the higher relaxation rate (λ_1) seems to show a double peak. The lower temperature peak in λ_1 is close to the peak position in λ_2 are are taken to indicate the superconducting transition temperature, T_c. The peak at high temperature in λ_1 may be due an antiferromagnetic (AF) transition. In analogy with FeTe [96], this AF transition may be due to a SDW (spin density wave) transition associated with an ordering of the iron spins. A similar AF transition has also been observed in the magnetization measurments on the same sample. However,

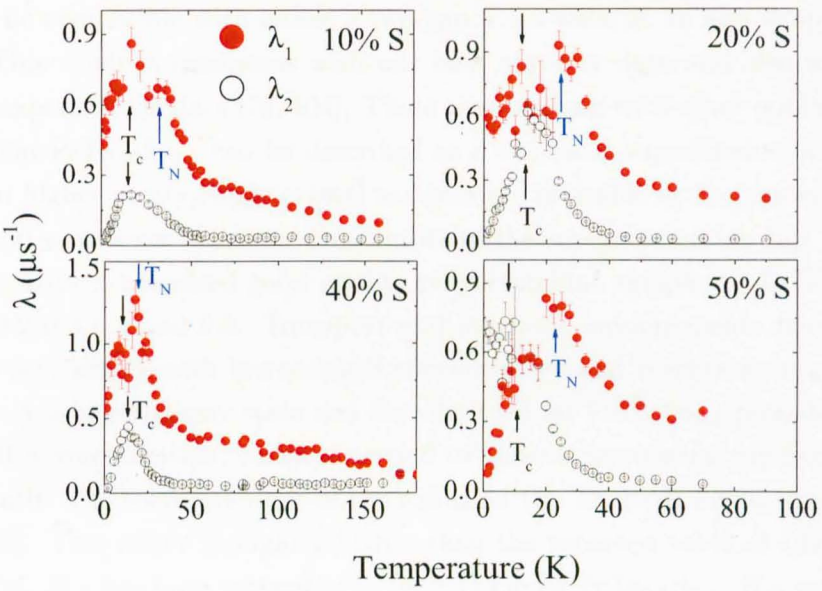

Figure 3.27: The temperature dependence of the muon depolarization rate λ of $FeTe_{1-x}S_x$ for 10%, 20%, 40%, and 50% S compositions.

more studies are required to establish the exact nature of these magnetic transitions seen in the $FeTe_{1-x}S_x$ system.

3.5 Summary and Conclusions

We have synthesized polycrystalline and single crystal samples of $FeTe_{0.5}Se_{0.5}$. Our detailed studies of the structural, magnetic, thermodynamic and other superconducting properties of this sample reveal several important results. A superconducting transition at 14 K have been confirmed using susceptibility, resistivity and specific heat measurements. We have measured the temperature dependence of the resistivity of $FeTe_{0.5}Se_{0.5}$ at different magnetic fields. The upper critical fields at absolute zero have been estimated from the resistivity at different applied magnetic fields. We have investigated the temperature dependence of specific heat of $FeTe_{0.5}Se_{0.5}$. We have used the the specific heat of a non-superconducting sample $FeTe_{0.75}Se_{0.25}$ as a reference and separated the electronic specific heat of $FeTe_{0.5}Se_{0.5}$. Our analysis also shows that the electronic specific heat of $FeTe_{0.5}Se_{0.5}$ can be fitted using a two-band BCS model with isotropic gaps.

We have also performed μSR measurements on superconducting $FeTe_{0.5}Se_{0.5}$. The temperature dependence of the magnetic penetration depth of $FeTe_{0.5}Se_{0.5}$ is

found to be compatible with either a two-gap $s + s$-wave or an anisotropic s-wave model. This result is consistent with our heat capacity data and also with other reported experimental data [76, 104]. These results along with other published data suggest that $FeTe_{0.5}Se_{0.5}$ can be described as a two-band superconductor. Further studies on higher purity single crystal samples are desirable as the presence of impurities can sometimes mask the true nature of the superconducting gap. [105]

We have synthesized good quality polycrystalline samples of $FeTe_{1-x}S_x$ for $x = 0.1, 0.2, 0.3, 0.4$ and 0.5. Transport and magnetic measurements show that T_c increases very slowly with increasing S concentration and reaches a maximum for $x = 0.40$. A zero resistivity state was not observed for $FeTe_{0.9}S_{0.1}$ probably due to very small S concentration, which is needed to make a percolating superconducting current path. The solubility limit of the sulfur on the Te site is found to be around (16 ± 2) %. This result is slightly higher than the reported value of 12% for this system [74]. H_{c1} has been estimated to be 5(1) Oe for $FeTe_{0.6}S_{0.4}$. H_{c2} values have been estimated for $FeTe_{0.6}S_{0.4}$ using the GL theory and the WHH model. ξ and λ have been calculated to be 2.05 nm and 664(1) nm respectively for $FeTe_{0.6}S_{0.4}$. The T_c of $FeTe_{0.5}S_{0.5}$ is found to decrease linearly with pressure with the pressure coefficient, $dT_c/dP = -0.27(1)$ K/kbar. The results are consistent with other experimental data of the $FeTe_{1-x}S_x$ system [69, 102] but different compared to the other iron chalchogenide superconductors where T_c initially increases with P and goes through a broad maximum and decreases thereafter. This different scenario can be understood by its structural phase transition with pressure. μSR experiments have been performed on four different compositions of $FeTe_{1-x}S_x$. μSR data show a AF transition at low temperature. Similar AF transitions have also been observed in the magnetization data of $FeTe_{1-x}S_x$ system. The magnetic transitions may be due to an ordering of the iron spins. More studies are required to understand the exact nature of these magnetic transitions seen in the $FeTe_{1-x}S_x$ system.

Chapter 4

Two-gap Superconductivity in $Lu_2Fe_3Si_5$

4.1 Introduction

The discovery of superconductivity in MgB_2 with a $T_c \sim 39$ K [13] has generated a great deal of interest in superconducting materials containing light elements such as B, C, and Si. Among these materials, the ternary-iron silicide superconductors $R_2Fe_3Si_5$ with R = Lu, Y, Sc, Tm, or Er are particularly noteworthy due to the presence of iron [106, 107]. The ternary-iron silicides, $R_2Fe_3Si_5$ were first reported as superconducting by Braun in 1980 [106]. The properties of these materials are peculiar in several respects. For instance, these compounds have high superconducting critical temperatures (6.1, 4.5, and 2.4 K for compounds with Re = Lu, Sc and Y, respectively) among the Fe-based superconductors, other than the recently discovered FeAs and FeSe families as discussed in Chapter 3. Mössbauer experiments suggest that in these materials the iron possesses no magnetic moment [108]. The local magnetic moment of an atom depends on the local bonding environment. According to Umarji *et al.* [109], the moment of iron is quenched primarily because the Fe-Si separation is much smaller than the sum of the individual metallic radii. This leads to a strong covalent interaction between Fe and Si. The effect of pressure on $R_2Fe_3Si_5$ is very unusual. A large negative pressure effect on T_c has been observed in $Lu_2Fe_3Si_5$ and $Sc_2Fe_3Si_5$ ($dT_c/dp = -7 \times 10^{-5}$ K/bar), whilst a large positive pressure effect on T_c is exhibited in $Y_2Fe_3Si_5$ ($dT_c/dp = 33 \times 10^{-5}$ K/bar) [110]. Reentrant superconductivity has been reported in $Tm_2Fe_3Si_5$ [107]. The coexistence of superconductivity and magnetism has also been reported in $Er_2Fe_3Si_5$ [111].

$Lu_2Fe_3Si_5$ is one of the most interesting of the ternary-iron silicide super-

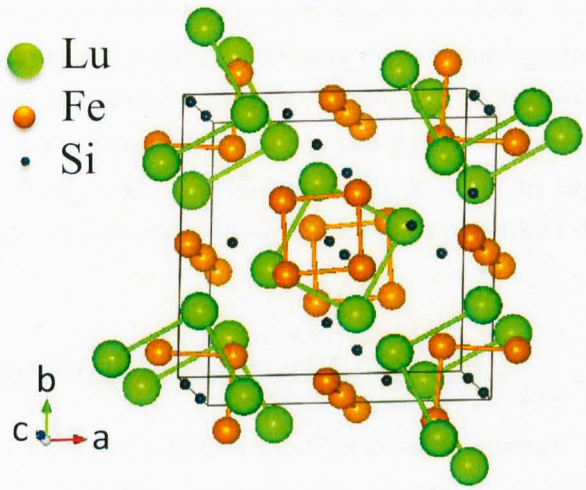

Figure 4.1: Crystallographic structure of $Lu_2Fe_3Si_5$.

conductors because of its high superconducting transition temperature, large upper critical field (H_{c2} = 60 kOe) [106, 109] and unconventional superconducting properties. This compound crystallizes in the tetragonal $Sc_2Fe_3Si_5$-type structure (space group $P4/mnc$) consisting of quasi one-dimensional iron chains along the c-axis and quasi two-dimensional iron squares parallel to the basal plane [112]. Fig. 4.1 shows the crystal structure of $Lu_2Fe_3Si_5$. It is noteworthy that the other two isoelectronic compounds $Lu_2Ru_3Si_5$ and $Lu_2Os_3Si_5$ are not superconducting [113]. This implies that the *3d* electrons in $Lu_2Fe_3Si_5$ play a significant role in the occurrence of the superconductivity in this system. Anisotropy in the upper critical field and a pronounced peak effect have also been reported in $Lu_2Fe_3Si_5$ from magnetic measurements [114]. Moreover, there is a rapid decrease in T_c when a small amount of nonmagnetic impurity replaces some of Fe atoms in $Lu_2Fe_3Si_5$ [115]. According to Anderson's theorem, adding a small amount of non-magnetic impurity to a conventional s-wave superconductor does not affect its T_c or the superconducting density of states [116]. This behaviour in $Lu_2Fe_3Si_5$ is thus incompatible with the isotropic s-wave BCS picture and hence allows us to speculate on the possibility of the existence of spin-triplet superconductivity in $Lu_2Fe_3Si_5$. On the other hand, Josephson effect measurements between $Lu_2Fe_3Si_5$ and Nb have indicated an s-wave pairing mechanism in this system [117]. However, recently, a detailed study of the low-temperature specific heat on a single crystal of $Lu_2Fe_3Si_5$ revealed two-gap superconductivity similar to that seen in MgB_2 [31].

To reveal the pairing mechanism of the exotic superconductivity in $Lu_2Fe_3Si_5$,

it is crucial to determine the superconducting gap function. To clarify the superconducting gap symmetry of $Lu_2Fe_3Si_5$, we have carried out a series of low-temperature μSR measurements on a polycrystalline sample. We show that the temperature dependence of λ can be well described using a two-gap $s+s$-wave model. We also study the low-temperature specific heat of $Lu_2Fe_3Si_5$ in order to support the validity of the two-gap model. We compare these results with published data for the $R_2Fe_3Si_5$ system.

4.2 Sample Preparation of $Lu_2Fe_3Si_5$

Polycrystalline samples of $Lu_2Fe_3Si_5$ were prepared by melting a stoichiometric mixture of lutetium shot (99.99%), iron granules (99.999%) and silicon pieces (99.99%) in an arc furnace under an argon atmosphere [see 2.1.1]. The as-cast sample was poorly superconducting with a T_c = 4.8 K and a broad transition. In order to improve these characteristics, it is essential to anneal the as-cast samples at high temperature for a long period of time [118, 31]. The as-cast sample was sealed in a quartz tube under a partial pressure of argon. The sample was then heated at a rate of 200°C/h to 800°C, held at this temperature for 48 h, then heated at the same rate to 1100°C and held at this temperature for 72 h. The sample was then cooled at 200°C/h to 800°C, maintained at this temperature for 72 h, and then finally cooled to room temperature.

4.3 Magnetization Measurements of $Lu_2Fe_3Si_5$

Temperature dependence of the dc magnetic susceptibility of $Lu_2Fe_3Si_5$ were performed by using a *Quantum Design* Magnetic Property Measurement System (MPMS) magnetometer [see section 2.3.1 for more details]. Data were taken both in zero-field-cooled warming (ZFCW) and field-cooled cooling (FCC) modes. The temperature dependence of the diamagnetic susceptibility shows that $Lu_2Fe_3Si_5$ has a superconducting transition temperature T_c (onset) of (6.1±0.1) K [see Fig. 4.2]. In the ZFCW mode, the temperature dependence of the susceptibility of $Lu_2Fe_3Si_5$ reaches a value close to -1. This implies that the superconducting volume fraction of $Lu_2Fe_3Si_5$ is nearly 100%.

Magnetization measurements were performed to check the sample quality and the T_c value of $Lu_2Fe_3Si_5$. However, to find the magnitude and the symmetry of the superconducting gap, we have performed low temperature specific heat measurements on $Lu_2Fe_3Si_5$.

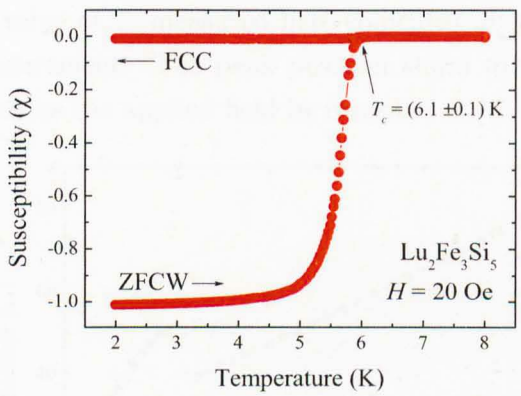

Figure 4.2: The temperature dependence of the dc magnetic susceptibility of $Lu_2Fe_3Si_5$ measured using both zero-field-cooled warming (ZFCW) and field-cooled cooling (FCC). The diamagnetic susceptibility shows a T_c onset of (6.1 ± 0.1) K.

4.4 Heat Capacity Measurements of $Lu_2Fe_3Si_5$

Low-temperature specific heat measurements were carried out using a two-tau relaxation method in a *Quantum Design* Physical Property Measurement System (PPMS) equipped with a ^{3}He insert [see 2.3.3].

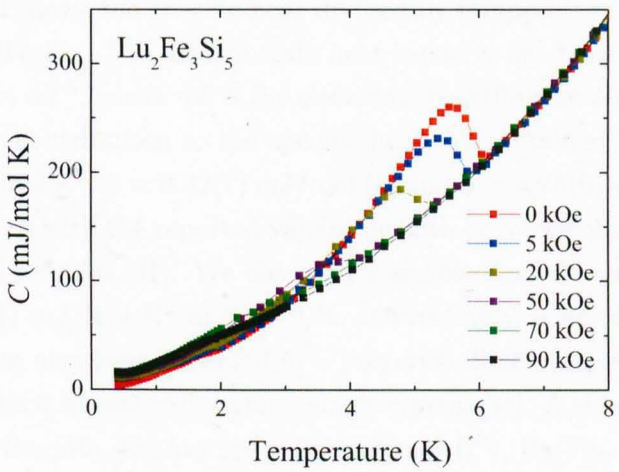

Figure 4.3: Temperature dependence of specific heat of $Lu_2Fe_3Si_5$ in various applied magnetic fields.

Figure. 4.3 shows the temperature dependence of the specific heat of $Lu_2Fe_3Si_5$ at different applied fields. In the zero field specific heat data, a pronounced jump

is observed starting at 6.1 K which indicates that the sample exhibits bulk superconductivity. The value of T_c measured here coincides with the T_c found from the magnetization measurement. The peak position shifts toward lower temperature and also get broaden as the applied field increases.

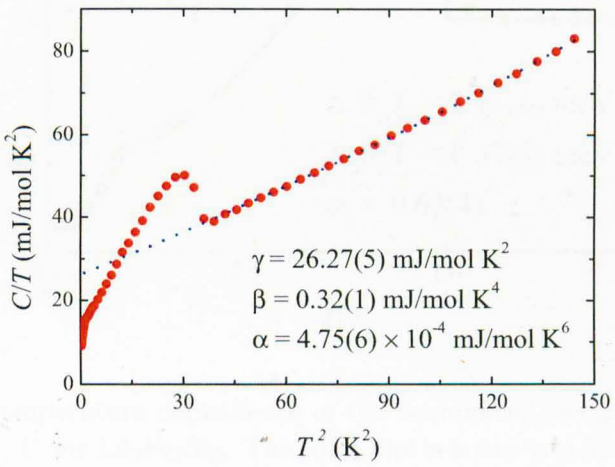

Figure 4.4: The specific heat divided by temperature (C/T) as a function of T^2 for $Lu_2Fe_3Si_5$. The dashed line shows the fit to the data in the normal state using the equation $C = \gamma T + \beta T^3 + \alpha T^5$.

Figure. 4.4 shows the specific heat divided by temperature (C/T) as a function of T^2 for $Lu_2Fe_3Si_5$. The normal state heat capacity has been fitted up to 12 K by $C = \gamma T + \beta T^3 + \alpha T^5$, where γT is the electronic contribution and $\beta T^3 + \alpha T^5$ represents the lattice contribution to the specific heat. We obtained fitted parameters $\gamma = 26.27(5)$ mJ/mol K^2, $\beta = 0.32(1)$ mJ/mol K^4 and $\alpha = 4.75(6) \times 10^{-4}$ mJ/mol K^6 which are consistent with the reported values for both polycrystalline [119, 120, 114] and single crystal samples [31]. We observed a sizable residual specific heat coefficient, $\gamma_r = 7.21(1)$ mJ/mol K^2 at $T = 0$ K. Interestingly, a finite residual specific heat coefficient has also been observed in a polycrystalline sample of the same system [114] whereas it is absent in data for a single crystal [31]. A similar effect has also been reported in $Ba_{0.6}K_{0.4}Fe_2As_2$ ($\gamma_r = 7.7$ mJ/mol K^2), $Ba(Fe_{1-x}Co_x)_2As_2$ ($\gamma_r = 3.0$ mJ/mol K^2) and $Ba(Fe_{0.92}Co_{0.08})_2As_2$ ($\gamma_r = 3.7$ mJ/mol K^2) [121, 122, 123]. Possible explanations for this residual specific heat coefficient involve pair breaking effects of an unconventional superconductor due to the presence of some impurities in the sample [124], spin glass behaviour or crystallographic defects [123]. Given the metallurgy of our polycrystalline sample and the dramatic effects that annealing has on the electronic properties, we suggest that crystallographic defects are the most

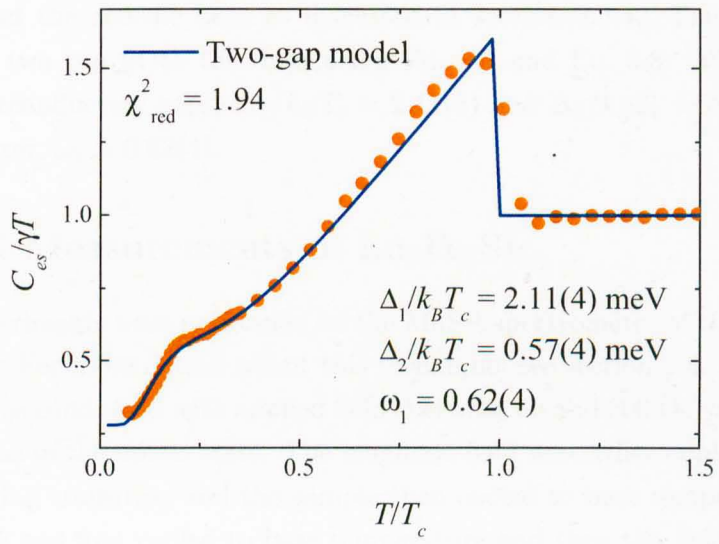

Figure 4.5: The temperature dependence of the normalized electronic specific heat as a function of T/T_c for $Lu_2Fe_3Si_5$. The solid line is a two-gap fit to the data using Eq. 3.7 and Eq. 3.8.

likely cause of the residual specific heat coefficient in the heat capacity data.

If the superconducting and nonsuperconducting regions have similar heat capacities then the volume fractions of normal and superconducting material can be expressed as γ_r/γ and $1 - \gamma_r/\gamma$, respectively. On this basis, the total electronic specific heat is the sum of contributions of the superconducting and normal phases and consequently, the electronic specific heat can be normalized to one mole of superconducting material, C_{es}, defined by:

$$C_{es} = (C_e - \gamma_r T).\frac{\gamma}{\gamma - \gamma_r} \tag{4.1}$$

where C_e is the electronic specific heat and is calculated by subtracting the lattice contribution from the total specific heat. Fig. 4.5 shows the temperature dependence of the normalized electronic specific heat, $C_{es}/\gamma T$, for $Lu_2Fe_3Si_5$ as a function of T/T_c. We find two clear anomalies in the temperature dependence of electronic specific heat data of $Lu_2Fe_3Si_5$. A large jump appears at T_c and a smaller one at $T_c/5$. The value of $C_{es}/\gamma T$ at T_c is found to be 1.13(1) meV, which is much smaller than the BCS value of 1.43 meV but similar to the value of 1.05 meV measured on a single crystal [31] and also agrees well with the reported values for polycrystalline samples [119, 120, 114]. To perform a two-gap fit to the $C_{es}/\gamma T$ data in the superconducting state, we use the BCS expressions for the normalized

entropy S and the specific heat as discussed in section 3.3.4. The solid line in Fig. 4.5 is a two-gap fit to the data using Eq. 3.7 and Eq. 3.8. We obtain two distinct superconducting gaps, $\Delta_1/k_BT_c = 2.11(4)$ and $\Delta_2/k_BT_c = 0.57(4)$ with a weighting factor, $\omega_1 = 0.62(4)$.

4.5 μSR Measurements of $Lu_2Fe_3Si_5$

The μSR experiments were performed on the MuSR spectrometer of the ISIS pulsed muon facility. For more details about this technique, see section 2.4. The TF-μSR experiment was conducted with applied fields between 50 and 600 Oe, which ensured the sample was in the mixed state. The magnetic field was either applied above the superconducting transition and the sample then cooled to base temperature (FC), or the sample was first cooled to base temperature and then the field was applied (ZFC). The sample was mounted on a silver plate with a circular area of ~ 700 mm^2 and a small amount of diluted GE varnish was added to aid thermal contact. The sample and mount were then inserted into an Oxford Instruments He^3 sorbtion cryostat. Any silver exposed to the muon beam gives a background described by non-decaying sine wave.

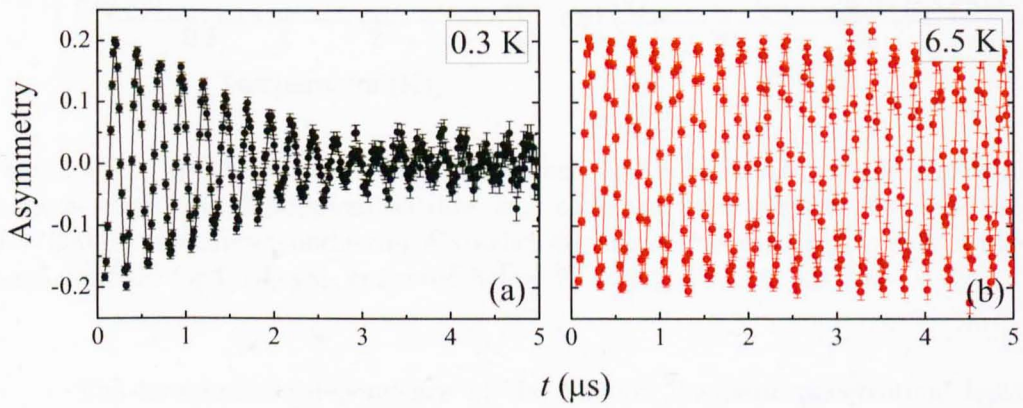

Figure 4.6: The transverse-field muon-time spectra (one component) for $Lu_2Fe_3Si_5$ collected (a) at $T = 6.5$ K and (b) at $T = 0.3$ K in a magnetic field $H = 300$ Oe.

TF-μSR precession signals above and below $T_c = 6.1$ K are shown in Figure 4.6. Above the superconducting transition i.e. in the normal state, the signal decays very slowly, but the decay is relatively fast in the superconducting state due to the inhomogeneous field distribution from the flux-line lattice. We can model these inhomogeneous field distributions using an oscillatory decaying Gaussian function

$$G_X(t) = A_0 \exp\left(-\sigma^2 t^2 / 2\right) \cos\left(\omega_1 t + \phi\right) + A_1 \cos\left(\omega_2 t + \phi\right), \tag{4.2}$$

where ω_1 and ω_2 are the frequencies of the muon precession signal and background signal respectively, ϕ is the initial phase offset, and σ is the Gaussian muon spin relaxation rate. Fig. 4.7a shows the temperature dependence of σ_{sc} obtained in an applied TF of 300 Oe. Fig. 4.7b presents the magnetic field dependence of σ_{sc} collected at different temperatures below the superconducting transition. A deviation in the field dependence of σ_{sc} is observed at 400 Oe in 0.3 K data. A small deviation of σ_{sc} is also present at the same field in 2 K data, whereas it is constant above 2 K.

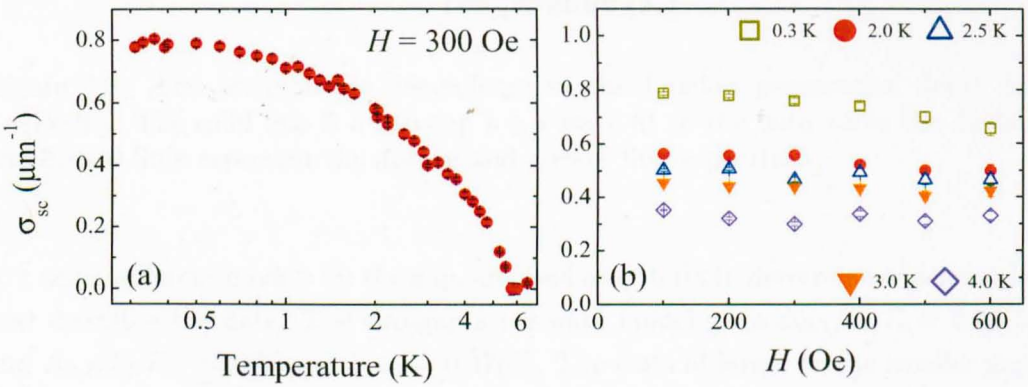

Figure 4.7: (a) The temperature dependence (on a log scale) of the superconducting muon spin depolarization rate, σ_{sc}, collected in an applied magnetic field $H = 300$ Oe. (b) Superconducting Gaussian depolarization rate, σ_{sc}, versus applied magnetic field for $Lu_2Fe_3Si_5$ collected below T_c at 0.3, 2.0, 2.5, 3.0 and 4.0 K.

The temperature dependence of the London magnetic penetration depth, $\lambda(T)$ is coupled with the superconducting Gaussian muon-spin depolarization rate, $\sigma_{sc}(T)$ by the equation 3.11. $\lambda(T)$ can then be fitted using either a single gap or a two-gap model which are structured on the basis of the α-model [23, 85] and described in section 3.3.5.

Fits to the data using the three different models are shown in Fig. 4.8. The fits rule out the s-wave and d-wave models as possible descriptions for $Lu_2Fe_3Si_5$ as the χ^2_{red} values for these models are 33.92 and 15.91 respectively. The two-gap $s + s$-wave model gives a good fit to the data with a χ^2_{red} of 1.94. The normalized χ^2_{red} values, resulting from our least squares fits to the temperature dependence of

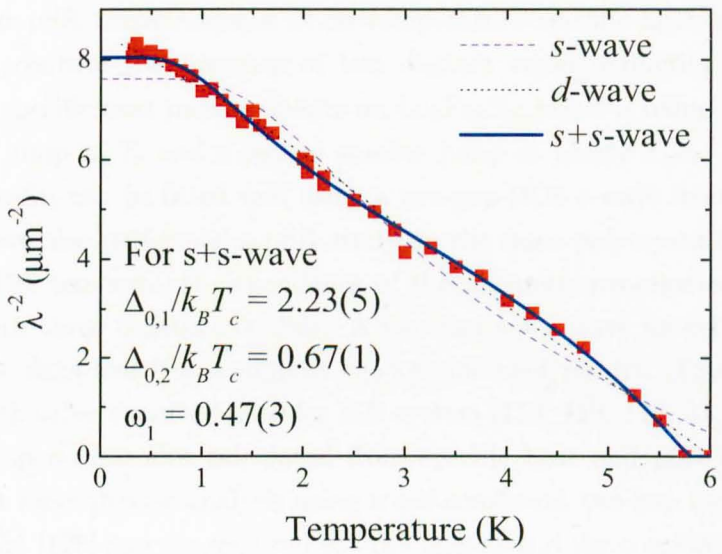

Figure 4.8: The temperature dependence of the London penetration depth for $Lu_2Fe_3Si_5$. The solid line is a two-gap $s + s$-wave fit to the data while the dashed and dotted lines represent the d-wave and s-wave fits respectively.

λ^{-2} using different models for the gap, are used as criteria to determine which model best describes the data. The two-gap $s + s$-wave model gives $\Delta_{0,1}/k_BT_c = 2.23(5)$ and $\Delta_{0,2}/k_BT_c = 0.67(1)$ with $\omega_1 = 0.47(3)$. The ratio of larger to the smaller gap, $\frac{\Delta_{0,1}}{\Delta_{0,2}} \approx 3.33(9)$, which is slightly lower than the value 5 obtained by low-temperature specific heat measurement [31], but consistent with the value 3.44 obtained by penetration depth measurement using the tunnel-diode resonator technique [125] on a single crystal of $Lu_2Fe_3Si_5$. The ratio is also close to the value 4.18, obtained from the specific heat measurements on the same sample. The magnetic penetration depth at $T = 0$ K is found to be $\lambda(0) = 353(1)$ nm. The in-plane penetration depth is 200 nm, obtained by tunnel-diode resonator technique [125]. The weighting factor, $\omega_1 = 0.47(3)$, which is slightly smaller than the value obtained from fits to the specific heat data. The good agreement between the μSR and heat capacity data and the two-gap model argues in favour of the presence of two distinct superconducting gaps in $Lu_2Fe_3Si_5$.

4.6 Summary and Conclusions

We have synthesized high quality polycrystalline samples of $Lu_2Fe_3Si_5$. A superconducting transition at around 6.1 K have been confirmed using susceptibility, spe-

cific heat and μSR measurements. Low-temperature specific heat measurements of $Lu_2Fe_3Si_5$ confirm the presence of two distinct superconducting gaps. Low-temperature specific heat measurements on $Lu_2Fe_3Si_5$ reveal a reduced normalized specific heat jump at T_c and a second smaller jump at nearly $T_c/5$. Specific heat data of $Lu_2Fe_3Si_5$ can be fitted well using a two-gap BCS s-wave model.

We have also performed a μSR study on the same polycrystalline sample of $Lu_2Fe_3Si_5$. The temperature dependence of the magnetic penetration depth data was fitted with three different models. A two-gap $s + s$-wave model provides the best fit to the data and hence support the specific heat results. These results are consistent with other reported data for this system [119, 120, 114, 31, 125].

The gap magnitudes calculated from specific heat and μSR studies agree reasonably. A more precise analysis using a self-consistent two-gap model proposed by Kogan *et al.* [126] may be required to fully understand the coupling strength between the two bands in this system. The self-consistent model has been developed within the quasi-classical Eilenberger weak-coupling formalism with one inter-band and two in-band pairing potentials. The model has been tested with the experimental data of well-known two-band superconductors MgB_2 and V_3Si. Work is under way to explain our specific heat and μSR data using this model.

Chapter 5

Flux-Line Lattice in $6H$-CaAlSi

5.1 Introduction

Magnesium diboride, MgB_2, has the highest transition temperature (T_c of 39 K) for a simple binary compound [13]. In MgB_2 there are two distinct energy gaps associated with different parts of the Fermi surface. The larger gap (7 meV) originates from holelike carriers residing on two cylindrical Fermi surface sheets, derived from σ bonding of the Pxy boron orbitals and called the σ band. The smaller gap (2 meV) originates from two 3D sheets of electron and holelike carriers, derived from π bonding of the Pz orbitals and called the π band. However, there are important questions concerning the superconducting mechanism that are still to be addressed. The best way to answer these questions is to investigate the various properties of similar systems. A few gallium-based binary compounds $CaGa_2$, $SrGa_2$, and $BaGa_2$ crystallize in to similar AlB_2-type structures but are not superconducting [127]. A high pressure superconducting phase of $CaSi_2$ with a T_c of 14 K also has the similar crystallographic structure [128]. However, a new group of pseudoternary compounds of the AlB_2-type structure with the general formula $A(M_{1-x}Si_x)$ (A = Ca, Sr, Ba and M = Al, Ga) turn out to have rich physics in various aspects of superconductivity [129, 130, 131, 132]. Among these compounds, CaAlSi with the highest superconducting transition temperature, T_c, of 7.8 K under ambient pressure [130], has attracted considerable interest as a reference material for understanding the key factors leading to such a high T_c in MgB_2. The ternary Ca-Al-Si system has another compound with a layered structure, $CaAl_2Si_2$. It has the La_2O_3-type structure [space-group $P\bar{3}m1$ (No. 164)], where the Si and Al atoms are arranged in the chemically ordered double-corrugated hexagonal layers and Ca atoms are intercalated between them. It is interesting to note that this compound

is not superconducting above 1.4 K, showing semimetal behaviour with the opening of a pseudogap in the Fermi level [133, 134]. CaAlSi exhibits a number of interesting superconducting properties, the study of which can provide an insight into the factors leading to high superconducting transition temperatures (T_c) in this class of materials. There is no reasonable correlation of T_c with the mass of the alkaline-earth-metal ion (A) in the compound A-GaSi. However, in AAlSi T_c decreases systematically with increasing mass of the A ion from 7.8 K (A = Ca) to 5 K (A = Sr) and BaAlSi is not superconducting above 2 K [135, 136]. In this case, the decrease of the electron-phonon coupling along the Ca, Sr, Ba sequence has been taken as a consequence of a decreasing density of states at the Fermi level (ρ_{EF}) [136] or the hardness of a soft mode which is present in CaAlSi but absent in the Ba compound [137, 138].

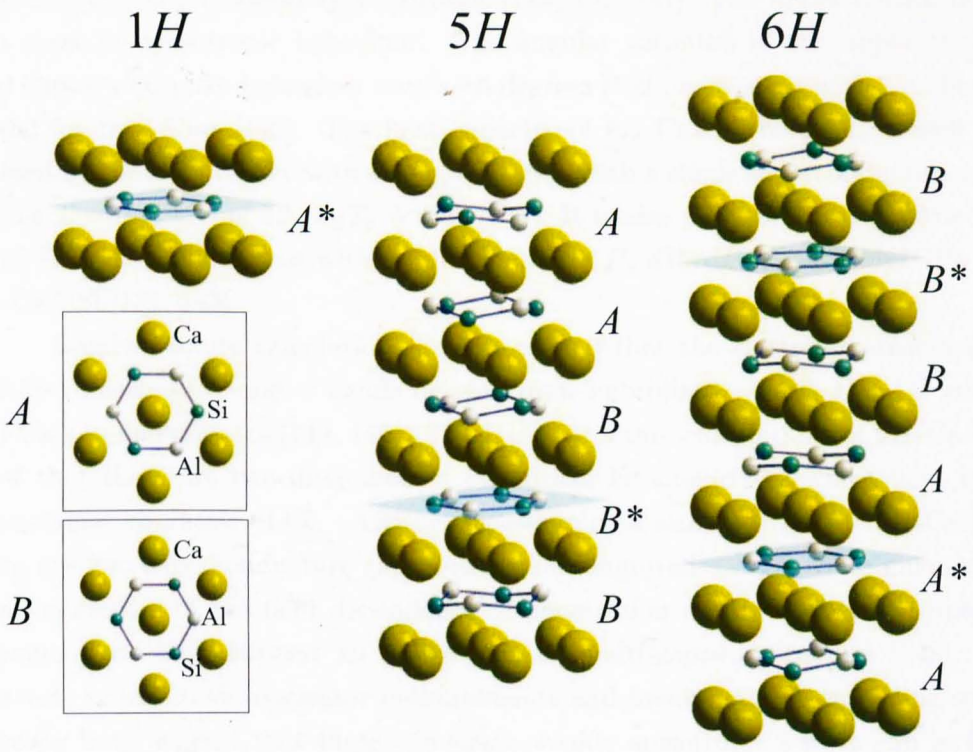

Figure 5.1: Crystal structure of $1H$, $5H$, and $6H$-CaAlSi which are characterized by a different sequence of A and B layers. A and B layers are rotated by 60° around the c-axis with respect to each other. Flat and buckled Al-Si layers are indicated with and without an asterisk, respectively.

Neutron and x-ray diffraction studies have shown that there are two possible

arrangements for the atoms in the hexagonal AlSi layers in CaAlSi, denoted as A and B shown in Fig. 5.1. The A and B layers differ by a 60° rotation around the c-axis [139, 140]. These layers stack along the c-axis in a sequence ($AABBB$) in five-fold $5H$-CaAlSi and ($AAABBB$) in six-fold $6H$-CaAlSi. Stacking of the A and B layers induces an internal stress on the structure, causing a buckling of boundary layers. It was also found that the superconducting properties depend strongly on the kind of stacking of the A and B layers. Further distortions produce either corrugated or flat AlSi layers within the multi stack structures [139]. An unmodulated phase ($1H$-CaAlSi) can also be grown by controlled cooling from the molten state [140].

The superconducting properties of CaAlSi, including $H_{c2}(T)$ and T_c (5.7 to 7.7 K), change with modulation, as does the anisotropy $\gamma_H = H_{c2}^{ab}/H_{c2}^{c}$ or $\gamma_\lambda = \lambda_c/\lambda_{ab}$ of the superconductivity, although γ values of 2-3 indicate that these materials are only moderately anisotropic [129, 132, 141]. The upper critical fields also show an anisotropic behaviour. The angular variation of the upper critical field shows a cusplike behaviour near zero degrees [132], consistent with Tinkham's model for thin films [142]. The heat capacity of $6H$-CaAlSi below T_c is well explained by the BCS theory with strong-coupling, with a single superconducting gap, 2Δ, at $T = 0$ K giving $2\Delta/k_BT_c = 4.07$ [131]. It is also noteworthy that while the T_c of $1H$-CaAlSi decreases with applied pressure P, $dT_c/dP = +0.21$ K/GPa for $6H$-CaAlSi [131, 143].

Band-structure calculations have predicted that the electronic structure of CaAlSi consists of σ and π bands derived from hybridized (Al,Si) s and p states and Ca s, p and d states [144, 145, 137]. Band-structure calculations of $6H$-CaAlSi show that there are two disconnected cylindrical Fermi-surfaces which have two-dimensional character [146]. ARPES measurements indicate that in $6H$-CaAlSi there are two superconducting gaps with equal magnitudes [147] while muon spin rotation studies of the field dependence of penetration depth λ [141] and optical measurements both suggest an anisotropic or multi-gapped structure [148]. In contrast, tunnel-diode resonator measurements and break-junction tunneling spectroscopy both suggest that there is a single weakly anisotropic s-wave gap in $6H$-CaAlSi [149, 150].

Here, we report the synthesis of a single crystal of $6H$-CaAlSi. The sample characterization was done by single crystal X-ray diffraction, magnetization and resistivity measurements. We also present the results of a small angle neutron scattering (SANS) study of the magnetic flux line lattice (FLL) in the $6H$ phase of CaAlSi. SANS is a powerful technique for studying the FLL in the mixed state of type-II superconductors [151] and has often been used to investigate the symmetry

of the underlying electronic structure, details of the pairing mechanism, and the macroscopic physics of the FLL [152, 153, 154, 155, 156, 157, 158, 159]. We observe the FLL at a very low field of 54 Oe. The data also show a 30° reorientation of the FLL in $6H$-CaAlSi in a field of only 200 Oe. At low fields the sixfold symmetric diffraction pattern with Bragg peaks align themselves along one high symmetry direction of the crystal lattice and at high fields, they move to another high symmetry direction. We estimate the penetration depth, λ, and the coherence length, ξ of CaAlSi by analyzing the form factor data. We also estimate the penetration depth anisotropy γ_λ, by measuring the FLL for fields applied at different angles to the c-axis. Unlike MgB_2, the anisotropy of this coherence length is the same as the anisotropy of the penetration depth in CaAlSi.

5.2 Single Crystal Growth of $6H$-CaAlSi

A single crystal of $6H$-CaAlSi was prepared by the Bridgman method. For more details about the Bridgman method, read section 2.1.2. A polycrystalline ingot of CaAlSi was first made by melting a stoichiometric mixture of calcium shot (99.99%), aluminum shot (99.999%) and silicon pieces (99.99%) in an arc furnace under flowing argon gas. The as cast ingot was placed in a boron nitride crucible with a conical shaped bottom, and then sealed in a quartz tube under vacuum. The tube was placed in a vertical Bridgman furnace, heated to 1010°C at 100°C/h, and then held at this temperature for 24 h. Crystal growth was carried out by lowering the tube at a rate of 3 mm/h.

5.3 Single Crystal X-ray Diffraction of $6H$-CaAlSi

An Oxford Diffraction CCD single crystal diffractometer was used to study the structural modulation in a single crystal of $6H$-CaAlSi. For more details, see section 2.2.3. A single crystal of dimension $0.20 \times 0.12 \times 0.14$ mm^3 was cleaved from the crystal of CaAlSi used for the small angle neutron scattering (SANS) experiments and attached to a glass fibre with epoxy resin. Principal planes of reciprocal space were reconstructed from this data on the basis of the refined reciprocal lattice to identify the nature of the structural modulation.

Single-crystal X-ray diffraction experiments were performed on CaAlSi to verify the six-fold superlattice structure in our sample. Analysis of the X-ray diffraction data revealed a hexagonal unit cell, with refined lattice parameters of $a = 4.1982(7)$ Å and $c = 26.446(4)$ Å, and an internal R-factor of 0.0889. This cor-

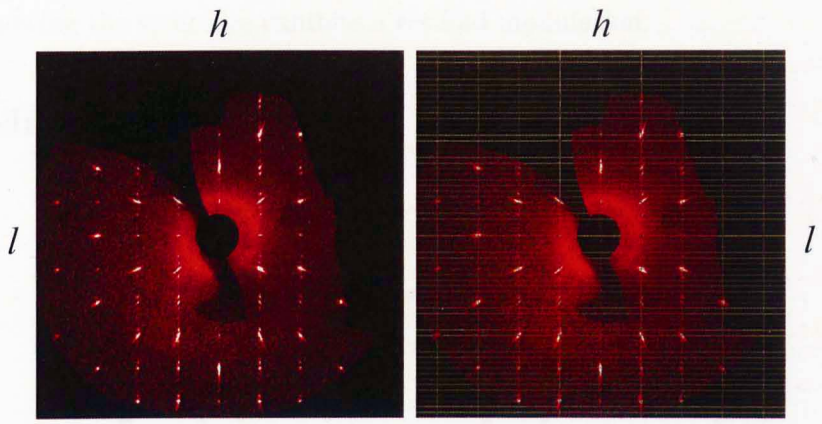

Figure 5.2: Sections of $(h1\ell)$ reciprocal layers both with and without grid, measured at room temperature for the single crystal of $6H$-CaAlSi.

responds to a c/a ratio of 6.30, consistent with $(c/a = 6.31)$ for $6H$-CaAlSi observed by Sagayama *et al.* [139]. Figure 5.2 shows sections of $(h1\ell)$ reciprocal layers both in grid and without grid. The strong reflections correspond to the average structure with the symmetry *P6/mmm* and are separated along the vertical c^*-axis by five superstructure reflections.

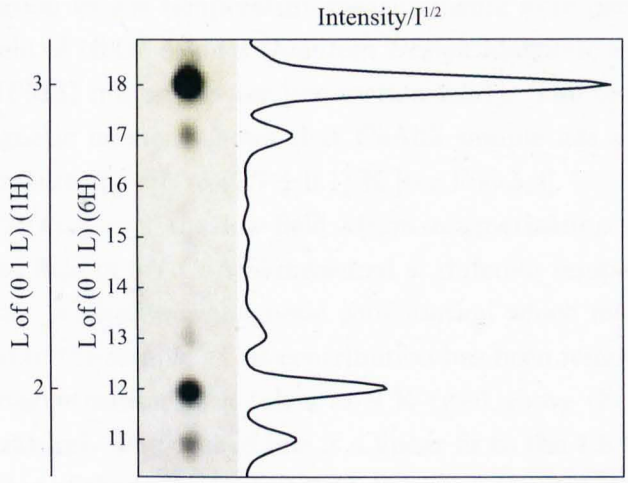

Figure 5.3: X-ray diffraction pattern along the reciprocal lattice line (01ℓ) and a single section of the $(h1\ell)$ reciprocal lattice plane for the $6H$ single crystal of CaAlSi.

Figure 5.3 shows a single section of the $(h1\ell)$ reciprocal lattice plane, indexed with both the unmodulated $(1H)$ and refined modulated $(6H)$ reciprocal lattices,

clearly showing the structure exhibits a six-fold modulation.

5.4 Magnetization Studies of $6H$-CaAlSi

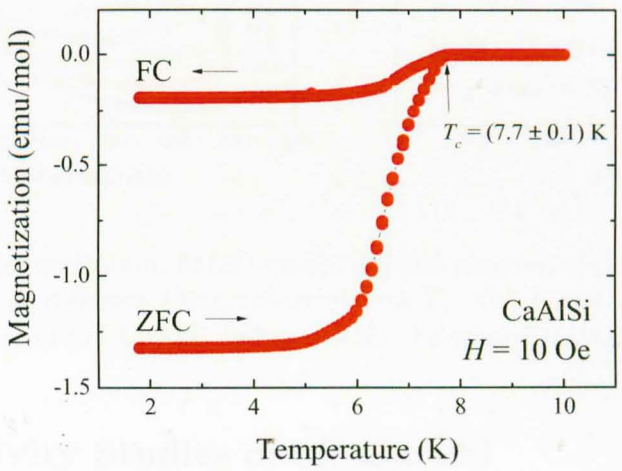

Figure 5.4: Temperature dependence of the magnetic moment for CaAlSi measured in zero-field-cooled and field-cooled mode in an applied magnetic field of 10 Oe.

Magnetization versus temperature measurements were performed in an applied magnetic field of 10 Oe using a *Quantum Design* Magnetic Property Measurement System (MPMS) magnetometer [see section 2.3.1]. The temperature dependence of the magnetic moment shows that CaAlSi sample has a superconducting transition temperature, T_c^{onset}, of (7.7 ± 0.1) K [see Fig. 5.4].

Figure 5.5 (a) shows the low-field virgin magnetization $M(H)$ data as a function of applied field of $6H$-CaAlSi measured at different temperatures. The raw $M(H)$ data contain a small paramagnetic contribution which may come from any impurities present in the sample. This contribution has been removed from the data by subtracting magnetization data taken at 9 K (well above the superconducting transition temperature). The dashed line is a linear fit to the 1.8 K data between 0 to 20 Oe. The value of the lower critical field H_{c1} was determined by measuring the field of first deviation from the linear fit (initial slope of the magnetization curve). Demagnetizing effects are also taken into account in estimating the H_{c1} values. Figure 5.5 (b) shows the H_{c1} versus temperature graph. The H_{c1} data can be fitted well using a quadratic equation $H_{c1}(T) = H_{c1}(0)\left\{1 - (T/T_c)^2\right\}$, where $H_{c1}(0)$ is the lower critical field at zero temperature. The fit yields $H_{c1}(0)$ of 53.4(5) Oe for CaAlSi.

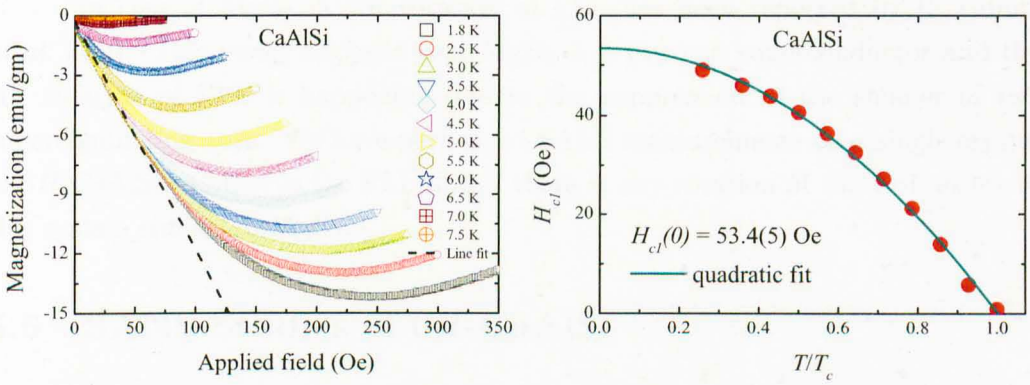

Figure 5.5: (a) Magnetization, $M(H)$ versus applied magnetic field in the low magnetic field region at different temperatures below T_c. (b) Lower critical field, H_{c1} versus temperature of $6H$-CaAlSi deduced from the magnetization measurements.

5.5 Resistivity Studies of $6H$-CaAlSi

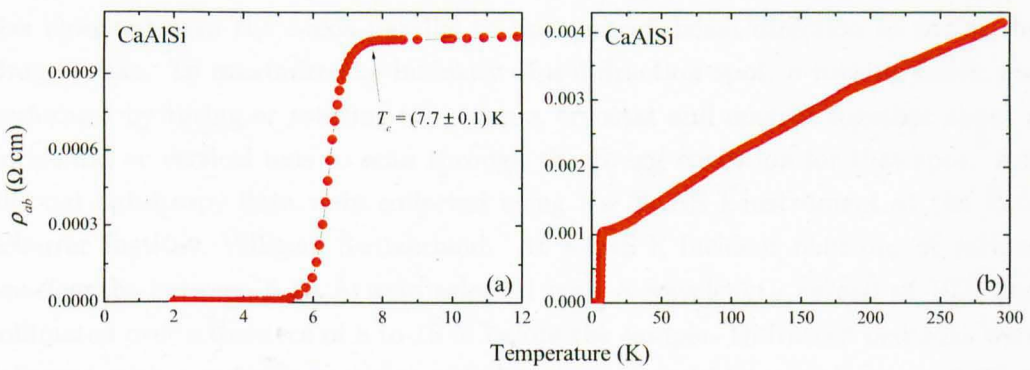

Figure 5.6: In-plane electrical resistivity versus temperature of $6H$-CaAlSi at (a) close to superconducting transition temperature and (b) up to room temperature.

We have measured the in-plane ac electrical resistivity, $\rho_{ab}(T)$, as a function of temperature for CaAlSi via a standard four-probe method using a *Quantum Design* Physical Property Measurement System (PPMS) [for more details, see section 2.3.2]. Fig. 5.6 (a) shows the resistivity for temperatures between 2 to 12 K. $\rho_{ab}(T)$ shows a superconducting transition at 7.7 K with a transition width of 0.9 K. The resistivity curves between 2 to 295 K (see Fig. 5.6 (b))shows metallic behavior for CaAlSi. The relative resistance ratio, $\rho_{ab}(295\ K)/\rho_{ab}(8\ K)$ is 4, similar to the reported data ($\rho_{ab}(298\ K)/\rho_{ab}(8.2\ K) = 4.9$) [160] by Imai *et al.*

In case of MgB_2, a 30^o rotation of FLL has been reported by R. Cubitt *et al.* [161]. This result suggests that MgB_2 is a two-gap superconductor and the 30^o rotation of FLL is happening due to the suppression of the smaller of two superconducting gaps. We have performed SANS measurements on a single crystal of $6H$-CaAlSi to observe the FLL and if there is any rotation of the FLL exists in this system similar to MgB_2.

5.6 SANS Studies of $6H$-CaAlSi

SANS measurements were performed using the D22 instrument at the Institut Laue-Langevin (ILL), Grenoble, France and the SANS I instrument at the Paul Scherrer Institut, Villigen, Switzerland. Read section 2.5 for more details. During the experiment, D22 was configured in a high resolution mode with a mean wavelength of 14 Å and a wavelength spread of 10%, collimation of 17.6 m, and an area detector at a distance of 17.6 m to the sample. An additional circular aperture of diameter 20 mm was also used before the sample to better define the scattered beam at the detector and to equalize the horizontal and vertical divergences. A sample was mounted with the c-axis parallel to the neutron beam direction to access the Bragg peaks. To maximize the intensity of a diffraction spot, a rocking curve was performed by tilting or rotating the sample, cryostat and magnet together about a horizontal or vertical axis to scan through the Bragg condition for that spot. Additional anisotropy data were collected using the SANS I instrument at the Paul Scherrer Institut, Villigen, Switzerland. At SANS I, incident neutrons of various wavelengths between 5-10 Å were selected with a wavelength spread of 10% and collimated over a distance of 8 to 18 m before the sample. Diffracted neutrons were collected with a position-sensitive two-dimensional multidetector located 13-20 m after the sample. For all measurements, the sample was cooled to base temperature in an applied magnetic field H and the data collected while warming the sample in the same field. Background scattering was measured above T_c and subtracted from the low-temperature data.

Figs. 5.7(a)-(d) show the diffraction patterns from the FLL of CaAlSi measured at 2 K in fields, H of (a) 97, (b) 185, (c) 250, and (d) 294 Oe applied parallel to the c-axis. Figs. 5.7(e)-(h) and Figs. 5.7(i)-(l) are the same diffraction patterns taken at 4 K and 5 K, respectively. At the lowest field [Fig. 5.7(a), (e), (f), and (i)] we observe a symmetric hexagonal diffraction pattern with Bragg peaks appearing at 30° to the b-axis of the crystal denoted here as Low-Hex. With increasing field, a second hexagonal diffraction pattern appears oriented along the b-axis [see

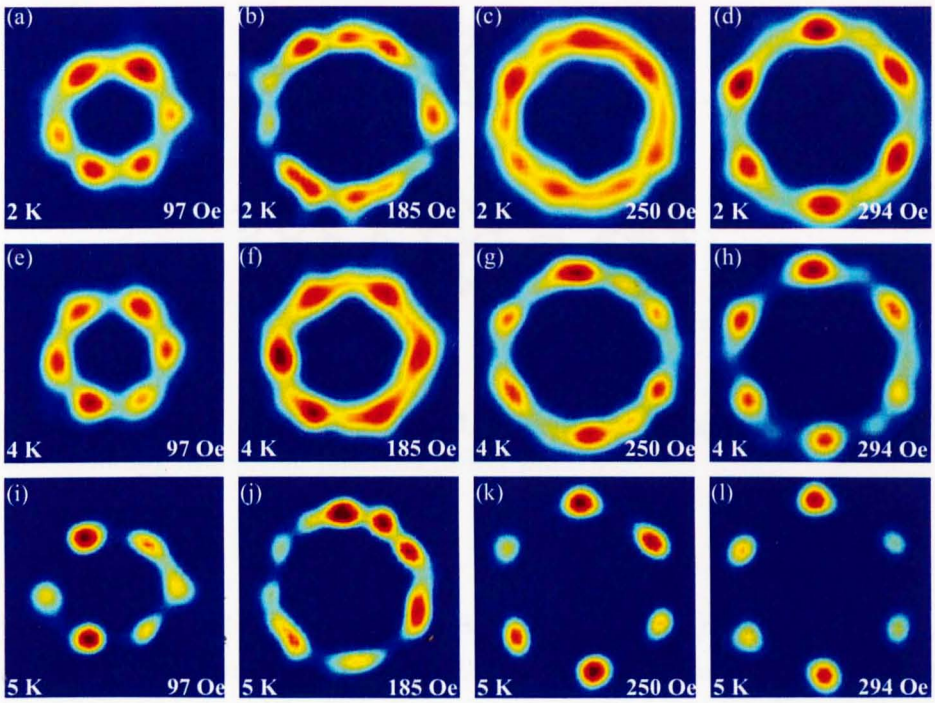

Figure 5.7: (a-l) SANS diffraction patterns of CaAlSi taken at 2 K, 4 K and 5 K in the applied magnetic fields of 97, 185, 250, and 294 Oe, respectively.

Figs. 5.7(b), (c), (g), and (j)]. This means that the FLL has now formed two domains with an angular separation of 30°. As the applied field is increased further the FLL transforms into a single domain with Bragg peaks oriented along the *b*-axis and referred to as High-Hex [Fig. 5.7(d), (h), (k), and (l)]. We did not observe any intermediate structures or any continuous change in the positions of the diffraction peaks during the reorientation process. These observations suggest that the transition between the High and Low-Hex phases is most likely of first-order in character. No further reorientations of the FLL were observed in applied fields of up to 2 kOe.

Fig. 5.8 contains a schematic diagram of the FLL patterns of CaAlSi in real-space (upper panel) and the diffraction patterns (lower panel). The only previous SANS measurements on $6H$-CaAlSi found no evidence for a FLL reorientation as the measurements were not carried out at sufficiently low applied fields [162]. This earlier study also suggested the FLL was not perfectly hexagonal. In our measurements, a perfectly hexagonal lattice was found for all applied fields. It is also worth noting that the lowest applied field (54 Oe) is much smaller than the reported value of H_{c1} [160]. However, from the magnetization(M) vs. H measurements, we found

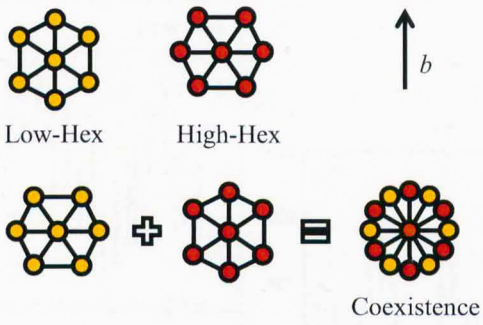

Figure 5.8: Schematic diagram of the FLL patterns in real-space (upper panel) and the corresponding diffraction patterns (lower panel).

$H_{c1} = 50$ Oe at 2 K.

The intensity of the Bragg diffraction peaks for the Low-Hex, High-Hex, and Coexistence phases are shown in Fig. 5.9. The intensity curves were obtained by summing the counts as a function of angle over a half-spherical (between 0° to 180°) block arc encompassing the spots. For the Low-Hex phase [see Fig. 5.9 (a)], we observe intensity peaks at 30°, 90°, and 150°. For High-Hex phase [see Fig. 5.9 (b)], the peaks are at 0°, 60°, 120°, and 180°. This again implies that the FLL in High-Hex phase has rotated by 30° from the Low-Hex phase. In the Coexistence phase [see Fig. 5.9 (c)], we observe peaks both in Low-Hex and High-Hex positions as expected.

An H-T phase diagram of CaAlSi is shown in Fig. 5.10 indicating the regions in which we observe either a purely Low-Hex or a High-Hex phase separated by a region in which the two FLL structures coexist. Fig. 5.11 shows the variation of the integrated intensity of the Bragg spots for the High and Low-Hex states with applied magnetic field at 4 K. The shaded region indicates the coexistence of the two phases. A sudden change of intensity for the two states occurs through this narrow window of coexistence. The coexistence of the two phases around the transition might come from pinning or demagnetization effect due to the shape of the sample.

Changes in the symmetry of the FLL and its orientation with respect to the crystallographic axes can result from an anisotropy in either the Fermi surface or the superconducting energy gap. In some instances the structures of the FLL can be understood by considering non-local corrections to the London model [163, 164, 153, 165].

The 30° reorientation of the FLL reported here occurs in a field H_r of only

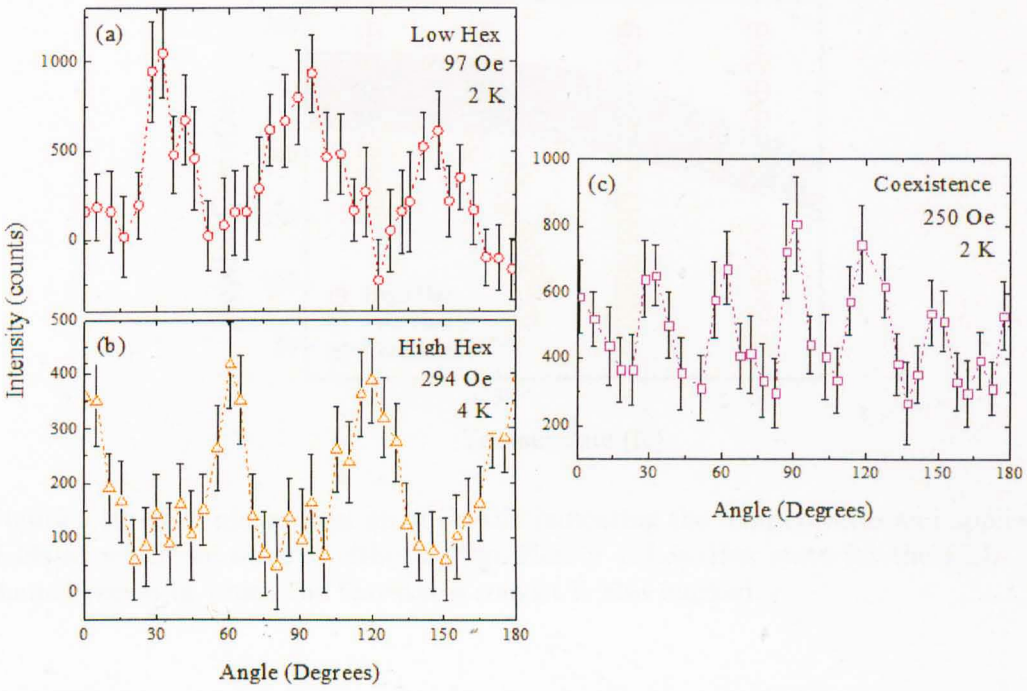

Figure 5.9: Intensity of the Bragg's peaks as a function of angle in the Low-Hex, High-Hex, and Coexistence phases of $6H$-CaAlSi between 0° to 180°.

200 Oe, a much lower field than for most FLL reorientations and a small fraction of the H_{c2} for this material, ($H_r/H_{c2} \approx 0.025$). In MgB_2, a 30° reorientation in the FLL has been associated with the suppression of the smaller of two superconducting gaps. However, H_r for MgB_2 is over 5000 Oe ($H_r/H_{c2} \approx 0.2$) and the reorientation process is second-order [161]. In some ways the FLL transition in CaAlSi more closely resembles the (apparently) first-order 45° reorientation between two rhombic FLL phases observed in Lu and Y borocarbide [164, 153, 166]. In these materials H_r is 250 and 1500 Oe for Lu and Y respectively ($H_r/H_{c2} \approx 0.02$) and the reorientation angle reflects the underlying symmetry of the lattice. In CaAlSi, however, we find no clear evidence for the changes in the apex angle β away from 60° seen in the borocarbides close to H_r.

Fig. 5.12 shows the form factor F at 2 K, extracted from the integrated intensity of the Bragg spots forming the FLL in CaAlSi. The form factor provides a measure of the amplitude of the field modulation inside a type-II superconductor due to the formation of a FLL [161].

According to the London model, for a conventional single band superconductor with a penetration depth and a coherence length that are independent of

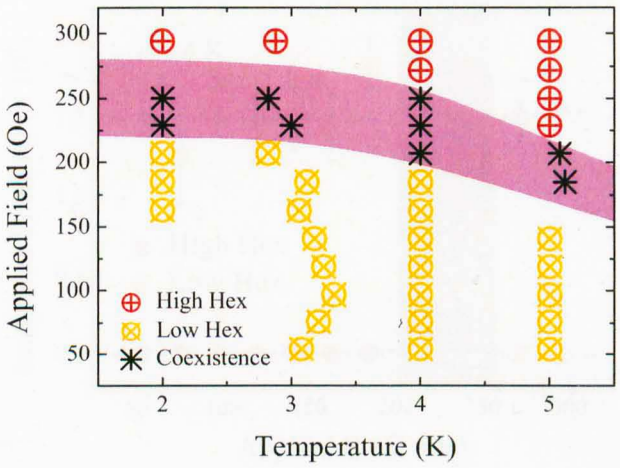

Figure 5.10: H-T phase diagram of CaAlSi indicating the temperatures and applied fields at which we observe either a High-Hex or a Low-Hex state for the FLL. A shaded region in which the two states coexist is also marked.

field, F decreases exponentially with field [167]. However, for an anisotropic superconductor, an expression for F has been calculated by Hao *et al.* [168] within the Ginzburg-Landau (GL) approximation.

$$F = \frac{3^{1/4}}{2\pi\sqrt{2}} \frac{\sqrt{\Phi_0 B} f^2 \xi_v}{\lambda^2} K_1 \left(\frac{2\pi\sqrt{2}}{3^{1/4}} \xi_v \sqrt{B/\Phi_0} \right) \tag{5.1}$$

with

$$\xi_v = \xi \left(\sqrt{2} - \frac{0.75}{\kappa} \right) \sqrt{(1+b^4)\left[1 - 2b(1-b)^2\right]}, \tag{5.2a}$$

$$f^2 = 1 - b^4, \tag{5.2b}$$

$K_n(x)$ is a modified Bessel function of n^{th} order, $\Phi_0 = 2.068 \times 10^{-15}$ Wb is the magnetic flux quantum, $\kappa = \lambda/\xi$ is the GL parameter, $B_{c2} = \Phi_0/(2\pi\xi^2)$ is the upper critical field, and $B = bB_{c2}$ is the applied field [84, 167]. The fit yields $\lambda = 1496(1)$ Å, $\xi = 307(1)$ Å, and $\kappa = 4.9(1)$. This κ is similar to the value of 5.2 reported by Imai *et al.* [160]. ξ is 50% larger than the value extracted from H_{c2} measurements on the same sample. In a study of MgB_2, the increase in the F at low field was attributed to a change in the superfluid density [161]. As shown here, such a conclusion is not required for CaAlSi.

The penetration depth anisotropy γ_λ, can be extracted by rotating the ap-

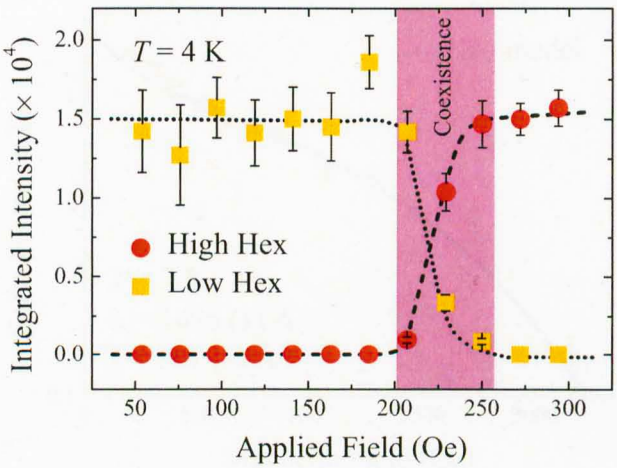

Figure 5.11: Standard monitor normalized intensity of the Bragg peaks for the High-Hex and Low-Hex phases of CaAlSi. The dotted and dashed lines are guides to the eye. The shading indicates the region in which the two FLL phases coexist.

plied magnetic field away from the c-axis and measuring the ratio of the major to minor axes of the ellipse (ϵ) connecting the Bragg peaks. Figs. 5.13(a)-(d) show the diffraction patterns of CaAlSi taken at 1.5 K in a field of 3 kOe applied at 10°, 28°, 47°, and 72° respectively to the c-axis. As the angle between the applied field and the c-axis increases, the diffraction pattern is distorted towards an elliptical shape, since the screening currents circulating around a vortex must cross the basal plane. Campbell *et al.* [169] studied the structure of a vortex lattice in anisotropic, uniaxial superconductors, for magnetic fields applied at an angle ψ to the principal axis. According to their model based on the London approach, ϵ is related to γ_λ in the following way,

$$\epsilon^2 = \frac{\gamma_\lambda^2}{\sin^2\psi + \gamma_\lambda^2 \cos^2\psi}. \tag{5.3}$$

Fig. 5.14 shows the variation of ϵ as a function of ψ for CaAlSi measured at 1.5 K in a field of 3 kOe. A fit to the data using Eq. 5.3 is indicated by the solid line yielding an anisotropy, $\gamma_\lambda = 2.7(1)$. The value of γ_λ is in excellent agreement with previous values of γ_ξ determined from magnetic and transport measurements [160, 132] and slightly larger than the value of 2 obtained by Kuroiwa *et al.* [162] from SANS measurements.

Close to T_c the anisotropic GL equations for a clean superconductor with an arbitrary gap anisotropy yield $\gamma_\lambda = \gamma_\xi$. At lower T, however, these two quanti-

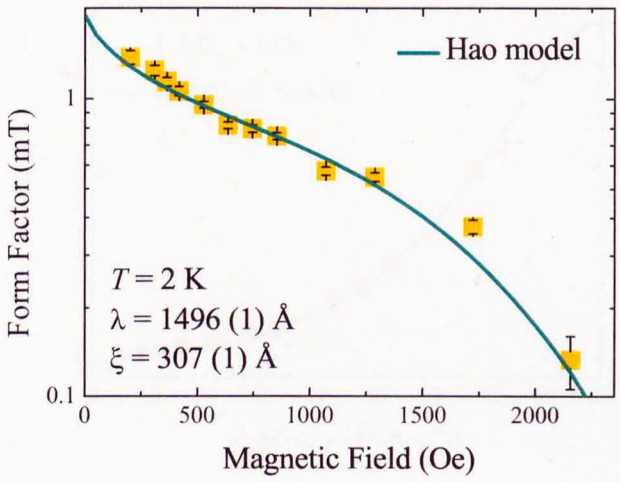

Figure 5.12: Form factor F of CaAlSi plotted on a log scale. The solid line is a fit to the data using the Hao model described in the text.

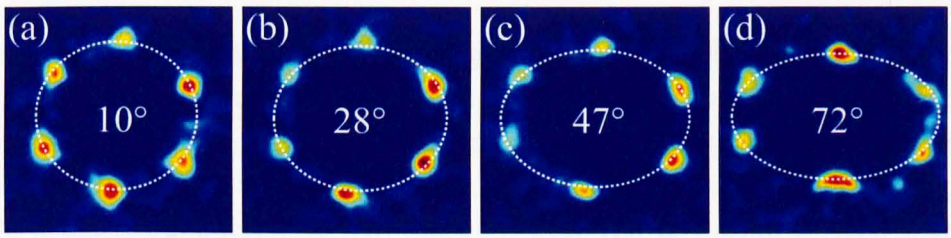

Figure 5.13: (a-d) Anisotropic FLL of CaAlSi at 1.5 K and a field of 3 kOe applied at 10°, 28°, 47°, and 72° respectively to the c-axis of the crystal.

ties may both depend on T and are not necessarily the same. For example, in the case of MgB_2 calculations for a weakly coupled two-band anisotropic superconductor showed that $\gamma_\lambda(T)$ and $\gamma_\xi(T)$ are an increasing and decreasing function of T respectively [170, 171]. In CaAlSi the equality of γ_λ and γ_ξ at 1.5 K may reflect the fact that the morphology of the FLL is established at higher T, which then gets pinned as the T is reduced. Alternatively it may be indicative of a more isotropic character for the Fermi surface in this material.

5.7 Summary and Conclusions

We have successfully grown a large single crystal of CaAlSi by the Bridgman method. We have carried out a high resolution single crystal x-ray study and observed the

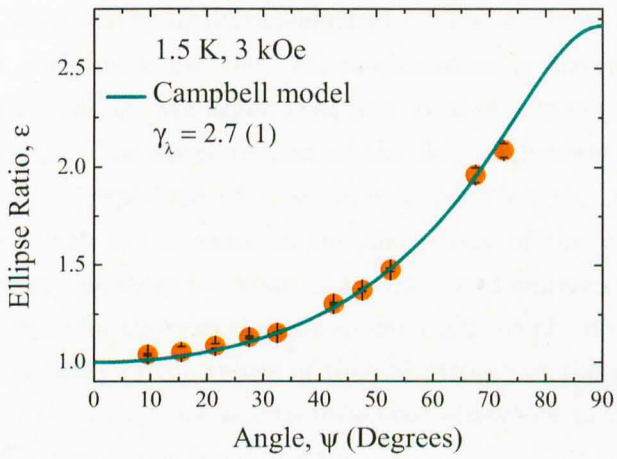

Figure 5.14: The ellipse ratio, ϵ as a function of angle, ψ at 1.5 K and applied field of 3 kOe for CaAlSi. The solid line is a fit to the data using the Campbell model which yields $\gamma_\lambda = 2.7(1)$ at $\psi = 90°$.

6 fold superlattice peaks present as a result of the $6H$ structure in the single crystal of CaAlSi. Magnetization and resistivity measurements have been performed to further verify the quality of our samples. Both magnetization and resistivity measurements confirm that our sample is superconducting below 7.7 K. Using the virgin magnetization data, we have calculated the H_{c1} of CaAlSi to 53.4(5) Oe at zero temperature.

We have performed a SANS study on a single crystal sample of CaAlSi. We observe a well-defined flux line lattice in a very low field of only 54 Oe. This in itself is noteworthy as this is one of the lowest fields in which a FLL has ever been imaged using the SANS technique and brings the technique closer to applied fields used in Bitter decoration experiments. In addition, it is interesting that a well defined FLL forms just above H_{c1} where the inter vortex distance is many times longer than the penetration depth. There have been suggestions that in this class of materials at lower fields ($\approx$ 1 Oe) an attractive inter vortex interaction will lead to a clustering of the vortices. While we acknowledge that we are well above this field regime, it is important to demonstrate that the dominant inter vortex interaction in this material at the low field regime is repulsive, leading to the formation of a symmetric hexagonal FLL.

We observe a hex-to-hex FLL reorientation at just 200 Oe. We have carefully considered what may drive the reorientation of the FLL. We cannot unequivocally state the source of the reorientation. We can, however, argue strongly in favour of

the reorientation being driven by non-local effects. This contrasts with the situation in MgB_2 where it is claimed that the FLL reorientation is driven by the effects of two superconducting bands. We argue that non local effects may be ubiquitous in this class of materials. Our measurement of the field dependent form factor from the field distribution is explained by a single coherence length, and the anisotropy of this coherence length is the same as the anisotropy of the penetration depth. Both features are very unlikely to occur in a multi-band superconductor. This has important implications for those working to understand the physics of the AlB_2 class of materials. The equality of the values of the anisotropy for the penetration depth measured here and the coherence length measured elsewhere may hint at the fact that this is indeed a simple one band system.

Chapter 6

Coexistence of Type-I and Type-II Superconductivity in ZrB_{12}

6.1 Introduction

Superconductivity was discovered in the cubic hexaborides, MeB_6, and the dodecaborides, MeB_{12} by Matthias *et al.* in the late 1960's (Me = Sc, Y, Zr, La, Lu, Th) [172]. ZrB_{12} has a relatively high T_c ($\approx$ 6 K) among all the known dodecaborides. Superconductivity in these cluster boride compounds has been of interest because of the idea that large numbers of light atoms and hence high phonon frequencies, together with a strong electron-phonon interaction, might lead to a high transition temperature. This interest has been renewed with the discovery of superconductivity at 39 K in MgB_2 (see ref. [13]). Later, isotope measurements indicated that the superconductivity in ZrB_{12} may arise from the Zr sublattice, with the boron acting as a fairly inert background [173]. ZrB_{12} crystallizes in the fcc cubic structure of the UB_{12} type (space group $Fm\bar{3}m$, a = 0.74075 nm [174]), a rocksalt-type structure with the Zr on the Na and the B_{12} clusters on the Cl sites. The boron atoms form a B_{12} cubic octahedral unit. Figure 6.1 shows the crystallographic structure of ZrB_{12}.

There have been several models suggested to explain the superconducting properties of ZrB_{12} which range from a strong-coupling BCS model to a two band BCS model with different superconducting gaps [175, 176, 174]. Recent band-structure calculations concluded that the Fermi surface of ZrB_{12} is composed of one open and one closed sheet [177, 178]. The specific heat data at zero field shows

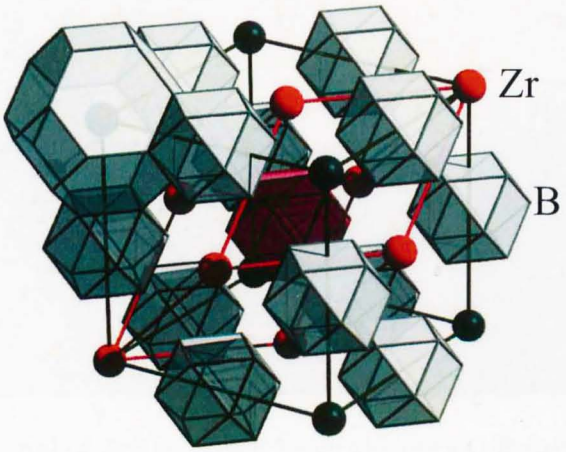

Figure 6.1: Crystallographic structure of ZrB_{12}. ZrB_{12} has a UB_{12} type face-centred cubic lattice structure. Each Zr atom (solid sphere) is surrounded by 24 B atoms arranged in a octahedral cluster.

a BCS-type superconducting transition at T_c. The specific heat jump changes from first-order (with a latent heat) to second-order (without a latent heat) with increasing magnetic field. It is also reported that the κ in this material lies close to the cross-over value of $1/\sqrt{2}$ between Type-I and Type-II superconductivity and that κ may change with temperature [179]. This motivated us to map out the complete B-T phase diagram of ZrB_{12}. This will help to clarify the debate as to whether ZrB_{12} is a Type-I or Type-II superconductor or has a more exotic nature in which both types of superconductivity coexist.

6.2 Single Crystal Growth of ZrB_{12}

Single crystals of ZrB_{12} were produced using the floating-zone technique in a Crystal Systems Incorporated (CSI) four-mirror infrared image furnace [see section 2.1.2]. The growths were performed in a flowing argon atmosphere of 2 bars. The seed rod was a polycrystalline rod of the same composition as the feed rod. Polycrystalline materials of ZrB_{12} (commercially available) were made into rods by compacting the powder in a waterproof balloon before compressing the rod isostatically by submerging it in water and applying high pressure ($\geq$ 150 kg cm^{-2}). The polycrystalline rod was sintered for 12 hr at 1400^{o}C to densify the materials to make it less likely to crumble upon handling and also to stabilize the molten zone during crystal growth. Growth speeds of 6-8 mm/h and a rotation rate of 25-30 rpm were used for both

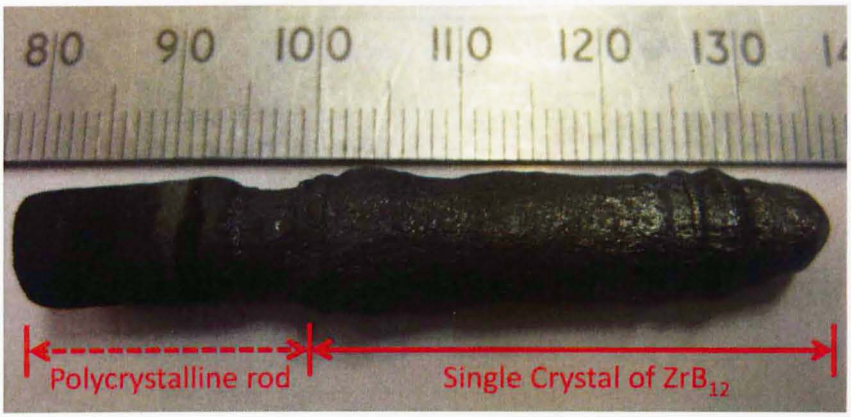

Figure 6.2: Single crystal of ZrB_{12}, grown using the optical floating zone method in a four mirror image furnace.

the feed and seed rods. Figure. 6.2 shows a single crystal of ZrB_{12} grown using this method. Crystal quality and orientation were determined using the X-ray Laue technique [for more details, see section 2.2.2]. Figure. 6.3 show the X-ray Laue images of a single crystal of ZrB_{12} collected along the [100] (a-axis) and [110] direction of the crystal.

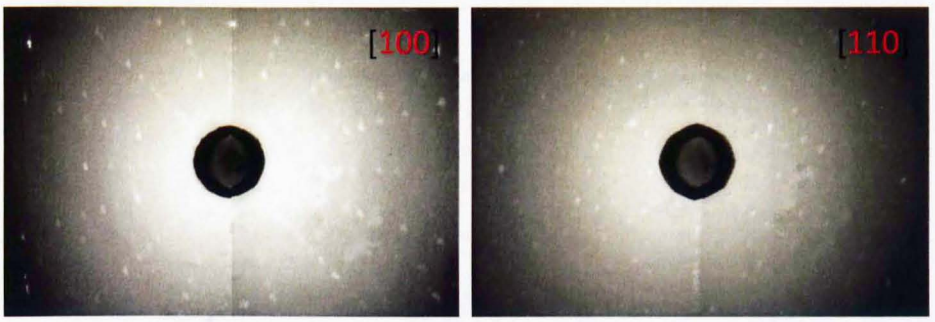

Figure 6.3: Typical X-ray Laue back-reflection image obtained from a crystal of ZrB_{12}. The image in the left is taken with the X-rays directed parallel to [100] (along the a-axis). The image on the right is taken along the [110] direction.

6.3 Magnetization Measurements of ZrB_{12}

The temperature dependence of the magnetic susceptibility of ZrB_{12} was measured using a *Quantum Design* MPMS magnetometer [see section 2.3.1]. A field of 10 Oe was applied both parallel and perpendicular to the c-axis. Data were taken both in

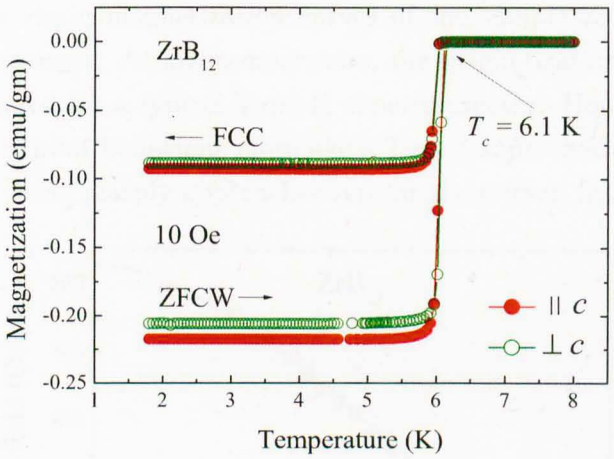

Figure 6.4: The temperature dependence of the dc magnetic susceptibility of ZrB_{12} measured using both zero-field-cooled warming (ZFCW) and field-cooled cooling (FCC). The magnetic field was applied both in parallel and perpendicular to the c-axis. The diamagnetic susceptibility shows a T_c onset of (6.10 ± 0.05) K.

the zero-field-cooled warming (ZFCW) and the field-cooled cooling (FCC) modes. The temperature dependence of the diamagnetic susceptibility shows that ZrB_{12} has nearly the same signal strength [see Fig. 6.4] for both directions of the applied field.

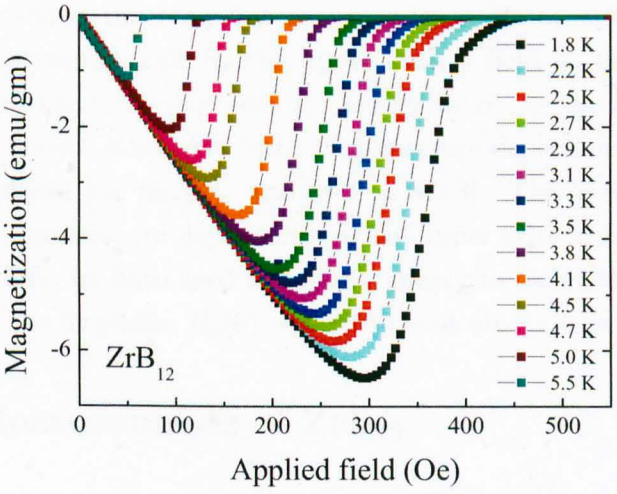

Figure 6.5: Virgin magnetization curves of the sample ZrB_{12} taken at different fixed temperatures.

Magnetization measurements were performed as a function of field. Fig-

ure 6.5 shows the virgin magnetization curves of the sample ZrB_{12} taken at different fixed temperatures. At low temperature, the magnetization approaches zero smoothly, as expected for a typical Type-II superconductor. However, close to T_c, the $M(H)$ curves exhibit behaviour more like a Type-I superconductor as the magnetization (5.5 K data) sharply approaches zero at the critical field.

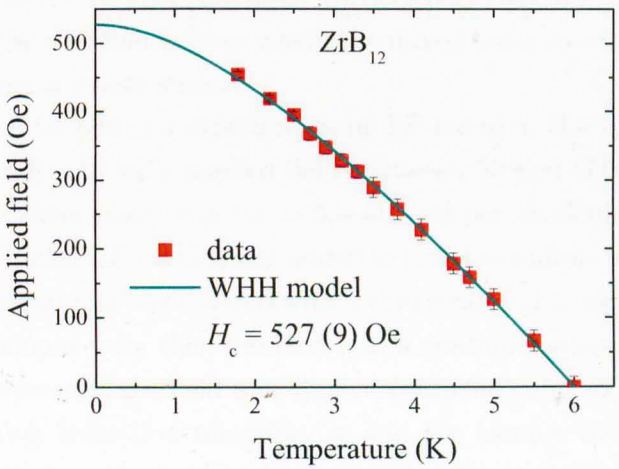

Figure 6.6: The temperature dependence of the critical field, H_c of ZrB_{12}, estimated from the $M(H)$ data.

Figure 6.6 shows the temperature dependence of the critical field, H_c of ZrB_{12}. We can not simply call H_c the upper critical field as the $M(H)$ data of ZrB_{12} shows Type-I like behaviour near T_c. We define H_c, as the field at which the sample enters the normal state. We fit the temperature dependence of the H_c data using the WHH model [for details, read section 3.3.3]. The WHH model is only applicable for the temperature dependence of the upper critical field for a Type-II superconductor. Here, we have used this model simply to estimate the H_c of ZrB_{12} at absolute zero. The fit yields, $H_c(0) = 527(9)$ Oe at absolute zero.

6.4 μSR Measurements of ZrB_{12}

In order to determine whether ZrB_{12} is a Type-I or Type-II superconductor, it is very important to understand the internal field distribution in the superconducting state. To probe the field distribution in the superconducting state of ZrB_{12} we have performed μSR experiments on the MuSR spectrometer of the ISIS pulsed muon facility. For more details of this technique, see section 2.4.

Here, we report transverse-field (TF) μSR experiments on a single crystal of

superconducting ZrB_{12} and construct a complete superconducting phase diagram. Our results clearly show a region of the B-T phase diagram of ZrB_{12} in which the sample is in a Meissner state. In this region, the superconductor behaves as an ideal diamagnet. We observe a region of intermediate state, a characteristic feature of Type-I superconductor (with a sizable demagnetization factor) [180] and a region of the mixed state with Abrikosov vortices [16], that are typical of a Type-II superconductor. We also find regions where the mixed state coexists with either the Meissner or the intermediate state.

We have performed the experiments in TF mode in the temperature range between 1.4 and 8 K and with applied fields between 50 and 600 Oe. The sample was mounted on a silver plate with the c-axis aligned perpendicular to the plate. A small amount of diluted GE varnish was added to glue the sample to the holder. The outer surface of the sample was covered with a thin silver foil to aid thermal contact. The sample and mount were then inserted into a continuous-flow helium cryostat. For all the measurements, the field was applied (perpendicular to the c-axis) above the superconducting transition temperature and the sample then cooled to base temperature. To analyze the data we have used the standard TF-μSR time spectra to observe the local field distribution in the superconducting state of ZrB_{12}. We have also used the field spectra which are extracted from the TF-μSR spectra using the maximum entropy technique. This is a deconvolution algorithm which functions by minimizing a smoothness function (entropy) of a system. This method picks the configuration with the highest entropy from all the probability distributions compatible with the empirical data. For more details on how the maximum entropy data is converted from the TF-μSR spectra, see Ref. [181].

The left hand panels of Figs. 6.7 and 6.8 show the time dependence of the muon spin rotation spectra below and above the superconducting transition temperature and in different applied fields. The solid lines are the fits to the data using the function:

$$\begin{aligned} G_X(t) = A_{KT}\left[1/3 + 2/3(1-\sigma_{KT}^2 t^2)\exp(-\sigma_{KT}^2 t^2/2)\right]\exp(-\lambda t) \\ + \sum_{i=M,Mx,Int} A_i \exp(-\sigma_i^2 t^2/2)\cos(\omega_i t + \phi) \\ + A_{Bg}\cos(\omega_{Bg} t + \phi), \end{aligned} \tag{6.1}$$

where A is the asymmetry, σ is the relaxation rate, and ω is the frequency of the muon spin precession signal of the respective components. The first term in the parentheses describes the static or quasi-static magnetic signal due to the neigh-

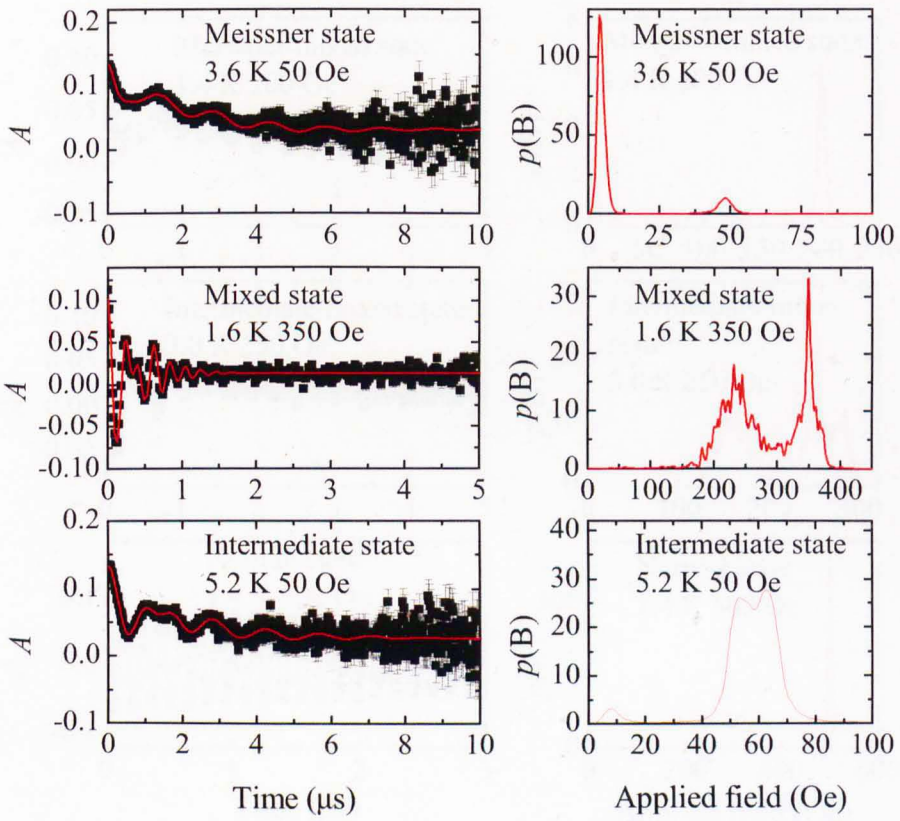

Figure 6.7: Muon spin rotation signals and the fitted parameters. The left hand panels show the time-dependent transverse-field μSR spectra, measured at different applied fields and temperatures. The right hand panels show the maximum entropy spectra of the corresponding muon spin rotation signals shown in the left panels.

bouring nuclear dipoles of Zr atoms which are randomly orientated with respect to each other and is also called the Kubo-Toyabe relaxation function [182]. Nuclear dipoles create a magnetic moment depending on the spin of the individual nucleons (i.e., protons and neutrons), which is a fundamental property of the nucleus. For Zr atoms, the nuclear magnetic dipole moment, $\mu = -1.5424(1)\ \mu_N$, where μ_N is the nuclear magneton [183]. The summation in the middle of Eq. 6.1 consists of Meissner (M), mixed (Mx) and intermediate (Int) state components. The third term represents the background signal which is mainly due to the applied field in the exposed sample holder and the cryostat walls.

Figure 6.9 shows the temperature dependence of the initial asymmetry data for the Meissner, mixed, intermediate, and normal states at different applied fields.

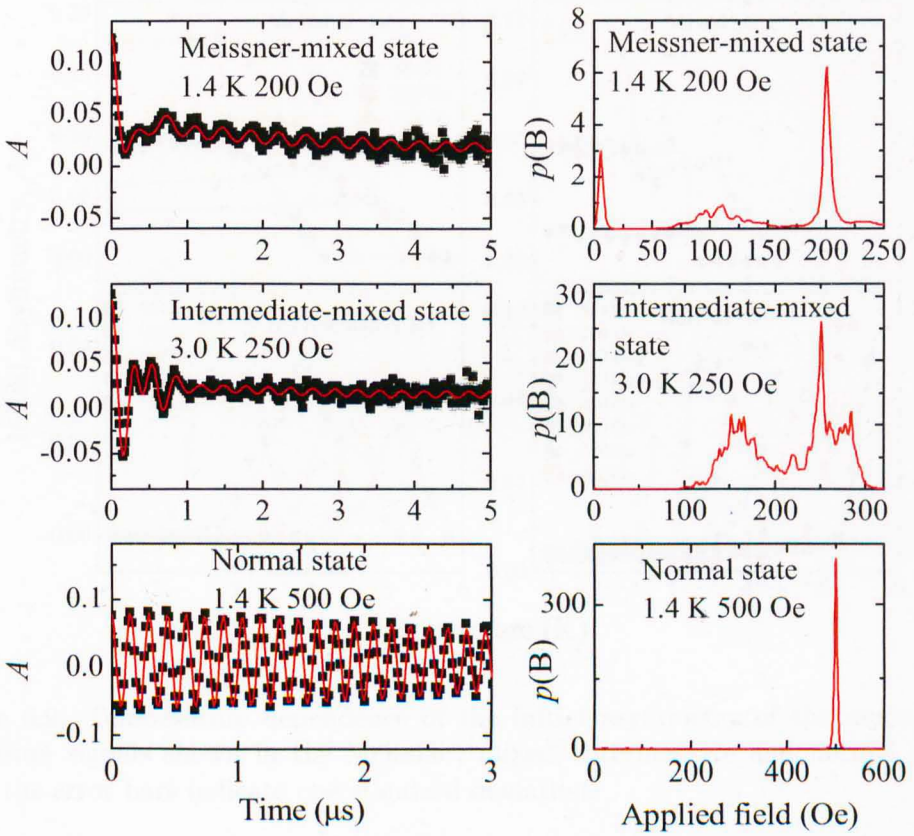

Figure 6.8: Muon spin rotation signals and the fitted parameters. The left hand panels are the time-dependent transverse-field μSR spectra, measured at different applied fields and temperatures. The right hand panels are the maximum entropy spectra of the corresponding muon spin rotation signals shown in the left panels.

The asymmetry data quantitatively describes the presence of different superconducting states with temperature. Solid lines are guides to the eye. In all cases, regimes of the different superconducting states tend towards lower temperature as the field increases. Figure 6.10 summarizes our data in a complete B-T phase diagram.

Let us now discuss this data in a little more detail. At 3.6 K and 50 Oe, the sample shows a Meissner state where the magnetic field is completely excluded from the sample. In the time spectra data (see the upper left panel of Fig. 6.7), we find a oscillatory signal with a frequency of 0.673 MHz. The muon precession frequency is related to the local field strength by

$$f = \frac{\gamma_\mu}{2\pi} B, \tag{6.2}$$

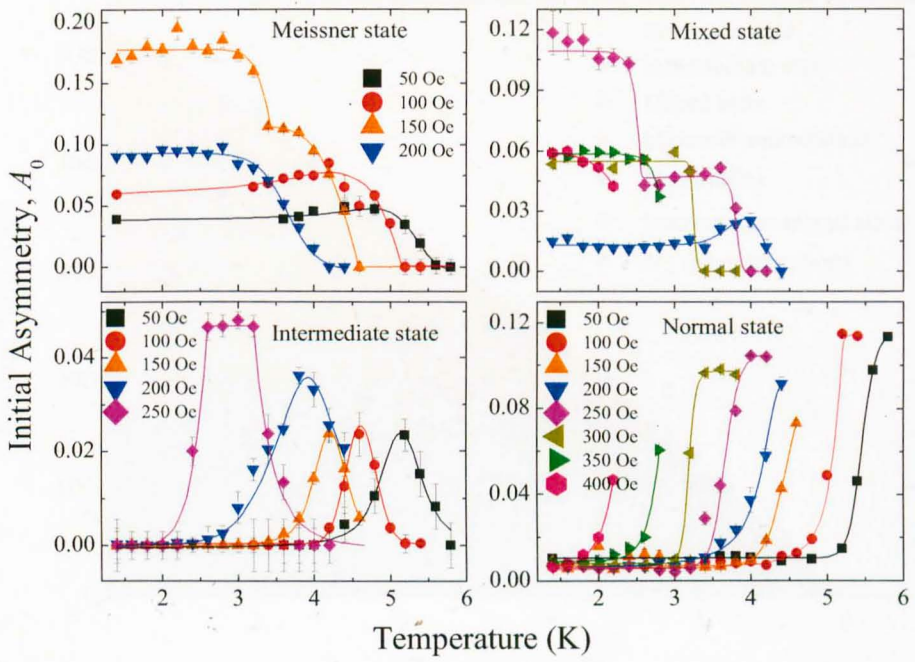

Figure 6.9: Temperature dependence of the initial asymmetry of the muon spin precession signals shown in the Meissner, mixed, intermediate and normal state. Here, the error bars indicate one standard deviation.

where $\gamma_\mu/2\pi = 135.5$ MHz/T is the muon gyromagnetic ratio. This implies that a frequency of 0.673 MHz corresponds to the magnetic field of 50 Oe. A relaxation signal with a field of 50 Oe can be explained by the fact that a fraction of the muons hit the sample holder and only see the applied field giving a background signal. The time spectra also has an additional relaxation signal which is probably due to the random nuclear dipole moments of the Zr atoms and can be fitted using the Kubo-Toyabe relaxation function. In the maximum entropy data (see the upper right panel of Fig. 6.7), we observe a peak at very low field which shows the Kubo-Toyabe behaviour associated with the nuclear field. We also see a small fraction of the applied field as an additional peak in the data due to some of the muons stopping in the sample holder and the cryostat's wall. In the B-T phase diagram [see Fig. 6.10], this Meissner state is shown by the yellow circles.

The signal at 1.6 K and 350 Oe (Fig. 6.7 middle panel) decays very quickly due to the inhomogeneous field distribution from the flux line lattice (FLL). Time spectra data have two frequencies of 4.776 and 3.205 MHz corresponding to magnetic fields of 350 and 236 Oe, respectively. Here again, the high frequency signal

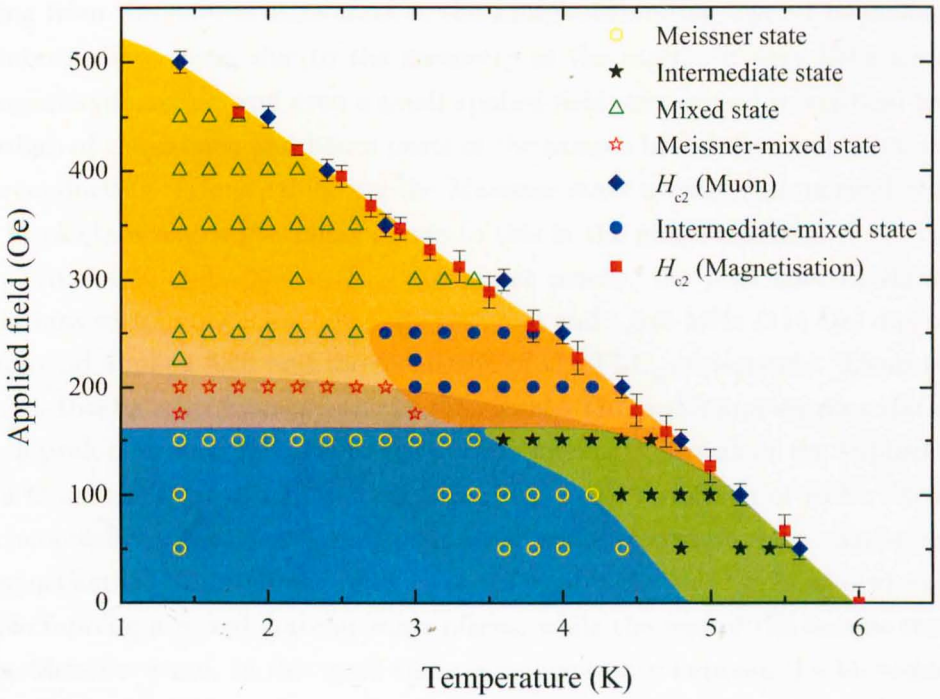

Figure 6.10: Superconducting phase diagram determined from muon spin rotation measurements on ZrB_{12}. The yellow circles, black stars, and green open-triangles indicate the Meissner, intermediate, and mixed states, respectively. The red open-stars and blue circle designate the coexistence of the mixed state separately with the Meissner and intermediate states, respectively. The royal-blue diamonds and red squares are the upper critical fields determined from muon spin rotation and magnetization measurements, respectively. The error bars indicate one standard deviation.

(4.776 MHz) is the background signal coming from the applied field, whereas the other signal with a frequency of 3.205 MHz is due to the formation of the FLL in the mixed state. In the maximum entropy data, a Gaussian distribution of fields due to the FLL is observed below the applied field and this indicates that the sample is in the mixed state of a Type-II superconductor. This data point is shown in the phase diagram by one of the green triangles.

The μSR spectra at 5.2 K and 50 Oe (Fig. 6.7 bottom panel) clearly reveal the presence of two oscillatory terms (with frequencies of 0.702 and 1.058 MHz) along with the Kubo-Toyabe term for the nuclear moments at very low field. The maximum entropy data show three peaks in the internal field distribution. The first and the second peaks are due to the nuclear moment and small background applied field, respectively, while the third peak can be described as a critical field

coming from the intermediate state of the sample exhibiting Type-I behaviour. In the intermediate state, due to the geometry of the sample it may have a sizable demagnetisation effect and even a small applied field may exceed the critical field at the edges of the sample and hence parts of the sample become normal. As a result, superconducting regions exhibiting the Meissner state coexist with normal regions. The black stars represent similar points to this in the phase diagram.

At 1.4 K and 200 Oe (Fig. 6.8 upper panel), the μSR spectra show two oscillations with frequencies 2.64 MHz (195 Oe) and 1.545 MHz (114 Oe) due to the background applied field and the formation of the FLL, respectively. There is also a Kubo-Toyabe relaxation present in the signal. The maximum entropy data also show a peak near zero field due to the nuclear moments, a peak at the applied field, and a Gaussian Type distribution of fields due to the formation of FLL. These are the characteristic signals of both the Meissner and mixed state. Here, again, due to demagnetisation effects, the applied field can exceed the lower critical field and the sample forming a mixed state at some places, while the rest of the sample remains in the Meissner state. In this state there is a coexistence between the Meissner and the mixed state. This region is shown in the phase diagram by the red stars. At 3.0 K and 250 Oe (Fig. 6.8 middle panel), another coexistence region is observed between the intermediate and the mixed states where we see structures typical of a FLL and the characteristic feature of the intermediate state. In the phase diagram, this region is shown by the blue spheres. Finally, at 1.4 K and 500 Oe (Fig. 6.8 lower panel), the sample is clearly in the normal state and we see a single oscillation (with frequency 6.769 MHz) corresponding to the applied field of 500 Oe which decays very slowly. The maximum entropy data also shows a single peak at the applied field. The normal state data are shown in the B-T phase diagram by the blue diamonds.

6.5 Summary and Conclusions

We have grown a high quality single crystal of ZrB_{12} using the optical floating zone method. The quality of the crystal was confirmed from Laue X-ray diffraction images. The temperature dependence of the magnetization measurements show a sharp T_c of 6.1 K for ZrB_{12}. The temperature dependence of H_c has been extracted from the virgin magnetization loops measured at different temperatures. The value of $H_c(T)$ at absolute zero can be estimated using the WHH model. The fit yields a value of 527(9) Oe for $H_c(0)$. We have mapped out the superconducting phase diagram of ZrB_{12} in great detail from the μSR measurements. By measuring the local field distribution for different applied fields and temperatures we have found evi-

dence of the Meissner, mixed, and intermediate states in the ZrB_{12} superconductor. The intermediate state is characteristic of a Type-I superconductor, while the mixed state is characteristic of a Type-II superconductor. We have also observed regions of coexistence between different states. Observation of an intermediate mixed state in a low-κ and Type-II superconductor has been reported by Essmann and Träuble using the decoration technique [184], while our system shows direct evidence of such a state. This observed phase diagram for superconductivity is unusual and implies that κ may change with temperature (or at least is close to the Type-I / Type-II boundary) since different regions of the phase diagram are characteristic of Type-I and Type-II behaviour. More studies (such as SANS, etc.) are required to verify our claim and also to understand the B-T phase diagram of ZrB_{12} in more detail. In addition, at low fields an attractive interaction between vortices may also be playing a role, as has been suggested for the "Type-1.5" description of MgB_2 (see ref. [20]) where one band is thought to have Type-I character while the other retains its Type-II nature. ZrB_{12} may be the ideal system to test such propositions.

Chapter 7

Crystallographic Structure and Superconductivity of Two Different Phases of Re_3W

7.1 Superconductivity with Non-centrosymmetric Crystal Structure

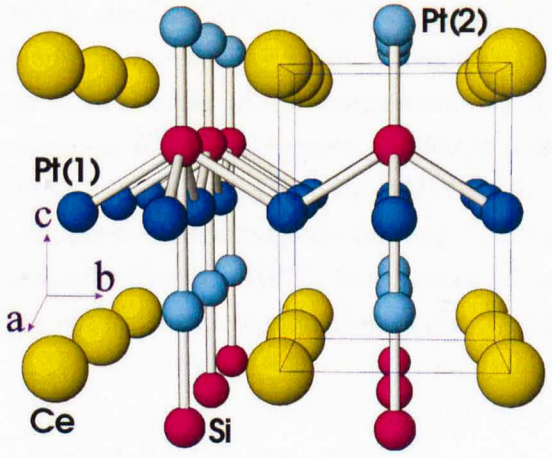

Figure 7.1: Crystal structure of $CePt_3Si$. The bonds indicate the pyramidal coordination $[Pt_5]Si$ around the Si atom.

The discovery of superconductivity in the non-centrosymmetric (NCS) heavy fermion $CePt_3Si$ [185] has resulted in a period of intense theoretical and experimen-

tal investigation into the physics of non-centrosymmetric superconducting materials. The symmetry of a crystal structure plays an important role in the formation of Cooper pairs in conventional superconductors. The term "non-centrosymmetric" indicates that the crystal lattice lacks inversion symmetry. The concept of symmetry describes the periodic repetition of structural features. If a crystal possesses inversion symmetry, then every line drawn through the centre of the crystal will connect two identical features on opposite sides of the crystal. For example, $CePt_3Si$ crystallizes in a tetragonal crystal structure with the space group *P4mm* (No. 99) which lacks inversion symmetry [185]. The unit cell contains one formula unit with one Ce, one Si and two Pt inequivalent sites. The absence of inversion symmetry comes from the missing mirror plane (0, 0, 1/2)(see Fig. 7.1). The absence of such a crystallographic inversion centre can degenerate the underlying spin-up and spin-down energy bands. Theoretically, the lack of inversion symmetry leads to an anti-symmetric spin orbit coupling which removes the spin degeneracy of the conduction band electrons and therefore in noncentrosymmetric superconductors the spin and the orbital parts of the Cooper pairs cannot be treated independently [186, 187, 188, 189]. The lack of inversion symmetry in the crystal structure of this type of material along with strong spin-orbit (SO) coupling can lead to a mixing of spin-singlet and spin-triplet pair states [186]. These NCS materials exhibit unusual magnetic properties including suppressed paramagnetic limiting or high upper critical fields [188, 190] as seen in $CePt_3Si$, [185] $CeRhSi_3$, [191] and $CeIrSi_3$ [192], the appearance of superconductivity with antiferromagnetic order in $CePt_3Si$, [193], and superconductivity at the border of ferromagnetism in UIr [194]. Novel physics has indeed been observed in many NCS superconductors such as the large upper critical field (Y_2C_3, [195] $CePt_3Si$, [185] $CeRhSi_3$, [191] $CeIrSi_3$, [192] $CeCoGe_3$, [196] $CeIrGe_3$, [195] etc.), suppressed paramagnetic limiting ($CePt_3Si$, [188, 190]), time-reversal symmetry breaking ($LaNiC_2$ [197]), coexistence of ferromagnetic or antiferromagnetic ordering with the superconducting phase ($CePt_3Si$, [193] UIr, [194]) are expected.

7.2 Superconductivity in Re_3W

One recent focus of the work on non-centrosymmetric superconductors has been to investigate the properties of transition-metal compounds that have significant spin-orbit coupling. Here, the complications of the f-electron heavy fermions, such as the strong electron correlations and the possibility of magnetically mediated superconductivity, are expected to be absent. The intermetallic Re_3W belongs in this

category as it contains very heavy atoms with atomic numbers 75 and 74 for Re and W respectively. Superconductivity in Re_3W was first reported in the 1960s. The material was shown to have an α-Mn or A12 structure [198, 199], although it is worth noting that the authors of this early work did not comment on the fact that the α-Mn structure is non-centrosymmetric. Since then, very little experimental work has been done on Re_3W. Recent penetration depth measurements carried out on the NCS phase of Re_3W by RF tunnel diode resonator and point-contact spectroscopy suggested that Re_3W is a weakly coupled isotropic s-wave superconductor [200, 201, 202].

Here, we report on the synthesis of two different superconducting phases of Re_3W. One phase has a centrosymmetric (CS) crystal structure, whereas the other has a non-centrosymmetric structure. Switching from the CS to the NCS phase is achieved by annealing the sample, while remelting the NCS sample in an arc furnace returns the sample to the CS structure. The ease with which one can switch between the two phases of Re_3W has allowed us to investigate and compare the properties of a CS and a NCS superconducting system using a single material without changing in stoichiometry. We characterize the properties of both phases of Re_3W using neutron diffraction, magnetization, M, and resistivity, ρ, measurements. We present the temperature dependence of the lower critical field, H_{c1}, and the upper critical field, H_{c2}, of both materials and also calculate the penetration depths and coherence lengths for these systems.

We have also performed muon spin relaxation/rotation (μSR) experiments on the NCS and the CS phases of Re_3W. μSR can be used to detect small internal magnetic fields associated with the onset of an unconventional superconducting state [203, 204, 197] and to measure the temperature and field dependence of the London magnetic penetration depth, λ, in the vortex state of type-II superconductors. [47, 205] The temperature and field dependence of λ can in turn provide detailed information on the nature of the superconducting gap.

7.3 Sample Preparation of the CS and NCS Phases of Re_3W

Samples of the as-cast phase of Re_3W were prepared by melting together a stoichiometric mixture of Re lumps (99.99%) and W pieces (99.999%) in an arc furnace [for details, see section 2.1.1] on a water-cooled copper hearth using tungsten electrodes in a high-purity Ar atmosphere. After the initial melt, the sample buttons were turned and remelted several times to ensure homogenity. The as-grown samples

were annealed for 5 days at 1500°C in a high-purity Ar atmosphere. The unannealed samples of Re_3W are hard but malleable. The samples become brittle after annealing.

7.4 Powder Neutron Diffraction Studies of the CS and NCS Phases of Re_3W

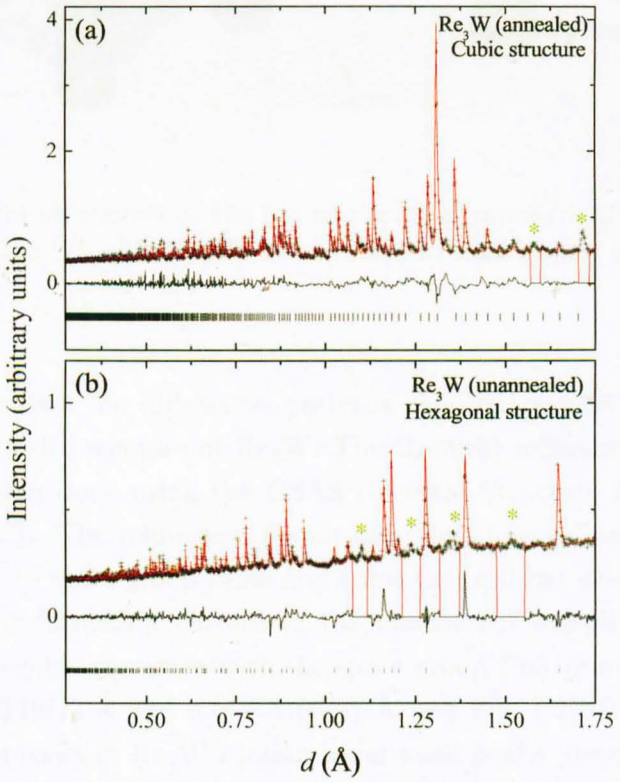

Figure 7.2: Neutron diffraction patterns as a function of d-spacing collected at 295 K for the (a) annealed and (b) unannealed samples of Re_3W. The Rietveld refinement of the diffraction data shows the annealed sample has a non-centrosymmetric α-Mn structure while the unannealed sample has a centrosymmetric hexagonal structure. Green asterisks are the peaks that can not be indexed. All the refined crystal parameters are shown in Table 7.1.

Powder neutron diffraction experiments were carried out on the GEM diffractometer at the ISIS Facility, Rutherford Appleton Laboratory, UK. For more details, read section 2.5.1. The data were normalized to the incident neutron flux distribution, corrected for detector efficiencies, and converted into d-spacing pat-

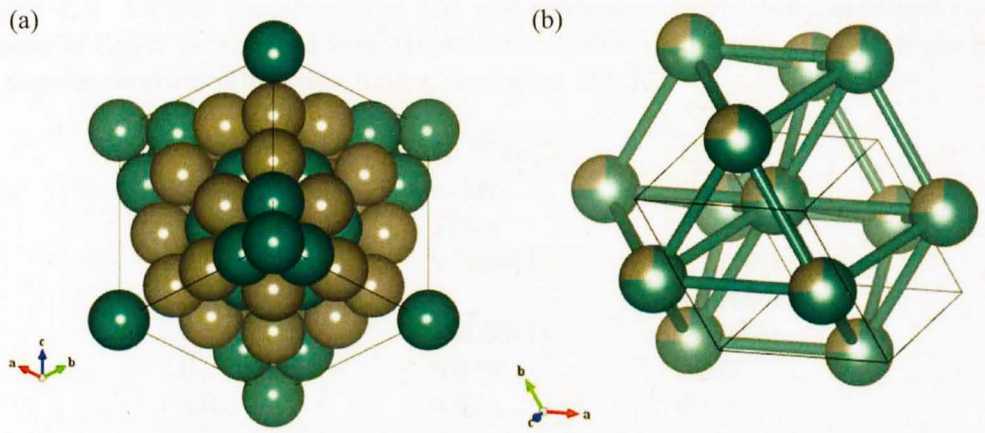

Figure 7.3: Crystal structures of the (a) non-centrosymmetric and (b) centrosymmetric phases of Re_3W, with the Re atoms shown in dark cyan and the W atoms shown in grey.

terns. Fig. 7.2 shows the diffraction patterns collected at 295 K from the annealed and unannealed samples of Re_3W. The Rietveld refinement of the diffraction data have been done using the GSAS (General Structure Analysis System) program [206, 207]. The refinement shows that the annealed sample has a NCS α-Mn structure with space group $I\bar{4}3m$ and cubic unit cell size $a = 9.5986(1)$ Å (see Fig. 7.2(a)). The diffraction pattern of the unannealed sample shows that this sample has a hexagonal structure with the space group $P63/mmm$ and lattice parameters $a = 2.7719(1)$ Å and $c = 4.5166(1)$ Å (see Fig. 7.2(b)). The diffraction patterns of both phases of Re_3W contain some weak peaks (denoted by asterisks) that can not be indexed. Figure. 7.3(a) and (b) show the crystal structures of the NCS and the CS phases of Re_3W. For the CS phase of Re_3W, both the Re and the W atoms share the same site leading to a random distribution of Re and W within the material. For the NCS phase, the refinement indicates that Re and the W atoms occupy preferred crystallographic sites and are therefore distributed in a more orderly fashion within the material. The refined composition of the NCS phase is $Re_{3.45}W$ indicating there is still some uncertainty in the site occupation. The ratio of the unit-cell volume for the NCS and CS phases of Re_3W is 25:1. Crystallographic parameters of the two phases of Re_3W, determined from the structural refinement of neutron diffraction data are shown in Tables 7.1 and 7.2.

Table 7.1: Lattice parameters of the non-centrosymmetric and centrosymmetric phases of Re_3W determined from the structural refinement using the GSAS program of powder neutron diffraction data collected at 295 K.

	NCS Re_3W	CS Re_3W
Structure	α-Mn	Hexagonal
Space group	$I\bar{4}3m$	$P63/mmm$
a (Å)	9.5986(1)	2.7719(1)
c (Å)		4.5166(1)
V_{cell} (Å^3)	884.35(1)	34.70(1)
R_p	0.049	0.077
wR_p	0.07	0.1

Table 7.2: Atomic position parameters of the non-centrosymmetric and centrosymmetric phases of Re_3W determined from the structural refinement using the GSAS program of powder neutron diffraction data collected at 295 K

NCS	Re_3W						
Atom	site	x	y	z	Mult	Occ.	U_{iso} (Å^2)
Re	2a	0	0	0	2	0.99	0.007
W	8c	0.3192	0.3192	0.3192	8	1.00	0.006
W	24g	0.3605	0.3605	0.0456	24	0.21	0.009
Re	24g	0.3605	0.3605	0.0456	24	0.79	0.009
Re	24g	0.0911	0.0911	0.2826	24	1.00	0.008
CS	Re_3W						
Atom		x	y	z	Mult	Occ.	U_{iso} (Å^2)
Re		0.3333	0.6667	0.25	2	0.75	0.005
W		0.3333	0.6667	0.25	2	0.25	0.005

7.5 Magnetization Measurements of the CS and NCS Phases of Re_3W

Magnetization versus temperature measurements were performed in an applied magnetic field of 20 Oe using a *Quantum Design* Magnetic Property Measurement System (MPMS) magnetometer, see section 2.3.1. The temperature dependence of the dc magnetic susceptibility, $\chi(T)$ shows that the NCS Re_3W sample has a superconducting transition temperature, T_c^{onset}, of (7.80 ± 0.05) K [see Fig. 7.4] with a transition width $\Delta T_c = 0.21$ K. For CS Re_3W, the onset of the transition is around

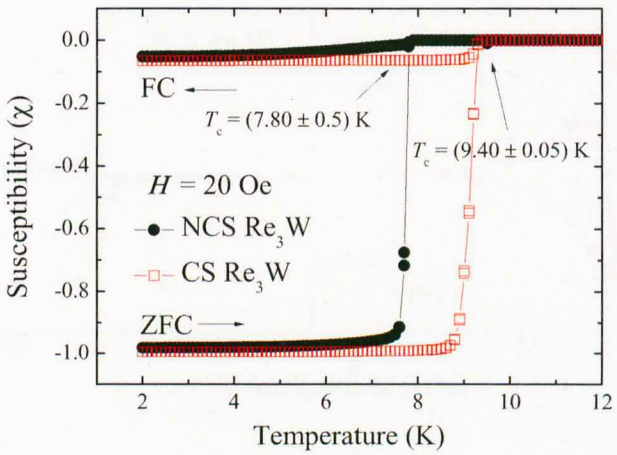

Figure 7.4: Temperature dependence of the magnetic susceptibility for the non-centrosymmetric and the centrosymmetric Re_3W measured in zero-field-cooled and field-cooled mode in an applied magnetic field of 20 Oe.

(9.40 ± 0.05) K with a much broader transition of ΔT_c = 0.50 K. Comparable transition widths are observed in the resistivity measurements (see below). This suggests, as expected, that the annealed NCS phase of Re_3W is more homogeneous than the unannealed CS phase. At 2 K, the zero-field-cooled (ZFC) dc susceptibility approaches a value of -1 ($\sim$ 100% shielding) for both the samples, while the field-cooled (FC) signal shows a flux exclusion (Meissner effect) of $\sim$ 5% for the NCS phase and $\sim$ 7% for the CS phase.

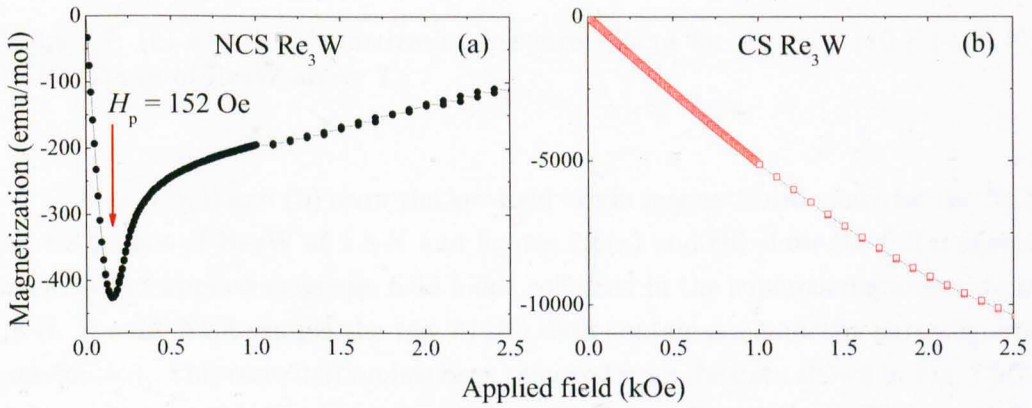

Figure 7.5: (a) and (b) Virgin magnetization curves measured at 1.8 K for the non-centrosymmetric and centrosymmetric phases of Re_3W.

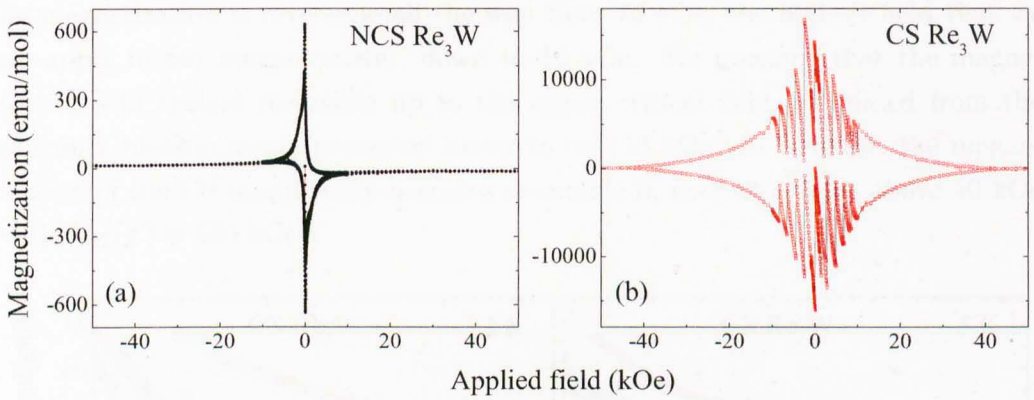

Figure 7.6: (a) and (b) Magnetization hysteresis loops at 1.8 K for the NCS and CS phases of Re_3W.

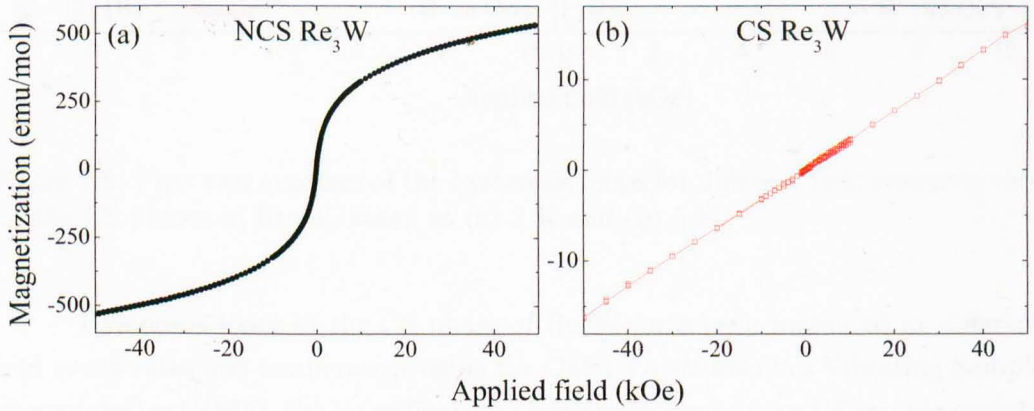

Figure 7.7: (a) and (b) Magnetization hysteresis loops for the NCS (10 K) and CS (12 K) phases of Re_3W above T_c.

Figs. 7.5(a) and (b) show the low-field virgin magnetization data for the NCS and CS phases of Re_3W at 1.8 K and figures 7.6(a) and (b) show the full magnetization versus applied magnetic field loops collected in the superconducting state at 1.8 K. For the NCS sample the raw $M(H)$ data contain a significant paramagnetic contribution. This contribution has been removed from the data shown in Fig. 7.6(a) by measuring an $M(H)$ curve above T_c at 10 K (see Fig. 7.7(a)). The signal for the CS sample contains a small linear susceptibility $\chi_{dc} = 4.23 \times 10^{-7}$ emu/g (see Fig. 7.7(b)) that has been subtracted from the data shown in figure 7.6(b). For the NCS sample, the value of the field of complete penetration of magnetic flux, H_p is 152 Oe while in the CS sample, $H_p > 2500$ Oe. For the NCS phase of Re_3W

the magnetization is reversible all the way from 70 kOe, the highest field that we can apply in our magnetometer, down to 10 kOe. We presume that the magnetization will remain reversible up to the upper critical field, estimated from the resistance measurements presented below to be 113 kOe. In contrast, the magnetization of the CS sample only becomes reversible in magnetic fields above 40 kOe (with $H_{c2}(T) \approx 130$ kOe).

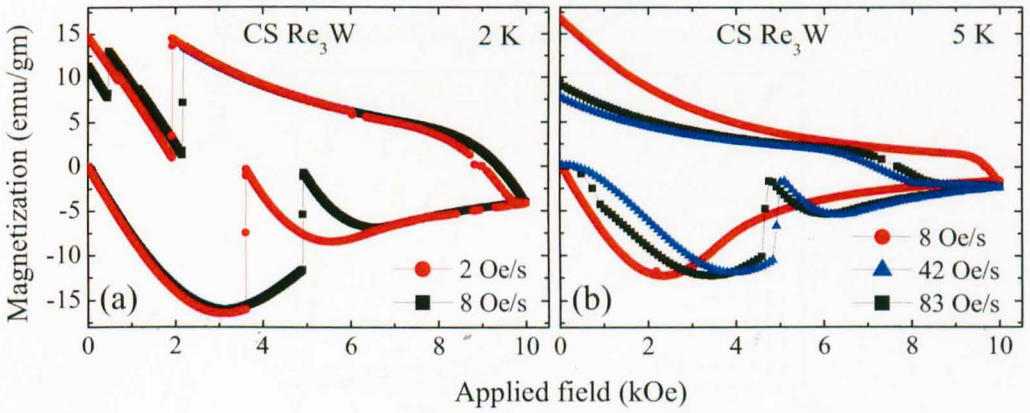

Figure 7.8: First two quarters of the hysteresis loops for different field sweeping rate for the CS phases of Re_3W, taken at (a) 2 K and (b) 5 K.

Hysteresis loops of the CS phase of Re_3W have been measured at different field sweep rates and temperature using the Oxford Instruments's Vibrating Sample Magnetometer (VSM). For lower fields the hysteresis loops of the CS sample contain a number of large magnetic-flux jumps, while no jumps are observed for the annealed samples. These flux jumps occur at lower temperatures ($T \leq 4$ K) and at applied fields below $\sim$ 20 kOe. The number and magnitude of the flux jumps vary from loop to loop and become less frequent as the field sweeping rate, dH/dt, is decreased [see Fig. 7.8(a)]. At 5 K with ($dH/dt \leq 10$ Oe/s) no flux jumps are observed and at higher temperatures (5 K $< T < T_c$) the flux jumps disappear [see Fig. 7.8(b)].

The $M(H)$ curves show that both types of Re_3W exhibit reversible behaviour below T_c over a large region of the H-T phase diagram. These data indicate that the bulk pinning is stronger in the CS phase of Re_3W than the NCS phase, and that the flux jumps are due to thermomagnetic instabilities induced by the motion of vortices into the superconductor combined with the sudden redistribution of the vortices within the sample [208]. The symmetry of the loops suggests that surface barriers do not play an important role in this material. Further studies are underway to investigate the different pinning mechanisms in the two different phases of Re_3W.

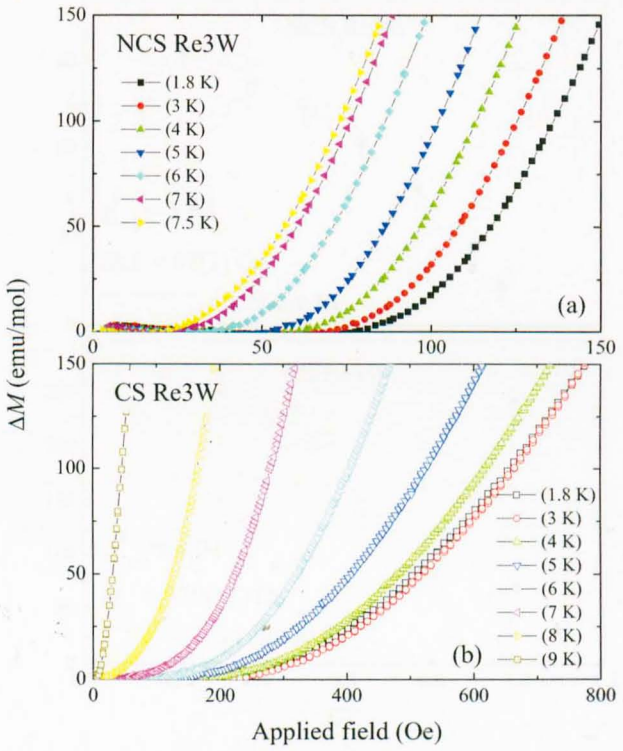

Figure 7.9: (a) and (b) Deviation, ΔM, from the linear virgin magnetization as a function of applied field determined at different temperatures for the NCS and CS phases of Re_3W.

The value of the lower critical field, H_{c1}, was determined by measuring the field of first deviation from the initial slope of the magnetization curve. To this end, a linear fit to the data between 0 to 10 Oe was made. The deviation from linearity, ΔM, was then calculated by subtracting this fit from the magnetization curves and plotted as a function of applied field [see Figs. 7.9 (a) and (b)]. The temperature dependence of H_{c1} for the two phases of Re_3W are obtained by using the criteria $\Delta M \leq 10^{-4}$ emu/g and plotted in Figs. 7.10 (a) and (b). Demagnetizing effects are taken into account while estimating the H_{c1} values from the magnetization data. The data for both the samples are fitted using the expression $H_{c1}(T) = H_{c1}(0)\left\{1-(T/T_c)^2\right\}$, where $H_{c1}(0)$ is the lower critical field at zero temperature. T_c was used as a variable parameter for better fitting. The quadratic equation fits the data well for the NCS phase, whereas the model provides a poor fit to the data of the CS phase. The fits yield $H_{c1}(0)$ of 97(1) and 279(11) Oe for the NCS and the CS samples respectively.

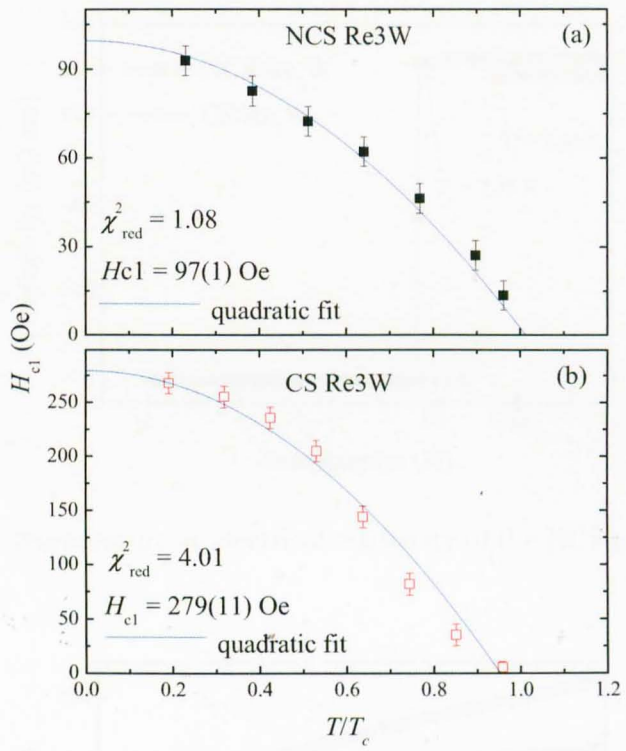

Figure 7.10: (a) and (b) H_{c1} as a function of temperature for the NCS and CS phases of Re_3W. The solid lines are fits to the data using the expression $H_{c1}(T) = H_{c1}(0)\{1 - (T/T_c)^2\}$.

7.6 Resistivity Measurements of the CS and NCS Phases of Re_3W

We have measured the ac electrical resistivity as a function of temperature, $\rho(T)$, for both phases of Re_3W via a standard four-probe method [see section 2.3.2] using a *Quantum Design* Physical Property Measurement System (PPMS) [see Fig. 7.11]. The NCS Re_3W shows a superconducting transition (onset) at (7.85 ± 0.05) K (ΔT_c = 0.05 K) while the CS Re_3W has a transition at (9.45 ± 0.05) K (ΔT_c = 0.32 K). The zero-field onset transition temperatures determined from the resistivity measurements are slightly higher than those obtained from the magnetization measurements performed in a magnetic field of 20 Oe. The resistivity curves between 2 to 295 K show metallic behaviour for the CS phase of Re_3W, whereas it is almost temperature independent above T_c in the NCS phase of Re_3W [see Fig. 7.12]. The relative resistance ratio, $\rho(295\ K)/\rho(10\ K)$ and the room temperature resistivity are 1.15(1) and 1.7$\mu\Omega$m for the NCS phase and 1.52(1) and 2.1$\mu\Omega$m for the CS phase

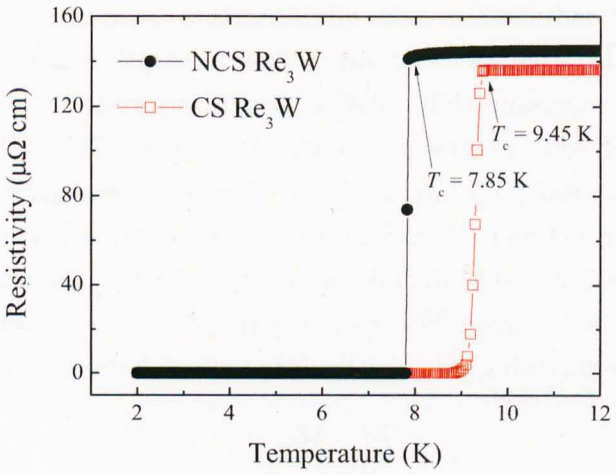

Figure 7.11: Low-temperature ac electrical resistivity of the NCS and the CS phases of Re_3W.

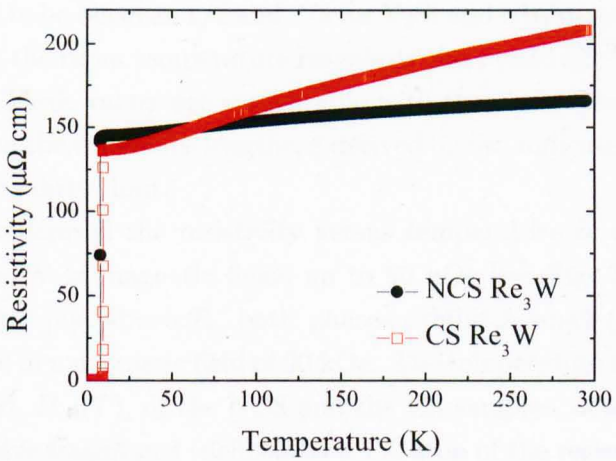

Figure 7.12: An ac electrical resistivity of the NCS and the CS phases of Re_3W up to room temperature.

indicating that both samples are poor metals. The NCS phase is the more brittle of the two materials and any extrinsic factors such as microscopic cracks in the sample are more likely to play a role in high normal state resistivity. Given that the room temperature resistivity of the NCS sample is lower than the CS phase, we suggest that cracks are not the reason for the high normal-state resistivity. The poor conductivity is more likely to result from a combination of strong electronic scattering and a large temperature independent residual resistivity due to structural disorder

(while the NCS annealed phase is structurally more ordered than the CS phase, the NCS phase still retains a degree of Re/W disorder). We have calculated the mean free path, l_{tr} based on the BCS approach [209]. The molecular weight of Re, W and, Re_3W are 186.2, 183.9 and, 742.5 g/mol, respectively. The density of Re_3W is 18.1 g/cm^3 (assuming same density for the NCS and CS phases of Re_3W). Hence, the molar volume, $V_M = 742.5/18.1 = 41.0$ cm^3/mol. The Fermi surface area for the free electron gas, $S_F = 4\pi(3\pi^2 n)^{2/3}$ where n is the free electron density and can be calculated as $n = \frac{1}{V_M} \times (3 \times 7 + 6) \times 6.023 \times 10^{23}$ e/cm^3. The mean free path of an electron can be calculated by these values using the following equation

$$l_{tr} = \frac{1.27 \times 10^4}{\rho n^{2/3}(S/S_F)}, \tag{7.1}$$

where S is the Fermi-surface area and S_F is the Fermi-surface area of the free electron gas of density n. S_F and n have been used in such a way so that the factor $n^{2/3}S/S_F$ appears proportional only to S. We assume $S/S_F = 1/2$ (value of S/S_F has been assumed to be between 1/2 and 2/3 for V_3Si and Nb_3Sn systems) [209]. The calculations using the room temperature resistivity data yield $l_{tr}^{NCS} = 0.277$ nm and $l_{tr}^{CS} = 0.224$ nm. These values are comparable with the size of the crystallographic unit cells and given the coherence lengths, ξ derived below, indicate that both phases of Re_3W are in the dirty limit.

We have measured the resistivity versus temperature of the NCS and the CS samples of Re_3W in magnetic fields up to 90 kOe [see Fig. 7.13 (a) and (b)]. In the normal state just above T_c, both phases exhibit a small ($\sim 0.6\%$) positive magnetoresistance in a magnetic field of 90 kOe. The temperature dependence of the upper critical field, $H_{c2}(T)$, of the NCS and the CS samples, determined from the onset of the resistive transitions (defined by a 1% drop of the resistivity), are shown in Fig. 7.14 (a) and (b). For the NCS sample, the temperature dependence of H_{c2} is nearly linear close to T_c with $dH_{c2}^{\rm NCS}/dT = -23.0(2)$ kOe/K and can be described using the Werthamer-Helfand-Hohenberg (WHH) model [see section 3.3.3]. In fitting the data to the WHH relations we calculated the Maki parameter, $\alpha = 1.41 \pm 0.01$, compared with a value of 1.22 ± 0.01 estimated from the gradient $dH_{c2}^{\rm NCS}/dT$ near T_c. The WHH fit yields $H_{c2}^{\rm NCS} = 125(1)$ kOe at $T = 0$ K. The temperature dependence of H_{c2} for the CS sample clearly shows a difference in behaviour compared to the NCS sample with deviations from the conventional WHH dependence. The data has a positive curvature with temperature near T_c and is linear thereafter. A similar behaviour is observed in polycrystalline borocarbides [210], MgB_2 [211, 212], and $Nb_{0.18}Re_{0.82}$ [213]. A reasonable fit to the data for the CS sample can be obtained

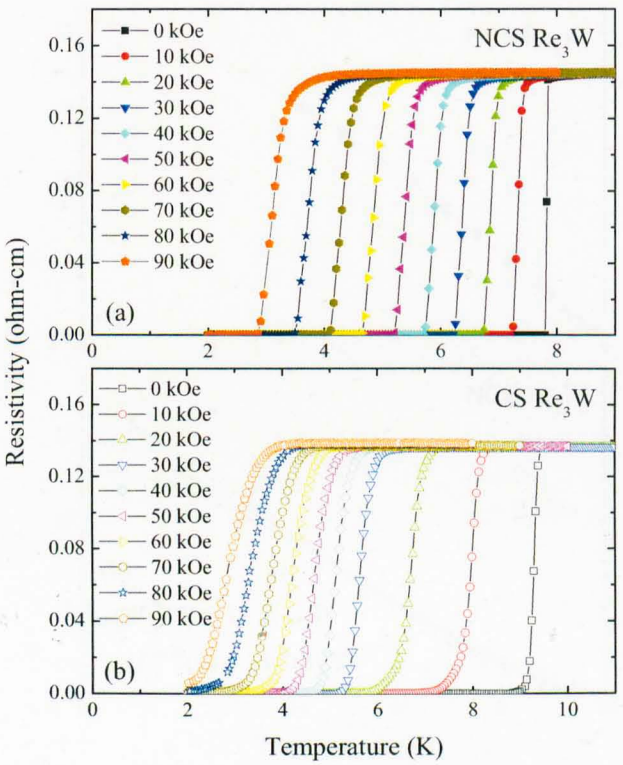

Figure 7.13: (a) and (b) Temperature variation of the resistivity in a set of magnetic fields from 0 to 90 kOe for the NCS and CS phases of Re_3W.

using the formula based on Ginzburg-Landau (GL) equation

$$H_{c2}(T) = H_{c2}(0)\frac{(1-t^2)}{(1+t^2)}. \tag{7.2}$$

Here $t = \frac{T}{T_c}$. The fit yields $H_{c2}^{CS}(0) = 129(4)$ kOe. A better fit to the data close to T_c can be obtained using the Boson equation [214].

$$H_{c2}(T) = H_{c2}(0)(1-t^{3/2})^{3/2}. \tag{7.3}$$

In this model is it assumed that the electron pairs beheave as hard-core charged bosons. This can exhibit a superconducting state analogous to that of superfluid ^{4}He. The fit the Boson expression yields $H_{c2}^{CS}(0) = 147(3)$ kOe. A simple linear extrapolation of the lower temperature data to $T = 0$ K (shown in dashed line in Fig. 7.14 (b)) gives $H_{c2}^{CS}(0) = 178(5)$ kOe with $dH_{c2}^{CS}/dT = -21(1)$ kOe/K. A similar analysis of the data for the NCS sample gives $H_{c2}^{NCS}(0) = 153(1)$ kOe. While the temperature dependence of H_{c2} for the two phases is clearly different, the values

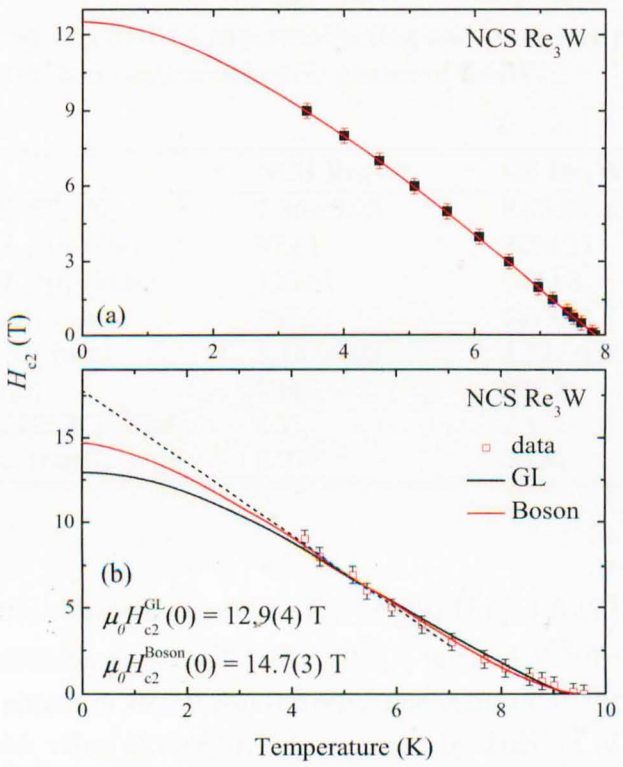

Figure 7.14: (a) and (b) Temperature dependence of the upper critical fields of the NCS and CS phases of Re_3W. The solid line in Fig. 7.14(a) is a fit to the data using the WHH model. The red line in Fig. 7.14(b) is a fit to the data using the Boson model. The black line is a fit to the data using the GL equation. The dashed line is a straight line fit to the data at low temperature region.

of H_{c2} at $T = 0$ K are comparable. The analysis presented above shows that $H_{c2}(0)$ appears to be slightly higher in the CS phase. Measurements at higher fields and lower temperatures are required to reveal to what extent Pauli limiting plays a role in determining $H_{c2}(0)$ in these materials.

7.6.1 Microscopic Parameters from Resistivity and Magnetization Measurements

The coherence length, ξ, can be calculated using the Ginzburg-Landau (GL) relation $\xi = (\Phi_\circ/2\pi H_{c2})^{1/2}$. With $H_{c2}^{\rm NCS}(0) = 125(1)$ kOe for NCS Re_3W, the estimated $\xi^{\rm NCS}(0)$ is 5.13(2) nm. To calculate the value of ξ for CS Re_3W, we have used the value of $H_{c2}^{\rm CS}(0)$ estimated using the Boson model as this model better fit the data close to T_c. $\xi^{\rm CS}(0)$ is deduced to be 4.73(5) nm from $H_{c2}^{\rm CS}(0) = 147(3)$ kOe.

Table 7.3: Measured and derived superconducting and transport parameters of the non-centrosymmetric and centrosymmetric phases of Re_3W.

	NCS Re_3W	CS Re_3W
T_c^{onset} (K)	7.80±0.05	9.40±0.05
$H_{c1}(0)$ (Oe)	97±1	279±11
$H_{c2}(0)$ (kOe)	125±1	147±3
$\lambda(0)$ (nm)	257±1	141±11
$\xi(0)$ (nm)	5.13±0.02	4.73±0.05
$\kappa(0)$	50±1	30±3
ρ(295 K)($\mu\Omega$m)	1.7	2.1
l_{tr} (nm)	0.277	0.224

Combining ξ and the standard expression $H_{c1} = \frac{\Phi_0}{4\pi\lambda^2}\left(\ln\frac{\lambda}{\xi} + 0.12\right)$ [22], we estimate the magnetic penetration depth, $\lambda^{NCS}(0) = 257(1)$ nm and $\lambda^{CS}(0) = 141(11)$ nm for the NCS and CS phases of Re_3W respectively. The value of $\lambda^{NCS}(0)$ is in resonable agreement with the value of 300(10) nm reported by Zuev *et al.* [200]. We used the values of $\lambda(0)$ and $\xi(0)$ to calculate the GL parameter $\kappa = \lambda/\xi$. They yield $\kappa^{NCS}(0) = 50(1)$ for the NCS phase and $\kappa^{CS} = 30(3)$ for the CS phase of Re_3W. The measured and derived superconducting and transport parameters of the NCS and the CS phases of Re_3W are listed in Table 7.3.

7.7 Heat Capacity Measurements of the CS and NCS Phases of Re_3W

The heat capacity was measured in a *Quantum Design* physical properties measurement system for temperatures from 2 K $\leq T \leq$ 300 K. The details about the experimental procedure are given in section 2.3.3.

The specific heat (C) of the NCS and CS phases of Re_3W are plotted in Fig. 7.15 in the form of C vs. T. As expected, no magnetic order could be detected down to 2 K and at high temperature, the signal is dominated by the contribution from lattice vibrations. To calculate the Einstein and Debye temperatures, we model the temperature dependence of the specific heat data of the NCS and CS phases of Re_3W by one-Debye and one-Einstein model, also called the Born-von Karman model

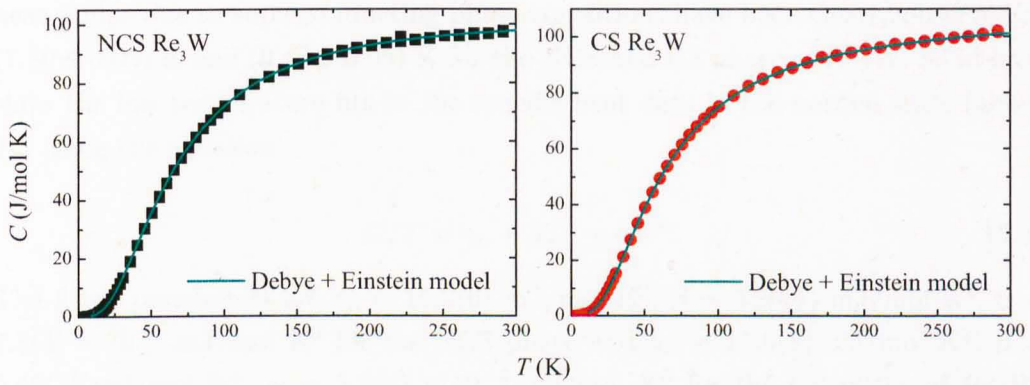

Figure 7.15: Temperature dependence of the specific heat C of the NCS and CS phases of Re_3W. Solid lines are the Debye+Einstein fit to the data.

$$C(T) = \gamma_n T + C_D(T, \Theta_D) + C_E(T, \Theta_E), \tag{7.4}$$

For more details, read section 3.3.4. The fits yield $\Theta_D = 228(6)$, $\Theta_E = 292(15)$ for the NCS phase and $\Theta_D = 219(1)$, $\Theta_E = 333(6)$ for the CS phase of Re_3W, respectively. The contributions of the Debye mode to the total specific heat are 78 % and 81 % for the NCS and CS phases of Re_3W, respectively. We can also resonably fit the data well using only a single Debye model and obtain a Debye temperature Θ_D of 258(1) and 247(1) K for the NCS and CS phases respectively.

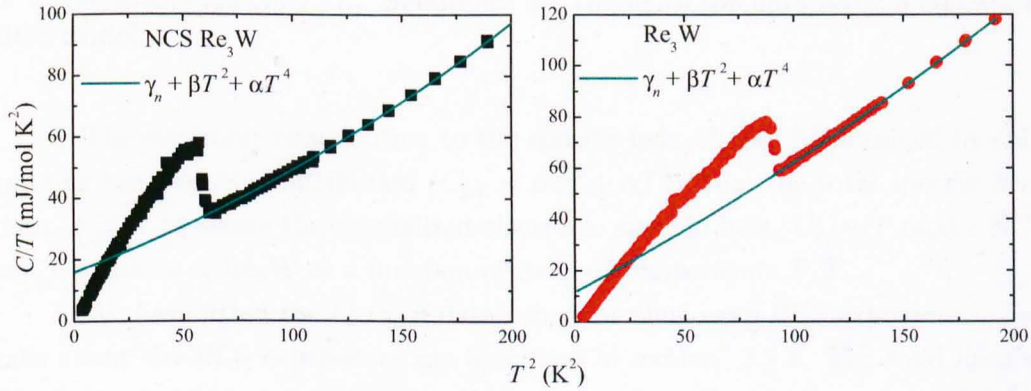

Figure 7.16: C/T vs T^2 of the NCS and CS phase of Re_3W. Solid lines are fit to the low-temperature data above T_c using Eq. 7.5.

Fig. 7.16 shows C/T vs T^2 of the NCS and CS phase of Re_3W. Specific

heat jumps due to superconducting phase transitions have been clearly observed at (7.80 ± 0.05) K and (9.40 ± 0.05) K for the NCS and CS phase of Re_3W. Solid lines show the low temperature fits to the specific heat data in the normal state (above T_c) using the equation

$$C/T = \gamma_n + \beta T^2 + \alpha T^4. \tag{7.5}$$

The fitted parameters are $\gamma_n = 15.9(6)$ mJ/mol K^2, $\beta = 0.26(1)$ mJ/mol K^4, $\alpha = 7.3(4) \times 10^{-4}$ mJ/mol K^6 for the NCS phase and $\gamma_n = 11.6(8)$ mJ/mol K^2, $\beta = 0.45(1)$ mJ/mol K^4, $\alpha = 5.1(4) \times 10^{-4}$ mJ/mol K^6 for the CS phase of Re_3W, respectively.

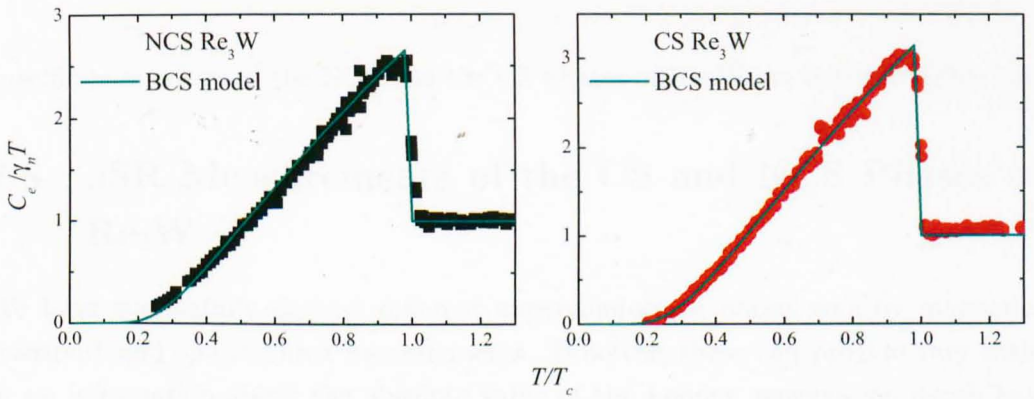

Figure 7.17: Electronic contribution to the specific heat of the NCS and CS phases of Re_3W as $C_e/\gamma_n T$ vs T/T_c. Solid lines are the fit to the data using a single-gap BCS model.

The electronic contribution to the specific heat C_e can be obtained by subtracting the phonon contribution ($C_{ph} = \beta T^3 + \alpha T^5$) from the total specific heat data. Fig. 7.16 shows the normalized electronic specific heat, $C_e/\gamma_n T$ of the NCS and CS phases of Re_3W as a function of reduced temperature T/T_c.

We have fitted the $C_e/\gamma_n T$ data using the single-gap BCS expressions. Details about the BCS expressions are described in section 3.3.4. The solid lines in Fig. 7.17 are the single-gap BCS model fit to the data. We obtain superconducting gaps, $\Delta_{NCS}(0) = 1.25(1)$ meV for the NCS phase and $\Delta_{CS}(0) = 1.56(1)$ meV for the CS phase of Re_3W. The magnitude of the superconducting gap, $\Delta/k_B T_c$, are 1.85(2) and 1.90(2) for the NCS and CS phases of Re_3W, respectively. In the weak-coupling BCS superconductors, the value of $\Delta/k_B T_c$ is 1.76. This implies that both the NCS and CS phases of Re_3W are strong coupling superconductors. The derived

Table 7.4: Fitted parameters of the non-centrosymmetric and centrosymmetric phases of Re_3W obtain from specific heat measurements.

	NCS Re_3W	CS Re_3W
Θ_D (K) $[n_D]$	228±6 [0.78]	219±1 [0.81]
Θ_E (K) $[n_E]$	292±15 [0.22]	333±6 [0.19]
γ_n (mJ/mol K^2)	15.9±0.6	11.6±0.8
β (mJ/mol K^4)	0.26±0.01	0.45±0.01
α (μJ/mol K^6)	0.73 ± 0.04	0.51 ± 0.04
$\Delta(0)$ (meV)	1.25±0.01	1.56±0.01
$\Delta(0)/k_BT_c$	1.85±0.02	1.90±0.02

specific parameters of the NCS and the CS phases of Re_3W are listed in Table 7.4.

7.8 μSR Measurements of the CS and NCS Phases of Re_3W

We have successfully derived different superconducting parameters by magnetic, transport and specific heat measurements. However, these can provide very little or no information about the absolute value of the London penetration depth and the symmetry of the superconducting gap structure. To investigate these features, we have performed muon spin rotation (μSR) experiments on Re_3W on the MuSR spectrometer of the ISIS pulsed muon facility, Rutherford Appleton Laboratory, UK [see section 2.4]. The sample was mounted on a silver plate with a circular area of $\sim$ 700 mm^2 and a small amount of diluted GE varnish was added to aid thermal contact. The sample and mount were then inserted into a Oxford Instruments He^3 sorbtion cryostat.

We have performed ZF-μSR study on both phases of Re_3W to detect the presence of any weak internal magnetism in the samples. Fig. 7.18 (a) and (b) show the ZF-μSR signals of the NCS and CS phase of Re_3W, respectively. Data taken above and below T_c show no sign of any change in the relaxation rate for both materials. These indicate the absence of any spontaneous internal field at the muon sites in the superconducting state and hence preserve the time-reversal symmetry in both systems.

The ZF data can be described by the Kubo-Toyabe function, [215]

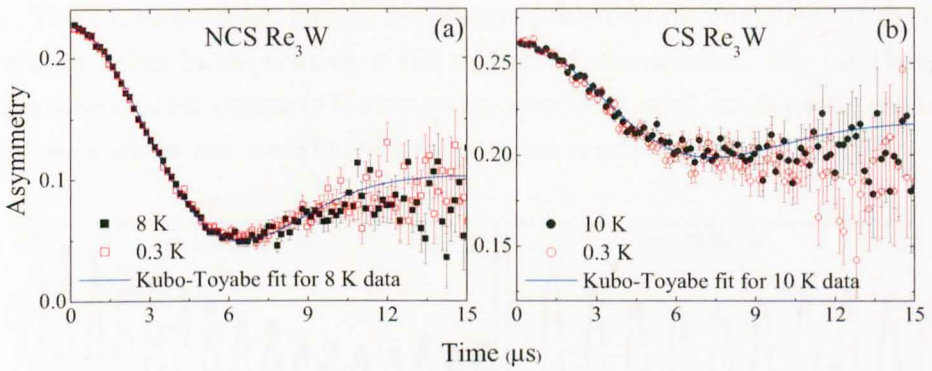

Figure 7.18: ZF- μSR time spectra collected at (a) 8 K and 0.3 K for the NCS phase of Re_3W and (b) 10 K and 0.3 K for the CS phase of Re_3W. The solid lines (in blue) are the fits to the data (above T_c) using the Gaussian Kubo-Toyabe function as described in the text.

Table 7.5: Parameters extracted from the fits using the Kubo-Toyabe function to the zero-field-μSR data collected above and below T_c for the non-centrosymmetric and centrosymmetric phases of Re_3W.

	NCS Re_3W	CS Re_3W
A_0	0.182±0.001 [8 K]	0.064±0.001 [10 K]
	0.178±0.001 [0.3 K]	0.069±0.002 [0.3 K]
σ (μs^{-1})	0.267±0.002 [8 K]	0.235±0.004 [10 K]
	0.266±0.002 [0.3 K]	0.234±0.005 [0.3 K]
A_{bkgd}	0.043±0.001 [8 K]	0.196±0.001 [10 K]
	0.047±0.001 [0.3 K]	0.191±0.002 [0.3 K]

$$G_z(t) = A_0 \left[\frac{1}{3} + \frac{2}{3}(1 - \sigma^2 t^2) \exp(-\frac{\sigma^2 t^2}{2}) \right] + A_{bkgd}, \tag{7.6}$$

where A_0 is the initial asymmetry, σ is the relaxation rate, and A_{bkgd} is the background signal. The fits yield the parameters shown in Table 7.5 with the same values for each phase obtained above and below T_c. The observed behaviour, and the values of σ extracted from the fits, are commensurate with the presence of random local fields arising from the nuclear moments within the samples, that are static on the time scale of the muon precession.

There is no evidence for any spontaneous coherent internal fields at the muon sites arising either in the normal or the superconducting states. Nor are there any additional relaxation channels that may be associated with more exotic electronic phenomena such as the breaking of time-reversal symmetry. [203, 204, 197]

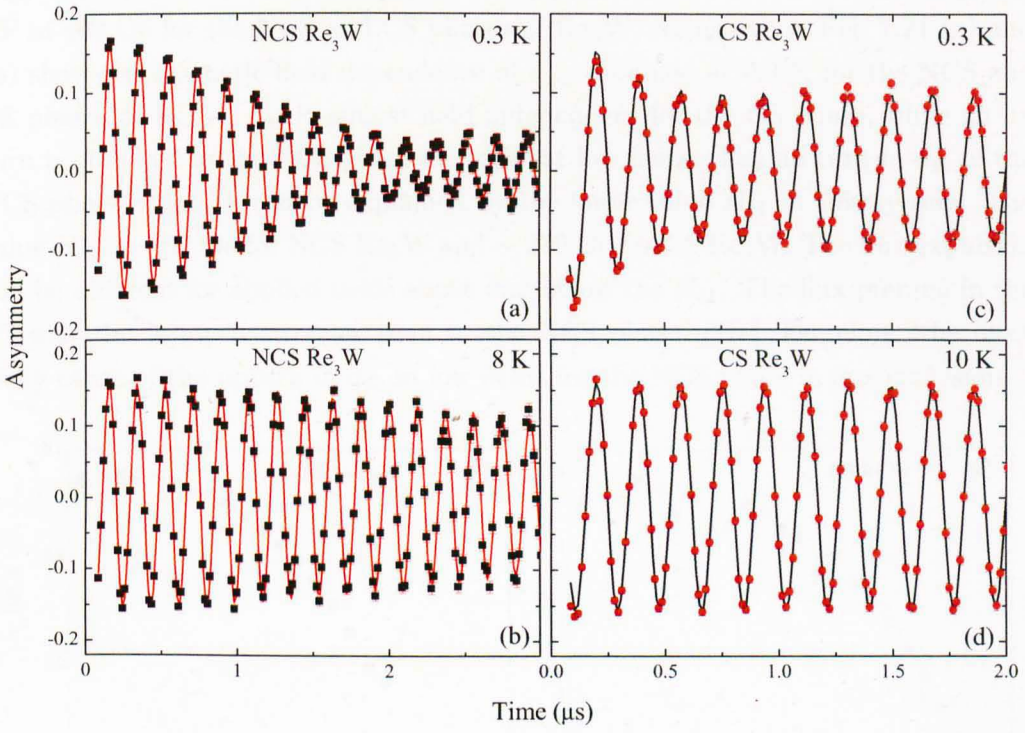

Figure 7.19: The transverse-field muon-time spectra (one component) collected (a) at $T = 0.3$ K and (b) at $T = 8.0$ K for the NCS phase and (c) at $T = 0.3$ K and (d) at $T = 10$ K for the CS phase of Re_3W in a magnetic field $H = 400$ Oe.

We have also performed a transverse field Muon spin rotation (TF-μSR) study on both phases of Re_3W which involves the application of an external magnetic field perpendicular (transverse) to the initial direction of the muon spin polarization. The muon spin precesses about the transverse field, with a frequency (called the Larmor frequency) that is proportional to the size of the field at the muon site in the material. Figure 7.19 (a) and (c) show the TF-μSR precession signals below T_c for the NCS and CS phases of Re_3W, while Figure 7.19 (b) and (d) are similar above T_c. The data were taken in an applied field of $H = 400$ Oe to make sure that the samples were in the mixed state. In the normal state, the signals of both phases of Re_3W decay very slowly. In this case, the muons experience only the homogeneous applied field over the whole sample. However, the decay is relatively fast in the

superconducting state ($T < T_c$). Here, the muons face an inhomogeneous field distribution inside the samples due to the formation of the flux-line lattice in the vortex state. To calculate the superconducting contribution to the Gaussian muon spin relaxation rate, σ_{sc}, TF-μSR precession data were fitted using equation 4.2. Fig. 7.20 (a) and (b) show the temperature dependence of σ_{sc} obtained in an applied TF of 400 Oe for the NCS and CS phases of Re_3W, respectively. Fig. 7.21 (a) and (b) show the magnetic field dependence of σ_{sc}, obtained at 0.3 K for the NCS and CS phases of Re_3W. σ_{sc} is almost field independent for the CS phase, while an up turn is observed in the NCS phase of Re_3W at low fields. The up turn in σ_{sc} of the NCS phase of Re_3W can be explained by the lower value H_{c1} in this system. The value H_{c1} is $\sim$ 97 Oe for NCS Re_3W and $\sim$ 279 Oe for CS Re_3W. The flux expulsion will be different for applied fields above and below the H_{c1}. The flux pinning in the CS material is much stronger than in the NCS phase. [216] Therefore, the most likely cause of the upturn in σ_{sc} in low fields for the NCS phase is flux exclusion.

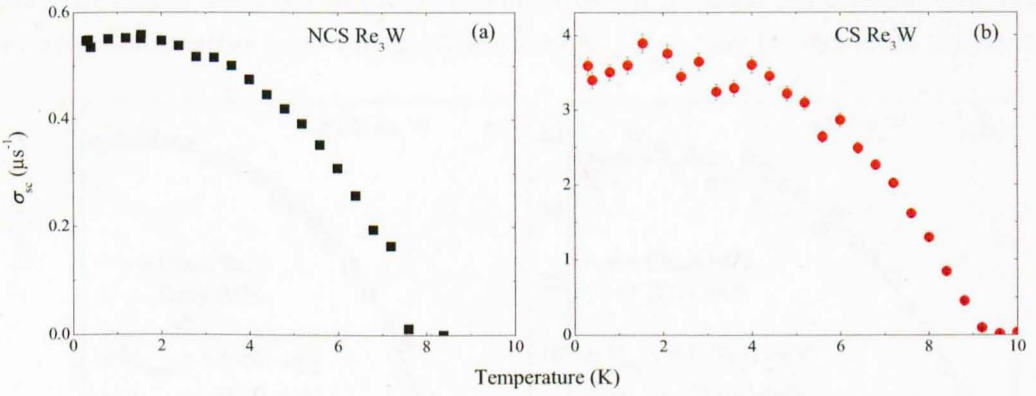

Figure 7.20: (a) The temperature dependence of the superconducting muon spin depolarization rate, σ_{sc}, collected in an applied magnetic field $H = 400$ Oe for the NCS and CS phase of Re_3W.

$\lambda(T)$ for the NCS and CS phases of Re_3W have been calculated using Eq. 3.11. Fig. 7.22 shows the $\lambda(T)$ for both phases. The data can be fitted for an s-wave BCS superconductor in the clean limit (no defects) using the expression as described in section 3.3.5. In the dirty limit (maximal defects), we have

$$\left[\frac{\lambda^2(0)}{\lambda^2(T)}\right]_{\text{dirty}} = \frac{\Delta(T)}{\Delta(0)} \tanh\left(\frac{\Delta(T)}{2k_BT}\right), \tag{7.7}$$

Note, the error in $\lambda(0)$ is the statistical error arising from the fit to the $\lambda^{-2}(T)$ data

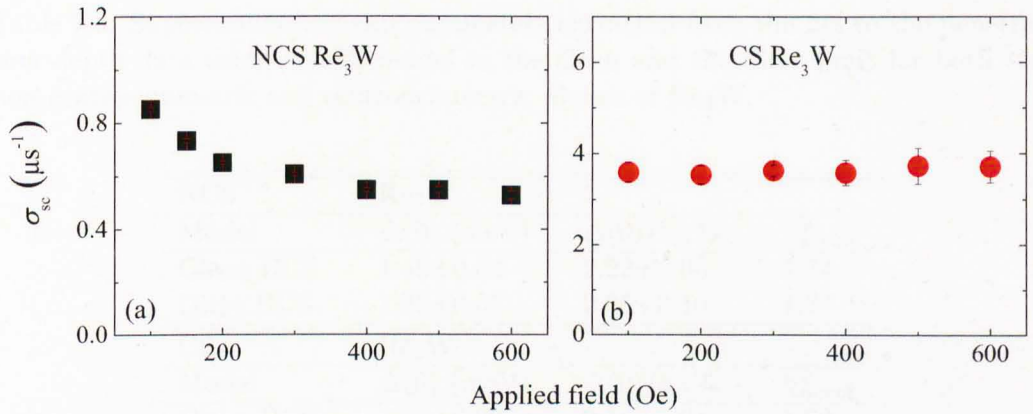

Figure 7.21: The magnetic field dependence of σ_{sc}, obtained at 0.3 K for the corresponding phases.

using the model described in the text. The error quoted does not take into account any systematic errors (e.g. vortex lattice disorder) that may be present in the data.

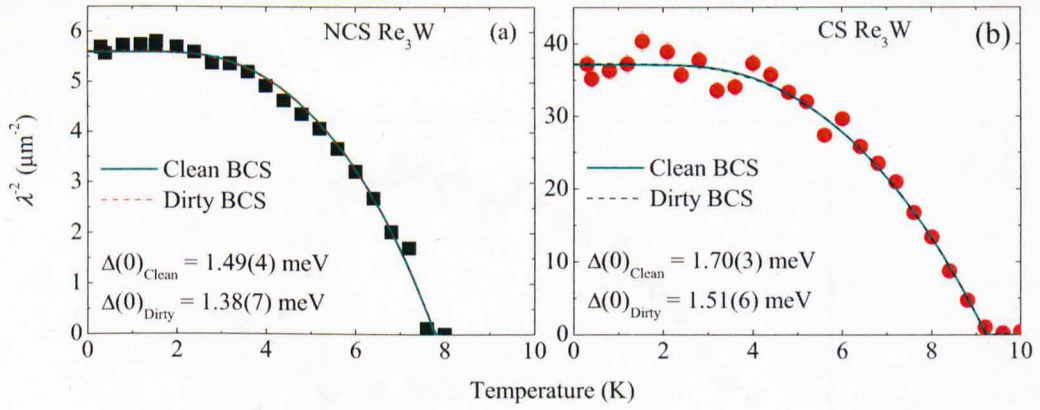

Figure 7.22: The temperature dependences of the London penetration depth as a function of temperature for (a) the NCS and (b) the CS phases of Re_3W, respectively. The solid lines are the clean and dashed lines are the dirty BCS s-wave fit to the data.

We obtain good fits to the $\lambda^{-2}(T)$ data for the NCS and the CS phases using both the models discussed above (see Fig. 7.22). The parameters extracted from these fits are shown in Table 7.6. There is little difference between the quality of the fits, as measured by χ^2_{norm}, in the clean and dirty limits. As expected the magnitudes of the gap in the clean limit are larger than those obtained for the dirty

Table 7.6: Superconducting gap parameters extracted from the fits to the penetration depth data using a BCS model in the clean and the dirty limit for both the non-centrosymmetric and centrosymmetric phases of Re_3W.

NCS	Re_3W		
Model	$\Delta(0)$ (meV)	$\Delta(0)/k_BT_c$	χ^2_{norm}
Clean BCS	1.49±0.04	2.22±0.06	1.74
Dirty BCS	1.38±0.07	2.05±0.10	1.72
CS	Re_3W		
Model	$\Delta(0)$ (meV)	$\Delta(0)/k_BT_c$	χ^2_{norm}
Clean BCS	1.70±0.03	2.14±0.04	1.60
Dirty BCS	1.51±0.06	1.90±0.08	1.57

limit but in both cases the values obtained place the materials in the strong-coupling limit. Penetration depth measurements carried out on the NCS phase of Re_3W by rf tunnel diode resonator and point-contact spectroscopy also suggest that the NCS phase of Re_3W is an *s*-wave superconductor, although Zuev *et al.* could only obtain good fits to their data for NCS Re_3W in the dirty limit. [200, 201, 202]

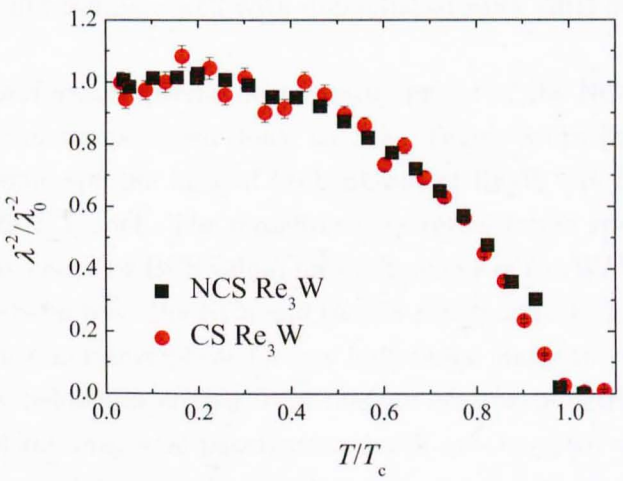

Figure 7.23: Normalized superfluid density, $\lambda^{-2}(0)/\lambda^{-2}(T)$ as a function of T/T_c for the CS and NCS phases of Re_3W.

Figure 7.23 shows the normalized superfluid density, $\lambda^{-2}/\lambda_0^{-2}$ as a function of T/T_c for the CS and NCS phases of Re_3W. Normalized data of both CS and NCS phases of Re_3W agree with each other and hence clearly show the same gap

symmetry for both phases.

7.9 Summary and Conclusions

We have shown that there are two different phases of Re_3W. One phase is non-centrosymmetric with an α-Mn structure and is superconducting with a T_c of (7.80± 0.05) K. The other phase is centrosymmetric with a hexagonal structure and is also superconducting with a T_c of (9.40 ± 0.05) K. Switching between the two phases is made possible by annealing (CS to NCS) or remelting (NCS to CS) the samples. The full hysteresis loops of the CS sample of Re_3W show giant flux jumps, while no jumps are observed for the NCS sample. The flux jumps are due to thermomagnetic instabilities induced by the motion of vortices into the superconductor combined with the sudden redistribution of the vortices within the sample [208]. The temperature dependence of H_{c2} of the NCS phase for Re_3W can be fitted using the WHH model which yields $H_{c2}^{\mathrm{NCS}}(0) = 125(1)$ kOe. In contrast, $H_{c2}(T)$ of the CS phase of Re_3W is linear at lower temperature and has a positive curvature nearer to T_c. A Boson model fit to the data gives $H_{c2}^{\mathrm{CS}}(0) = 147(3)$ kOe. Using GL relations, the penetration depths are estimated to be $\lambda^{\mathrm{NCS}} = 257(1)$ nm and $\lambda^{\mathrm{CS}} = 141(11)$ nm and the coherence lengths are calculated to be $\xi^{\mathrm{NCS}} = 5.13(1)$ nm and $\xi^{\mathrm{CS}} = 4.73(1)$ nm at $T = 0$ K. Our results compare well with unpublished work [201] on the NCS phase of Re_3W.

We have performed specific heat measurements of the NCS and CS phases of Re_3W from room temperature down to 2 K. Temperature dependence of the normalized electronic specific heat of both phases of Re_3W can be fitted well using a single-gap BCS model. The measurements reveal larger specific heat jumps (compared to weak-coupling BCS value) for both phases of Re_3W. We have also performed a μSR study on both the NCS and the CS superconducting phases of Re_3W. There is no evidence in either phase for any long-range magnetic order, nor for any unusual electronic behaviour arising from the non-centrosymmetric structure. The absolute values of the magnetic penetration depth are $\lambda_{NCS}(0) = 418(6)$ nm and $\lambda_{CS}(0) = 164(7)$ nm. Interestingly, the change in structure appears to have no effect on either the symmetry or the temperature dependence of the superconducting gap. The temperature dependence of λ for both structural phases of Re_3W can be described using a single gap s-wave BCS model. The magnitudes of the superconducting gaps both from heat capacity and μSR studies suggest that both materials are strong-coupling superconductors.

Chapter 8

Conclusions

Research into superconductivity has been highly active since its discovery in 1911. A great deal of progress has been made into understanding the fundamental causes of superconducting behaviour in different types of materials, and developing superconductors for technological applications in real life. The research work presented in this thesis has been focused on investigating the unconventional superconducting properties in $FeTe_{0.5}Se_{0.5}$, $FeTe_{1-x}S_x$ ($0.10 \leq x \leq 0.50$), $Lu_2Fe_3Si_5$, CaAlSi, ZrB_{12} and two different superconducting phases of Re_3W. The majority of the research presented has focused on the symmetry of the superconducting gap and the FLL in these compounds determined from low temperature specific heat, μSR and SANS studies. By explaning the observed exotic features in these compounds a broader understanding of the underlying physics of this class of material is achieved. Furthermore, it is hoped that by studying these particular materials new physics to explain the phenomena observed may be developed.

The initial work carried out used Fe-based superconductors. We have synthesized good quality polycrystalline and single crystal samples of $FeTe_{0.5}Se_{0.5}$ and $FeTe_{1-x}S_x$ for $x = 0.1, 0.2, 0.3, 0.4$ and 0.5. Our detailed studies of the structural, magnetic, thermodynamic and other superconducting properties of this sample reveal several important results: The T_c of $FeTe_{0.5}S_{0.5}$ is found to decrease linearly with pressure with the pressure coefficient, $dT_c/dP = -0.27(1)$ K/kbar. The results are consistent with other experimental data of the $FeTe_{1-x}S_x$ system [69, 102] but different when compared to the other iron chalcogenide superconductors where T_c initially increases with P. This different scenario can be understood by its structural phase transition with pressure. We have performed low temperature specific heat measurements of $FeTe_{0.5}Se_{0.5}$. Our analysis shows that the electronic specific heat of $FeTe_{0.5}Se_{0.5}$ can be fitted using a two-band BCS model with isotropic gaps,

similar to MgB_2. We have also performed μSR measurements on superconducting $FeTe_{0.5}Se_{0.5}$. The temperature dependence of the magnetic penetration depth of $FeTe_{0.5}Se_{0.5}$ is found to be compatible with either a two-gap $s + s$-wave or an anisotropic s-wave model. This result is consistent with our heat capacity data and also with other reported experimental data [76, 104]. These results along with other published data suggest that $FeTe_{0.5}Se_{0.5}$ can be described as a two-band superconductor. Further studies on higher purity single crystal samples are desirable as the presence of impurities can sometimes mask the true nature of the superconducting gap. [105] μSR experiments have been performed on four different compositions of $FeTe_{1-x}S_x$ and show an AF transition at low temperature. Similar AF transitions have also been observed in the magnetization data of $FeTe_{1-x}S_x$. The magnetic transitions may be due to an ordering of the iron spins. However, more studies are required to understand fully the exact nature of these magnetic transitions.

To understand the underlying physics of two-gap superconductivity better, we continued our research with another candidate of this class of superconductor $Lu_2Fe_3Si_5$. We have synthesized high quality polycrystalline samples of $Lu_2Fe_3Si_5$ and performed low-temperature specific heat measurements to confirm the presence of two distinct superconducting gaps. Low-temperature specific heat measurements on $Lu_2Fe_3Si_5$ reveal a reduced normalized specific heat jump at T_c and a second smaller jump at nearly $T_c/5$. Specific heat data of $Lu_2Fe_3Si_5$ can be fitted well using a two-gap BCS s-wave model. We have also performed a μSR study on the same polycrystalline sample. The temperature dependence of the magnetic penetration depth data was fitted with three different models. A two-gap $s + s$-wave model provides the best fit to the data and hence support the specific heat results. These results are consistent with other reported data for this system [119, 120, 114, 31, 125]. The gap magnitudes calculated from specific heat and μSR studies are in resonable agreement. A more precise analysis using a self-consistent two-gap model proposed by Kogan *et al.* [126] may be required to fully understand the coupling strength between the two bands in this system. This model has been developed within the quasi-classical Eilenberger weak-coupling formalism with one inter-band and two in-band pairing potentials and tested with experimental data from well-known two-band superconductors MgB_2 and V_3Si. Work is under way to explain our specific heat and μSR data using this model.

We have worked with another superconductor CaAlSi, structurally similar to the two-band superconductor MgB_2. CaAlSi is a low κ (≈ 5) superconductor and there is a debate about whether the superconducting gap symmetry in CaAlSi is single or multi-gap in nature. Different measurements on CaAlSi such as ARPES, μSR

and optical measurements suggest an anisotropic or multi-gapped structure [148]. In contrast, tunnel-diode resonator measurements and break-junction tunneling spectroscopy both suggest that there is a single weakly anisotropic s-wave gap in CaAlSi. To clarify this debate, we have performed a SANS study on a single crystal sample of CaAlSi. We observe a well-defined flux line lattice in a very low field of only 54 Oe. This in itself is noteworthy as this is one of the lowest fields in which a FLL has ever been imaged using the SANS technique. In addition, it is interesting that a well defined FLL forms just above H_{c1} ($\approx$ 50 Oe) where the inter vortex distance is many times longer than the penetration depth. There have been suggestions that in this class of materials at lower fields ($\approx$ 1 Oe) an attractive inter vortex interaction will lead to a clustering of the vortices. While we acknowledge that we are well above this field regime, it is important to demonstrate that the dominant inter vortex interaction in this material at the low field regime is repulsive, leading to the formation of a symmetric hexagonal FLL. We observe a hex-to-hex FLL reorientation at just 200 Oe. We have carefully considered what may drive the reorientation of the FLL. We cannot unequivocally state the source of the reorientation. We can, however, argue strongly in favour of the reorientation being driven by non-local effects. This contrasts with the situation in MgB_2 where it is claimed that the FLL reorientation is driven by the effects of two superconducting bands. We argue that non local effects may be ubiquitous in this class of materials. Our measurement of the field dependent form factor from the field distribution is explained by a single coherence length, and the anisotropy of this coherence length is the same as the anisotropy of the penetration depth. Both features are very unlikely to occur in a multi-band superconductor, hence supporting the single gap arguments. This has important implications for those working to understand the physics of the AlB_2 class of materials. The equality of the values of the anisotropy for the penetration depth measured here and the coherence length measured elsewhere may hint at the fact that this is indeed a simple one band system.

So far we have discussed about the unconventional superconductors with two different superconducting gaps. However, there are some other unconventional superconductors which have different unusual behaviours. One of this kind of superconductors is ZrB_{12} which have a very low-κ value. It is also reported that the κ in this material lies close to the cross-over value of $1/\sqrt{2}$ between Type-I and Type-II superconductivity and that κ may change with temperature [179]. To find out whether ZrB_{12} is a Type-I or Type-II superconductor or has a more exotic nature in which both types of superconductivity coexist, it was of interest to map out the complete B-T phase diagram of ZrB_{12} to find out the regions for different types

of superconductivity. To this end, we have grown a high quality single crystal of ZrB_{12} using the optical floating zone method and characterized it using a range of in-house measurements. We have mapped out the superconducting phase diagram of ZrB_{12} in great detail from the μSR measurements. By measuring the local field distribution for different applied fields and temperatures we have found evidence of the Meissner, mixed, and intermediate states in the ZrB_{12} superconductor. The intermediate state is characteristic of a Type-I superconductor, but the mixed state is characteristic of a Type-II superconductor. We have also observed regions of co-existence between different states. Observation of an intermediate mixed state in a low-κ and Type-II superconductor has been reported by Essmann and Träuble using the decoration technique [184], while our system shows direct evidence of such a state. The observed phase diagram for superconductivity is unusual and implies that κ may change with temperature (or at least is close to the Type-I / Type-II boundary) since different regions of the phase diagram are characteristic of Type-I and Type-II behaviour. More studies (such as SANS, etc.) are required to verify our claim and also to understand the B-T phase diagram of ZrB_{12} in more detail. In addition, at low fields an attractive interaction between vortices may also be playing a role, as has been suggested for the Type-1.5 description of MgB_2 (see ref. [20]) where one band is thought to have Type-I character while the other retains its Type-II nature. ZrB_{12} may be the ideal system to test such propositions.

Another class of unconventional superconductors are the non-centrosymmetric superconductors. They are well-known for exhibiting unusual magnetic properties including nodes in the superconducting gap function or the involvement of spin-triplet pairs in the superconducting condensate, high upper critical fields, time-reversal symmetry breaking, coexistence of ferromagnetic or anti-ferromagnetic ordering with the superconducting phase, etc. These arise due to the lack inversion symmetry of their crystal structures and strong correlations between electrons. This motivated us to investigate if Re_3W exhibits any such unusual behaviour. We have grown good quality polycrystalline sample of Re_3W. While growing the sample, we found two different superconducting phases of Re_3W. One phase is non-centrosymmetric (NCS) with an α-Mn structure and is superconducting with a T_c of (7.80 ± 0.05) K. The other phase is centrosymmetric (CS) with a hexagonal structure and is also superconducting with a T_c of (9.40 ± 0.05) K. Switching between the two phases is made possible by annealing (CS to NCS) or remelting (NCS to CS) the samples. The full hysteresis loops of the CS sample of Re_3W show giant flux jumps, while no jumps are observed for the NCS sample. We have performed specific heat measurements of the NCS and CS phases of Re_3W from room temperature down to

2 K. Low temperature electronic specific heat of both phases of Re_3W can be fitted well using a single-gap BCS model. The measurements reveal larger specific heat jumps (compared to weak-coupling BCS value) for both phases of Re_3W. We have also performed a μSR study on both the NCS and the CS superconducting phases of Re_3W. There is no evidence in either phase for any long-range magnetic order, nor for any unusual electronic behaviour arising from the non-centrosymmetric structure. Interestingly, the change in structure appears to have no effect on either the symmetry or the temperature dependence of the superconducting gap. The temperature dependence of λ for both structural phases of Re_3W can be described using a single gap s-wave BCS model. The magnitudes of the superconducting gaps both from heat capacity and μSR studies suggest that both materials are strong-coupling superconductors. This, and similar systems if they exist, offer a good opportunity to study the interplay between the structure, spin-orbit coupling, and the superconducting properties of intermetallic systems.

Finally, we have successfully studied the properties of different unconventional superconducting materials which exhibit unusual pairing mechanisms and other exotic properties that cannot explained by a simple BCS model. By studying such systems, we hope to gain a better understanding of the mechanism involved. This may help to find new routes to the discovery of unconventional superconductors with higher T_c values and greater technological applications.

Bibliography

[1] H. K. Onnes. *Comm. Leiden*, 1911.

[2] W. Meissner and R. Ochsenfeld. *Naturwiss*, 21:787, 1933.

[3] F. London and H. London. *Proc. Roy. Soc. (London)*, A149:71, 1935.

[4] V. L. Ginzburg and L. D. Landau. *Zh. Eksp. Teor. Fiz.*, 20:1064, 1950.

[5] J. Bardeen, L. N. Cooper, and J. R. Schrieffer. *Phys. Rev.*, 108:1175, 1957.

[6] W. L. McMillan. *Phys. Rev.*, 167:331, 1968.

[7] B. T. Matthias, T. H. Geballe, R. H. Willens, E. Corenzwit, and Jr. G. W. Hull. *Phys. Rev. A*, 139:1501, 1965.

[8] R. Chevrel, M. Hirrien, and M. Sergent. *Polyhedron*, 5:87, 1986.

[9] J. G. Bednorz and K. A. Müller. *Z. Phys. B: Condens. Matter*, 64:189, 1986.

[10] M. K. Wu, J. R. Ashburn, C. J. Torng, P. H. Hor, R. L. Meng, L. Gao, Z. J. Huang, Y. Q. Wang, and C. W. Chu. *Phys. Rev. Lett.*, 58:908, 1987.

[11] A. Schilling, M. Cantoni, J. D. Guo, and H. R. Ott. *Nature*, 363:56, 1993.

[12] R. J. Cava, H. Takagi, B. Batlogg, H. W. Zandbergen, J. J. Krajewski, W. F. Jr. Peck, R. B. van Dover, R. J. Felder, T. Siegrist, K. Mizuhashi, J. O. Lee, H. Eisaki, S. A. Carter, and S. Uchida. *Nature*, 367:146, 1994.

[13] J. Nagamatsu, N. Nakagawa, T. Muranaka, Y. Zenitani, and J. Akimitsu. *Nature (London)*, 410:63, 2001.

[14] Y. Kamihara, T. Watanabe, M. Hirano, and H. Hosono. *J. Am. Chem. Soc.*, 130:3296, 2008.

[15] C. Wang, L. Li, S. Chi, Z. Zhu, Z. Ren, Y. Li, Y. Wang, X. Lin, Yo. Luo, S. Jiang, X. Xu, G. Cao, and Z. Xu. *Europhys. Lett.*, 83:67006, 2008.

[16] A. A. Abrikosov. *Sov. Phys. JETP*, 5:1174, 1957.

[17] E. H. Brandt. *Rep. Prog. Phys.*, 58:1465, 1995.

[18] M. Tinkham. *Introduction to Superconductivity.* McGraw-Hill, New York, 1975.

[19] J. Auer and H. Ullmaier. *Phys. Rev. B*, 7:136, 1973.

[20] V. Moshchalkov, M. Menghini, T. Nishio, Q. H. Chen, A. V. Silhanek, V. H. Dao, L. F. Chibotaru, N. D. Zhigadlo, and J. Karpinski. *Phys. Rev. Lett.*, 102:117001, 2009.

[21] C. S. Gorter and H. Casimir. *Zeitschrift fr Technische Physik*, 15:539, 1934.

[22] M. Tinkham. *Introduction to Superconductivity.* McGraw-Hill, New York, 1975.

[23] A. Carrington and F. Manzano. *Physica C*, 385:205, 2003.

[24] A. P. Mackenzie and Y. Maeno. *Rev. Mod. Phys.*, 75:657, 2003.

[25] C. C. Tsuei and J. R. Kirtley. *Rev. Mod. Phys.*, 72:969, 2000.

[26] M. Cyrot and D. Pavuna. *Introduction to superconductivity and high-T_c materials.* World Scientific, 1992.

[27] H. Suhl, B. T. Matthias, and L. R. Walker. *Phys. Rev. Lett.*, 3:552, 1959.

[28] M. Iavarone, G. Karapetrov, A. E. Koshelev, W. K. Kwok, G. W. Crabtree, D. G. Hinks, W. N. Kang, Eun-Mi Choi, Hyun Jung Kim, Hyeong-Jin Kim, and S. I. Lee. *Phys. Rev. Lett.*, 89:187002, 2002.

[29] T. Yokoya, T. Kiss, T. Watanabe, S. Shin, M. Nohara, H. Takagi, and T. Oguchi. *Phys. Rev. Lett.*, 85:4952, 2000.

[30] R. Nagarajan, Chandan Mazumdar, Zakir Hossain, S. K. Dhar, K. V. Gopalakrishnan, L. C. Gupta, C. Godart, B. D. Padalia, and R. Vijayaraghavan. *Phys. Rev. Lett.*, 72:274, 1994.

[31] Y. Nakajima, T. Nakagawa, T. Tamegai, and H. Harima. *Phys. Rev. Lett.*, 100:157001, 2008.

[32] R. Jenkins and R. Snyder. *Introduction to X-Ray Powder Diffractometry.* edited by J. Wiley & Sons, Inc.(New York), 1996.

[33] http://www.panalytical.com.

[34] http://www.icdd.com/.

[35] C. Marin and E. Diéguez. *Orientation of Single Crystals by Back-reflection Laue Pattern Simulation.* edited by World Scientific, 1999.

[36] http://technoinfo.co.uk/catalog/41.html.

[37] *CrysAlisPro*, Oxford Diffraction Ltd., Version 1.171.33.34d (release 27-02-2009 CrysAlis171.NET).

[38] D. C. Bell and A. J. Garratt-Reed. *Energy Dispersive X-ray Analysis in the Electron Microscope.* edited by BIOS Scientific Publisher Ltd. (Oxford, UK), 2003.

[39] *Quantum Design* Magnetic Property Measurement System: Hardware Manual (2000).

[40] *Quantum Design* Physical Property Measurement System: Heat Capacity Option Users Manual (2000).

[41] A. Schenck. *Muon Spin Rotation Spectroscopy.* Adam Hilger Ltd., Bristol and Boston, 1985.

[42] A. Schenck and F. N. Gygax. *Handbook of Magnetic Materials.* edited by K. H. J. Buschow (Amsterdam: Elsevier), 1995.

[43] P. Dalmas de Réotier and A. Yaouanc. *J. Phys.: Condens. Matter*, 9:9113, 1997.

[44] A. Amato. *Rev. Mod. Phys.*, 69:1119, 1997.

[45] A. D. Hillier and R. Cywinski. *Appl. Mag. Res.*, 13:95, 1997.

[46] S. J. Blundell. *Contemporary Physics*, 40:175, 1999.

[47] J. E. Sonier, J. H. Brewer, and R. F. Kiefl. *Rev. Mod. Phys.*, 72:769, 2000.

[48] R. L. Garwin, L. M. Lederman, and M. Weinrich. *Phys. Rev.*, 105:1415, 1957.

[49] A. C. Hannon. *Nuclear Instruments and Methods in Physics Research A*, 551: 88, 2005.

[50] P. Day, J. E. Enderby, W. G. Williams, L. C. Chapon, A.C. Hannon, P. G. Radaelli, and A. K. Soper. *Neutron News*, 15:19, 2004.

[51] Y. Kamihara, H. Hiramatsu, M. Hirano, R. Kawamura, H. Yanagi, T. Kamiya, and H. Hosono. *J. Am. Chem. Soc.*, 128:10012., 2006.

[52] X. H. Chen, T. Wu, G. Wu, R. H. Liu, H. Chen, and D. F. Fang. *Nature (London)*, 453:761, 2008.

[53] H. Takahashi, K. Igawa, K. Arii, Y. Kamihara, M. Hirano, and H. Hosono. *Nature (London)*, 453:376, 2008.

[54] H. Kito, H. Eisaki, and A. Iyo. *J. Phys. Soc. Japan*, 77:063707, 2008.

[55] M. Rotter, M. Tegel, and D. Johrendt. *Phys. Rev. Lett.*, 101:107006, 2008.

[56] X.C. Wang, Q.Q. Liu, Y.X. Lv, W.B. Gao, L.X. Yang, R.C. Yu, F.Y. Li, and C.Q. Jin. *Solid State Communications*, 148:538, 2008.

[57] F.-C. Hsu, J.-Y. Luo, K.-W. Yeh, T.-K. Chen, T.-W. Huang, Phillip M. Wu, Y.-C. Lee, Y.-L. Huang, Y.-Y. Chu, D.-C. Yan, and M.-K. Wu. *Proc. Natl. Acad. Sci.*, 105:14262, 2008.

[58] X. Zhu, F. Han, G. Mu, P. Cheng, B. Shen, B. Zeng, and H.-H. Wen. *Phys. Rev. B*, 79:220512, 2009.

[59] S. Margadonna, Y. Takabayashi, Y. Ohishi, Y. Mizuguchi, Y. Takano, T. Kagayama, T. Nakagawa, M. Takata, and K. Prassides. *Phys. Rev. B*, 80:064506, 2009.

[60] C. Wang, S. Jiang, Q. Tao, Z. Ren, Y. Li, L. Li, C. Feng, J. Dai, G. Cao, and Z. a. Xu. *Europhys. Lett.*, 86:47002, 2009.

[61] W. Guan, Y. Xu, S. R. Sheen, Y. C. Chen, J. Y. T. Wei, H. F. Lai, M. K. Wu, and J. C. Ho. *Phys. Rev. B*, 49:15993, 1994.

[62] K.-W. Yeh, T.-W. Huang, Y.-l. Huang, T.-K. Chen, F.-C. Hsu, P. M. Wu, Y.-C. Lee, Y.-Y. Chu, C.-L. Chen, J.-Y. Luo, D.-C. Yan, and M.-K. Wu. *Europhys. Lett.*, 84:37002, 2008.

[63] M. H. Fang, H. M. Pham, B. Qian, T. J. Liu, E. K. Vehstedt, Y. Liu, L. Spinu, and Z. Q. Mao. *Phys. Rev. B*, 78:224503, 2008.

[64] N. C. Gresty, Y. Takabayashi, A. Y. Ganin, M. T. McDonald, J. B. Claridge, D. Giap, Y. Mizuguchi, Y. Takano, T. Kagayama, Y. Ohishi, M. Takata, M. J. Rosseinsky, S. Margadonna, and K. Prassides. *J. Am. Chem. Soc.*, 131:16944, 2009.

[65] T. Kida, T. Matsunaga, M. Hagiwara, Y. Mizuguchi, Y. Takano, and K. Kindo. *J. Phys. Soc. Japan*, 78:113701, 2009.

[66] C. S. Yadav and P. L. Paulose. *New J. Phys.*, 11:103046, 2009.

[67] P. K. Biswas, G. Balakrishnan, C. V. Tomy, D. M. Paul, and M. R. Lees. unpublished, 2010.

[68] A. Subedi, L. Zhang, D. J. Singh, and M. H. Du. *Phys. Rev. B*, 78:134514, 2008.

[69] Y. Mizuguchi, F. Tomioka, S. Tsuda, T. Yamaguchi, and Y. Takano. *Appl. Phys. Lett.*, 94:012503, 2009.

[70] A. S. Sefat, R. Jin, M. A. McGuire, B. C. Sales, D. J. Singh, and D. Mandrus. *Phys. Rev. Lett.*, 101:117004, 2008.

[71] Y. Mizuguchi, K. Deguchi, S. Tsuda, T. Yamaguchi, and Y. Takano. *Phys. Rev. B*, 81:214510, 2010.

[72] K Deguchi, Y Mizuguchi, Y Kawasaki, T Ozaki, S Tsuda, T Yamaguchi, and Y Takano. *Supercond. Sci. Technol.*, 24:055008, 2011.

[73] Y. Mizuguchi, K. Deguchi, S. Tsuda, T. Yamaguchi, and Y. Takano. *Europhys. Lett.*, 90:57002, 2010.

[74] Y. Mizuguchi, F. Tomioka, S. Tsuda, T. Yamaguchi, and Y. Takano. *J. Phys. Soc. Japan*, 78:074712, 2009.

[75] F. Walz. *J. Phys.: Condens. Matter*, 14:R285, 2002.

[76] R. Khasanov, K. Conder, E. Pomjakushina, A. Amato, C. Baines, Z. Bukowski, J. Karpinski, S. Katrych, H.-H. Klauss, H. Luetkens, A. Shengelaya, and N. D. Zhigadlo. *Phys. Rev. B*, 78:220510(R), 2008.

[77] N. R. Werthamer, E. Helfand, and P. C. Hohenberg. *Phys. Rev.*, 147:295, 1966.

[78] G. F. Chen, Z. G. Chen, J. Dong, W. Z. Hu, G. Li, X. D. Zhang, P. Zheng, J. L. Luo, and N. L. Wang. *Phys. Rev. B*, 79:140509, 2009.

[79] A. Gurevich, S. Patnaik, V. Braccini, K. H. Kim, C. Mielke, X. Song, L. D. Cooley, S. D. Bu, D. M. Kim, J. H. Choi, L. J. Belenky, J. Giencke, M. K. Lee, W. Tian, X. Q. Pan, A. Siri, E. E. Hellstrom, C. B. Eom, and D. C. Larbalestier. *Supercond. Sci. Technol.*, 17:278, 2004.

[80] A. Gurevich. *Phys. Rev. B*, 67:184515, 2003.

[81] E. S. R. Gopal. *Specific Heats at Low Temperatures.* Plenum, New York, 1996.

[82] A. Günther, J. Deisenhofer, C. Kant, H.-A. Krug von Nidda, V. Tsurkan, and A. Loidl. *Supercond. Sci. Technol.*, 24:045009, 2011.

[83] B. Mühlschlegel. *Z. Phys.*, 155:313, 1959.

[84] E. H. Brandt. *Phys. Rev. B*, 37:2349, 1988.

[85] H. Padamsee, J. E Neighbor, and C. A. Shiffman. *J. Low Temp. Phys.*, 12: 387, 1973.

[86] R. Prozorov and R. W. Giannetta. *Supercond. Sci. Technol.*, 19:R41, 2006.

[87] T. Kondo, A. F. Santander-Syro, O. Copie, Chang Liu, M. E. Tillman, E. D. Mun, J. Schmalian, S. L. Bud'ko, M. A. Tanatar, P. C. Canfield, and A. Kaminski. *Phys. Rev. Lett.*, 101:147003, 2008.

[88] C. Martin, M. E. Tillman, H. Kim, M. A. Tanatar, S. K. Kim, A. Kreyssig, R. T. Gordon, M. D. Vannette, S. Nandi, V. G. Kogan, S. L. Bud'ko, P. C. Canfield, A. I. Goldman, and R. Prozorov. *Phys. Rev. Lett.*, 102:247002, 2009.

[89] V.I. Fesenko, V.N. Gorbunov, and V.P. Smilga. *Physica C*, 176:551, 1991.

[90] Y. J. Uemura, G. M. Luke, B. J. Sternlieb, J. H. Brewer, J. F. Carolan, W. N. Hardy, R. Kadono, J. R. Kempton, R. F. Kiefl, S. R. Kreitzman, P. Mulhern, T. M. Riseman, D. Ll. Williams, B. X. Yang, S. Uchida, H. Takagi, J. Gopalakrishnan, A. W. Sleight, M. A. Subramanian, C. L. Chien, M. Z. Cieplak, Gang Xiao, V. Y. Lee, B. W. Statt, C. E. Stronach, W. J. Kossler, and X. H. Yu. *Phys. Rev. Lett.*, 62:2317, 1989.

[91] H. Luetkens, H.-H. Klauss, R. Khasanov, A. Amato, R. Klingeler, I. Hellmann, N. Leps, A. Kondrat, C. Hess, A. Köhler, G. Behr, J. Werner, and B. Büchner. *Phys. Rev. Lett.*, 101:097009, 2008.

[92] V. J. Emery and S. A. Kivelson. *Nature*, 374:434, 1995.

[93] Y. Mizuguchi, F. Tomioka, S. Tsuda, T. Yamaguchi, and Y. Takano. *Physica C: Superconductivity*, 469:1027, 2009.

[94] H. Okada, H. Takahashi, Y. Mizuguchi, Y. Takano, and H. Takahashi. *J. Phys. Soc. Japan*, 78:083709, 2009.

[95] J. E. Oldfield, W. H. Allaway, H. A. Laitinen, H. W. Lakin, and O. H. Muth. *Geochemistry and the Environment.* National Academy of Sciences, 1974.

[96] Y. Kawashima, K. Ichimura, J. Ishioka, T. Kurosawa, M. Oda, K. Yamaya, and S. Tanda. *Physica B: Condens. Matter*, 407:1796, 2012.

[97] C. P. Hunt, B. M. Moskowitz, and S. K. Bannerjee. *Handbook of Physical Constants.* American Geophysical Union, Washington DC, 1995.

[98] M. Konczykowski, L. I. Burlachkov, Y. Yeshurun, and F. Holtzberg. *Phys. Rev. B*, 43:13707, 1991.

[99] T. Shibauchi, K. Hashimoto, R. Okazaki, and Y. Matsuda. *Physica C: Superconductivity*, 469:590, 2009.

[100] P. Zajdel, P.-Y. Hsieh, E. E. Rodriguez, N. P. Butch, J. D. Magill, J. Paglione, P. Zavalij, M. R. Suchomel, and M. A. Green. *J. Am. Chem. Soc.*, 132:13000, 2010.

[101] X. Wang, S. R. Ghorbani, G. Peleckis, and S. Dou. *Adv. Mater.*, 21:236, 2009.

[102] A. Pal, A. Vajpayee, H. Kishan, and V. P. S. Awana, 2010.

[103] S. Margadonna, Y. Takabayashi, M. T. McDonald, K. Kasperkiewicz, Y. Mizuguchi, Y. Takano, A. N. Fitch, E. Suard, and K. Prassides. *Chem. Commun.*, page 5607, 2008.

[104] J. K. Dong, T. Y. Guan, S. Y. Zhou, X. Qiu, L. Ding, C. Zhang, U. Patel, Z. L. Xiao, and S. Y. Li. *Phys. Rev. B*, 80:024518, 2009.

[105] J. E. Sonier, J. H. Brewer, R. F. Kiefl, G. D. Morris, R. I. Miller, D. A. Bonn, J. Chakhalian, R. H. Heffner, W. N. Hardy, and R. Liang. *Phys. Rev. Lett.*, 83:4156, 1999.

[106] H. Braun. *Phys. Lett. A*, 75:386, 1980.

[107] C. U. Segre and H. F. Braun. *Phys. Lett. A*, 85:372, 1981.

[108] H.F. Braun, C.U. Segre, F. Acker, M. Rosenberg, S. Dey, and P. Deppe. *J. Magn. Magn. Mater.*, 25:117, 1981.

[109] A. M. Umarji, S. K. Malik, and G. K. Shenoy. *J. Appl. Phys.*, 57:3118, 1985.

[110] C. U. Segre and H. F. Braun. *Physics of Solids Under High Pressure.* J. S. Schilling and R. N. Sheloton (North-Holland, Amsterdam), p. 381, 1981.

[111] S. Noguchi and K. Okuda. *Physica B (Amsterdam)*, 194B:1975, 1994.

[112] B. Chabot and E. Parthe. *J. Less-Common Met.*, 97:285, 1984.

[113] D. C. Johnston and H. F. Braun. *Superconductivity Ternary Compounds II.* edited by M. B. Maple and . Fischer Springer-Verlag, Berlin, 1982.

[114] T. Tamegai, T. Nakagawa, and M. Tokunaga. *Physica C (Amsterdam)*, 460: 708, 2007.

[115] Y. Xu and R.N. Shelton. *Solid State Commun.*, 68:395, 1988.

[116] P.W. and Anderson. *J. Phys. Chem. Solids*, 11:26, 1959.

[117] R. J. Noer, T. P. Chen, and E. L. Wolf. *Phys. Rev. B*, 31:647, 1985.

[118] T. Tamegai, Y. Nakajima, T. Nakagawa, G. Li, and H. Harima. *Sci. Technol. Adv. Mater.*, 9:044206, 2008.

[119] C. B. Vining, R. N. Shelton, H. F. Braun, and M. Pelizzone. *Phys. Rev. B*, 27:2800, 1983.

[120] G. R. Stewart, G. P. Meisner, and C. U. Segre. *J. Low Temp. Phys.*, 59:237, 1985.

[121] G. Mu, H. Luo, Z. Wang, L. Shan, C. Ren, and H.-H. Wen. *Phys. Rev. B*, 79: 174501, 2009.

[122] G. Mu, B. Zeng, P. Cheng, Z. Wang, L. Fang, B. Shen, L. Shan, C. Ren, and H. Wen, 2009.

[123] K. Gofryk, A. S. Sefat, E. D. Bauer, M. A. McGuire, B. C. Sales, D. Mandrus, J. D. Thompson, and F. Ronning. *New J. Phys.*, 12:023006, 2010.

[124] C. Kübert and P. J. Hirschfeld. *Solid State Commun*, 105:459, 1998.

[125] R. T. Gordon, M. D. Vannette, C. Martin, Y. Nakajima, T. Tamegai, and R. Prozorov. *Phys. Rev. B*, 78:024514, 2008.

[126] V. G. Kogan, C. Martin, and R. Prozorov. *Phys. Rev. B*, 80:014507, 2009.

[127] Y.S. Wang J. Cmaidalka Y.Y. Sun Y.Y. Xue J.K. Meen C.W. Chu R.L. Meng, B. Lorenz. *Physica C*, 382:113, 2002.

[128] S. Sanfilippo, H. Elsinger, M. Núñez Regueiro, O. Laborde, S. LeFloch, M. Affronte, G. L. Olcese, and A. Palenzona. *Phys. Rev. B*, 61:R3800, 2000.

[129] M. Imai, E. Abe, J. H. Ye, K. Nishida, T. Kimura, K. Honma, H. Abe, and H. Kitazawa. *Phys. Rev. Lett.*, 87:077003, 2001.

[130] M. Imai, K. Nishida, T. Kimura, and H. Abe. *Appl. Phys. Lett.*, 80:1019, 2002.

[131] B. Lorenz, J. Cmaidalka, R. L. Meng, and C. W. Chu. *Phys. Rev. B*, 68: 014512, 2003.

[132] A. K. Ghosh, M. Tokunaga, and T. Tamegai. *Phys. Rev. B*, 68:054507, 2003.

[133] G. Q. Huang, M. Liu, L. F. Cheng, and D. Y. Xing. *J. Phys.: Condens. Matter*, 17:7151, 2005.

[134] C. S. Lue, S. Y. Wang, and C. P. Fang. *Phys. Rev. B*, 75:235111, 2007.

[135] B. Lorenz, J. Lenzi, J. Cmaidalka, R. L. Meng, Y. Y. Sun, Y. Y. Xue, and C. W. Chu. *Physica C*, 383:191, 2002.

[136] M. Imai, K. Nishida, T. Kimura, H. Kitazawa, H. Abe, H. Kito, and K. Yoshii. *Physica C*, 382:361, 2002.

[137] I. I. Mazin and D. A. Papaconstantopoulos. *Phys. Rev. B*, 69:180512, 2004.

[138] R. Heid, K. P. Bohnen, B. Renker, P. Adelmann, T. Wolf, D. Ernst, and H Schober. *J. Low Temp. Phys.*, 147:375, 2007.

[139] H. Sagayama, Y. Wakabayashi, H. Sawa, T. Kamiyama, A. Hoshikawa, S. Harjo, K. Uozato, A. K. Ghosh, M. Tokunaga, and T. Tamegai. *J. Phys. Soc. Japan*, 75:043713, 2006.

[140] S. Kuroiwa, H. Sagayama, T. Kakiuchi, H. Sawa, Y. Noda, and J. Akimitsu. *Phys. Rev. B*, 74:014517, 2006.

[141] S. Kuroiwa, K.H. Satoh, A. Koda, R. Kadono, K. Ohishi, W. Higemoto, and J. Akimitsu. *J. Phys. Chem. Solids*, 68:2124, 2007.

[142] M. Tinkham. *Phys. Rev.*, 129:2413, 1963.

[143] L. Boeri, J. S. Kim, M. Giantomassi, F. S. Razavi, S. Kuroiwa, J. Akimitsu, and R. K. Kremer. *Phys. Rev. B*, 77:144502, 2008.

[144] I.R. Shein, N.I. Medvedeva, and A.L. Ivanovskii. *J. Phys.: Condens. Matter*, 15:L541, 2003.

[145] G. Q. Huang, L. F. Chen, M. Liu, and D. Y. Xing. *Phys. Rev. B*, 69:064509, 2004.

[146] S. Kuroiwa, A. Nakashima, S. Miyahara, N. Furukawa, and J. Akimitsu. *J. Phys. Soc. Jpn.*, 76:113705, 2007.

[147] S. Tsuda, T. Yokoya, S. Shin, M. Imai, and I. Hase. *Phys. Rev. B*, 69:100506, 2004.

[148] S. Lupi, *et al. Phys. Rev. B*, 77:054510, 2008.

[149] R. Prozorov, T. A. Olheiser, R. W. Giannetta, K. Uozato, and T. Tamegai. *Phys. Rev. B*, 73:184523, 2006.

[150] S. Kuroiwa, *et al. Phys. Rev. B*, 76:104508, 2007.

[151] R. Cubitt, E. M. Forgan, G. Yang, S. L. Lee, D. McK. Paul, H. A. Mook, M. Yethiraj, P. H. Kes, T. W. Li, A. A. Menovsky, Z. Tarnawski, and K. Mortensen. *Nature (London)*, 365:407, 1993.

[152] Y. De Wilde, M. Iavarone, U. Welp, V. Metlushko, A. E. Koshelev, I. Aranson, G. W. Crabtree, and P. C. Canfield. *Phys. Rev. Lett.*, 78:4273, 1997.

[153] D. McK. Paul, C. V. Tomy, C. M. Aegerter, R. Cubitt, S. H. Lloyd, E. M. Forgan, S. L. Lee, and M. Yethiraj. *Phys. Rev. Lett.*, 80:1517, 1998.

[154] V. G. Kogan, P. Miranović, Lj. Dobrosavljević-Grujić, W. E. Pickett, and D. K. Christen. *Phys. Rev. Lett.*, 79:741, 1997.

[155] A. Gurevich and V. G. Kogan. *Phys. Rev. Lett.*, 87:177009, 2001.

[156] N. Nakai, P. Miranović, M. Ichioka, and K. Machida. *Phys. Rev. Lett.*, 89: 237004, 2002.

[157] S. J. Levett, C. D. Dewhurst, and D. McK. Paul. *Phys. Rev. B*, 66:014515, 2002.

[158] V. G. Kogan, M. Bullock, B. Harmon, P. Miranovic-acute, Lj. Dobrosavljevic-acute Grujic-acute, P. L. Gammel, and D. J. Bishop. *Phys. Rev. B*, 55:R8693, 1997.

[159] K. Park and D. A. Huse. *Phys. Rev. B*, 58:9427, 1998.

[160] M. Imai, E.-H. S. Sadki, H. Abe, K. Nishida, T. Kimura, T. Sato, K. Hirata, and H. Kitazawa. *Phys. Rev. B*, 68:064512, 2003.

[161] R. Cubitt, M. R. Eskildsen, C. D. Dewhurst, J. Jun, S. M. Kazakov, and J. Karpinski. *Phys. Rev. Lett.*, 91:047002, 2003.

[162] S. Kuroiwa, H. Sagayama, T. Muranaka, H. Kawano-Furukawa, and J. Akimitsu. *J. Phys. Chem. Solids*, 68:2129, 2007.

[163] M. Yethiraj, D. McK. Paul, C. V. Tomy, and J. R. Thompson. *Phys. Rev. B*, 58:R14767, 1998.

[164] C. D. Dewhurst, S. J. Levett, and D. McK. Paul. *Phys. Rev. B*, 72:014542, 2005.

[165] V. G. Kogan, P. Miranovic, and D. McK. Paul. *Vortex Lattice Transitions.* ed. C. A. R. Sa de Melo, pp 127 - 149, World Scientific, Singapore, 1998.

[166] L. Ya. Vinnikov, T. L. Barkov, P. C. Canfield, S. L. Bud'ko, J. E. Ostenson, F. D. Laabs, and V. G. Kogan. *Phys. Rev. B*, 64:220508, 2001.

[167] A. Yaouanc, P. Dalmas de Réotier, and E. H. Brandt. *Phys. Rev. B*, 55:11107, 1997.

[168] Z. Hao, J. R. Clem, M. W. McElfresh, L. Civale, A. P. Malozemoff, and F. Holtzberg. *Phys. Rev. B*, 43:2844, 1991.

[169] L. J. Campbell, M. M. Doria, and V. G. Kogan. *Phys. Rev. B*, 38:2439, 1988.

[170] V. G. Kogan. *Phys. Rev. B*, 66:020509, 2002.

[171] P. Miranović, K. Machida, and V. G. Kogan. *J. Phys. Soc. Jpn.*, 72:221, 2003.

[172] B. T. Matthias, T. H. Geballe, K. Andres, E. Corenzwit, G. W. Hull, and J. P. Maita. *Science*, 159:530, 1968.

[173] C. W. Chu and H. H. Hill. *Science*, 159:1227, 1968.

[174] V. A. Gasparov, N. S. Sidorov, and I. I. Zver'kova. *Phys. Rev. B*, 73:094510, 2006.

[175] D. Daghero, R. S. Gonnelli, G. A. Ummarino, A. Calzolari, V. Dellarocca, V. A. Stepanov, V. B. Filippov, and Y. B. Paderno. Andreev-reflection spectroscopy in zrb 12 single crystals. *Supercond. Sci. Technol.*, 17:S250, 2004.

[176] M. I. Tsindlekht, G. I. Leviev, I. Asulin, A. Sharoni, O. Millo, I. Felner, Yu. B. Paderno, V. B. Filippov, and M. A. Belogolovskii. *Phys. Rev. B*, 69:212508, 2004.

[177] I. Shein and A. Ivanovskii. *Phys. Solid State*, 45:1429–1434, 2003.

[178] J. Teyssier, A. B. Kuzmenko, D. van der Marel, F. Marsiglio, A. B. Liashchenko, N. Shitsevalova, and V. Filippov. *Phys. Rev. B*, 75:134503, 2007.

[179] Y. Wang, R. Lortz, Y. Paderno, V. Filippov, S. Abe, U. Tutsch, and A. Junod. *Phys. Rev. B*, 72:024548, 2005.

[180] R. P. Huebener. *Magnetic Flux Structures in Superconductors.* Springer-Verlag, New York, 1979.

[181] B. D. Rainford and G. J. Daniel. *Hyperfine Interact.*, 87:1129, 1994.

[182] T. Kubo, R. & Toyabe. *Magnetic Resonance and Relaxation.* R. Blinc, North-Holland, Amsterdam, 1966.

[183] D. M. Granty and R. K. Harris. *Encyclopedia of Nuclear Magnetic Resonance.* vol. 5, John Wiley & Sons, Chichester, UK, 1996.

[184] H. Essman, V. & Träuble. *Phys. Lett. A*, 24:526, 1967.

[185] E. Bauer, G. Hilscher, H. Michor, Ch. Paul, E. W. Scheidt, A. Gribanov, Yu. Seropegin, H. Noël, M. Sigrist, and P. Rogl. *Phys. Rev. Lett.*, 92:027003, 2004.

[186] L. P. Gor'kov and E. I. Rashba. *Phys. Rev. Lett.*, 87:037004, 2001.

[187] S. Fujimoto. *J. Phys. Soc. Japan*, 76:051008, 2007.

[188] P. A. Frigeri, D. F. Agterberg, A. Koga, and M. Sigrist. *Phys. Rev. Lett.*, 92: 097001, 2004.

[189] K. V. Samokhin, E. S. Zijlstra, and S. K. Bose. *Phys. Rev. B*, 69:094514, 2004.

[190] V. P. Mineev. *Phys. Rev. B*, 71:012509, 2005.

[191] N. Kimura, K. Ito, K. Saitoh, Y. Umeda, H. Aoki, and T. Terashima. *Phys. Rev. Lett.*, 95:247004, 2005.

[192] I. Sugitani, Y. Okuda, H. Shishido, T. Yamada, A. Thamizhavel, E. Yamamoto, T. D. Matsuda, Y. Haga, T. Takeuchi, R. Settai, and Y. Ōnuki. *J. Phys. Soc. Japan*, 75:043703, 2006.

[193] N. Metoki, K. Kaneko, T. D. Matsuda, A. Galatanu, T. Takeuchi, S. Hashimoto, T. Ueda, R. Settai, Y. O-nuki, and N. Bernhoeft. *J. Phys.: Condens. Matter*, 16:L207, 2004.

[194] T. Akazawa, H. Hidaka, H. Kotegawa, T. C. Kobayashi, T. Fujiwara, E. Yamamoto, Y. Haga, R. Settai, and Y. Ōnuki. *J. Phys. Soc. Japan*, 73:3129, 2004.

[195] T. Nakane, T. Mochiku, H. Kito, J. Itoh, M. Nagao, H. Kumakura, and Y. Takanol. *Appl. Phys. Lett.*, 84:2859, 2004.

[196] R. Settai, I. Sugitani, Y. Okuda, A. Thamizhavel, M. Nakashima, Y. Onuki, and H. Harima. *J. Magn. Magn. Mater.*, 310:844, 2007.

[197] A. D. Hillier, J. Quintanilla, and R. Cywinski. *Phys. Rev. Lett.*, 102:117007, 2009.

[198] R. D. Blaugher and J. K. Hulm. *J. Phys. Chem. Solids*, 19:134, 1961.

[199] R. D. Blaugher, A Taylor, and J. K. Hulm. *IBM J. Res. Dev.*, 6:116, 1962.

[200] Y. L. Zuev, V. A. Kuznetsova, R. Prozorov, M. D. Vannette, M. V. Lobanov, D. K. Christen, and J. R. Thompson. *Phys. Rev. B*, 76:132508, 2007.

[201] V. A. Kuznetsova, 2007. Ph.D. thesis, University of Tennessee.

[202] Y. Huang, J. Yan, Y. Wang, L. Shan, Q. Luo, W Wang, and H.-H. Wen. *Supercond. Sci. Technol.*, 21:075011, 2008.

[203] Y. Aoki, A. Tsuchiya, T. Kanayama, S. R. Saha, H. Sugawara, H. Sato, W. Higemoto, A. Koda, K. Ohishi, K. Nishiyama, and R. Kadono. *Phys. Rev. Lett.*, 91:067003, 2003.

[204] G. M. Luke, Y. Fudamoto, K. M. Kojima, M. I. Larkin, J. Merrin, B. Nachumi, Y. J. Uemura, Y. Maeno, Z. Q. Mao, Y. Mori, H. Nakamura, and M. Sigrist. *Nature (London)*, 394:558, 1998.

[205] E. H. Brandt. *Phys. Rev. B*, 68:054506, 2003.

[206] A. C. Larson and R. B. V. Dreele. *Los Alamos National Laboratory Report LAUR*, page 86, 1994.

[207] B. H. Toby. *J. Appl. Cryst.*, 34:210, 2001.

[208] R. G. Mints and A. L. Rakhmanov. *Rev. Mod. Phys.*, 53:551, 1981.

[209] T. P. Orlando, E. J. McNiff, S. Foner, and M. R. Beasley. *Phys. Rev. B*, 19: 4545, 1979.

[210] S. V. Shulga, S.-L. Drechsler, G. Fuchs, K.-H. Müller, K. Winzer, M. Heinecke, and K. Krug. *Phys. Rev. Lett.*, 80:1730, 1998.

[211] I. Shigeta, T. Abiru, K. Abe, A. Nishida, and Y. Matsumoto. *Physica C*, 392: 359, 2003.

[212] Y. Takano, H Takeya, H. Fujii, H. Kumakura, T. Hatano, K. Togano, H. Kito, and H. Ihara. *Appl. Phys. Lett.*, 78:2914, 2001.

[213] A. B. Karki, Y. M. Xiong, N. Haldolaarachchige, S. Stadler, I. Vekhter, P. W. Adams, D. P. Young, W. A. Phelan, and Julia Y. Chan. *Phys. Rev. B*, 83: 144525, 2011.

[214] R. Micnas, J. Ranninger, and S. Robaszkiewicz. *Rev. Mod. Phys.*, 62:113, 1990.

[215] R. S. Hayano, Y. J. Uemura, J. Imazato, N. Nishida, T. Yamazaki, and R. Kubo. *Phys. Rev. B*, 20:850, 1979.

[216] P. K. Biswas, M. R. Lees, A. D. Hillier, R. I. Smith, W. G. Marshall, and D. M. Paul. *Phys. Rev. B*, 84:184529, 2011.